

Aerosol in the Gate Area and its Radiative Properties

By

K.Ya. Kondratyev, O.D. Barteneva, L.I. Chapursky, A.P. Chernenko, V.S. Grishechkin, L.S. Ivlev, V.A. Ivanov, V.I. Korzov, V.B. Lipatov, M.A. Prokofyev, V.K. Tolkatchev, O.B. Vasiliev and V.F. Zhvaley

Department of Atmospheric Science
Colorado State University
Fort Collins, Colorado

Department of Atmospheric Physics
Leningrad State University
and
Department of Radiation Studies
Main Geophysical Observatory
7, Karbysheva Street
194018 Leningrad, USSR

This contribution is the first of a series of reports on GATE Radiation Subprogramme results which will be published simultaneously as CSU Atmospheric Science Papers in English and in the Transactions of the Main Geophysical Observatory in Russian. Transactions of the Main Geophysical Observatory, Leningrad, Issue No. 381.

**Colorado
State
University**

**Department of
Atmospheric Science**

Paper No. 247

AEROSOL IN THE GATE AREA AND ITS
RADIATIVE PROPERTIES

This contribution is the first of a series of reports on GATE Radiation Subprogramme results which will be published simultaneously as Colorado State University Atmospheric Science Papers in English and in the Transactions of the Main Geophysical Observatory in Russian.

AEROSOL IN THE GATE AREA AND ITS RADIATIVE PROPERTIES

By

K. Ya. Kondratyev

in collaboration with:

O. D. Barteneva

L. I. Chapursky

A. P. Chernenko

V. S. Grishechkin

L. S. Ivlev

V. A. Ivanov

V. I. Korzov

V. B. Lipatov

M. A. Prokofyev

V. K. Tolkathev

O. B. Vasiliev

V. F. Zhvalev

Department of Atmospheric Physics
Leningrad State University

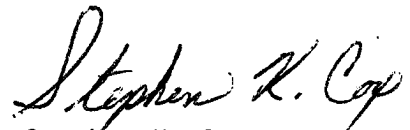
and

Department of Radiation Studies
Main Geophysical Observatory
7, Karbysheva Street
194018 Leningrad
U.S.S.R.

PREFACE

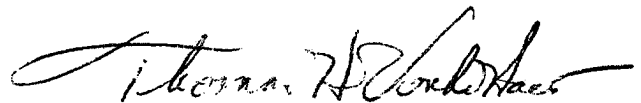
This research report authored by our Russian colleagues is being distributed jointly as a CSU Atmospheric Science Report and Leningrad State University, Department of Atmospheric Physics report in order to enhance the international distribution of the scientific information relative to GATE, collected and deduced by Professor Kondratyev and his associates at the University of Leningrad and the Main Geophysical Observatory. It is Professor Kondratyev's and our hope that this timely exchange of scientific results will facilitate research progress in atmospheric radiation studies throughout the world.

We wish to acknowledge the support of the U.S. GATE Project Office for the printing and distribution of the English version of this report.



Stephen K. Cox

Associate Professor of
Atmospheric Science.



Thomas H. Vonder Haar

Associate Professor and
Department Head.

Department of Atmospheric Science

Colorado State University

Fort Collins

Colorado

ABSTRACT

This report summarizes preliminary results of a research program conducted by Main Geophysical Observatory scientists during the GATE (GARP Atlantic Tropical Experiment). The origin and characteristic features of the dust layer are discussed. Inferences of microphysical and optical characteristics of the dust aerosol made from ship data are presented.

Chemical analyses of aerosols showed a rather high content of metals. The iron concentration nearly always exceeded 10^{-5} kg m⁻³ for aircraft aerosol observations.

Extensive data are presented giving spectral and total short-wave radiative flux divergence values for cloudfree, dust and stratoform cloud cases. These data are interpreted in the context of the meteorological conditions and the optical parameters of the aerosol or cloud layer.

TABLE OF CONTENTS

	<u>PAGE</u>
PREFACE	i
ABSTRACT	ii
LIST OF TABLES	v
LIST OF FIGURES	vi
1. INTRODUCTION	1
2. ORIGIN AND AREAL EXTENT OF THE DUST AEROSOL	3
2.1. Characteristic features of the underlying surface of the Western Sahara and its effects on the origin of the dust outbreaks.	5
2.2. Characteristic features of the dust outbreaks' images obtained from space.	10
2.3. Characteristic features of the Western Sahara dust outbreak's spatial extent over the Atlantic.	12
2.4. Meteorological conditions in the zone of the dust clouds.	18
2.4.1. Principal meteorological characteristics of the Saharan Aerosol Layer (SAL).	18
2.4.2. Synoptic situation during the powerful dust outbreak on 30 July, 1974.	21
2.4.3. Dynamics of the dust flow from Africa on 29-30 July 1974.	25
3. MICROPHYSICAL AND OPTICAL CHARACTERISTICS OF THE DUST AEROSOL AS INFERRED FROM THE SHIP DATA.	29
4. AIRCRAFT AEROSOL OBSERVATIONS.	47
5. VERTICAL PROFILES OF RADIATION FLUXES AND RADIATIVE HEAT FLUX DIVERGENCES.	55

TABLE OF CONTENTS - continued.

	<u>PAGE</u>
6. SPECTRAL DISTRIBUTION OF THE SHORTWAVE RADIATION FLUXES AND RADIATIVE HEAT FLUX DIVERGENCES.	67
6.1. Visible part of the spectrum.	67
6.1.1. Spectral fluxes and balances in a cloudless atmosphere and in the presence of a stratocumulus cloud layer.	67
6.1.2. The albedo transformation of the system "ocean surface - atmosphere".	70
6.1.3. The spectral radiative heat flux divergences in the cloudless and cloudy atmosphere.	74
6.2. The near-IR spectrum region.	79
7. ANGULAR AND SPECTRAL CHARACTERISTICS OF SHORTWAVE RADIATION REFLECTANCE.	96
7.1. Spectral albedo.	96
7.2. Reflectance functions.	98
8. CONCLUSION.	106
REFERENCES.	107

LIST OF TABLES

<u>TABLE</u>		<u>PAGE</u>
1	Optical characteristics of the atmosphere in the Kara-Kum desert in the tropical zone of the Atlantic.	37
2	Atmospheric transparency in the zone of the dust outbreak.	39
3	Values of the atmospheric optical characteristics observed under maximum turbidity.	41
4	Chemical analysis data for the aerosol particles sampled by the IL-18 aircraft in the dust cloud.	51
4a	As above for a dust-free atmosphere.	52
5	"Blue-red" ratios for albedo.	73
6	Total, molecular and aerosol relative influxes of radiative energy.	91

LIST OF FIGURES

<u>FIGURE</u>		<u>PAGE</u>
1	The scheme of the Western Sahara underlying surface in the region of dust storms development from the "World Atlas" (Moscow, GUGK, 1967).	6
2a	The photo of the dust outbreak over the Atlantic taken from SMS-1 on July 4, 1974.	8
2b	As above for July 30, 1974.	9
3a	Dynamics of the dust cloud inferred from IR SMS-1 images at 1600 GMT, on 29 July, 1974	13
3b	As above at 2100 GMT, on 29 July, 1974.	14
3c	As above at 0700 GMT, on 30 July, 1974.	15
4	Typical meteorological conditions in the dust cloud zone.	20
5	The surface synoptic map of the dust outbreak area of 30 July, 1974, 0000 GMT.	23
6	The baric topography map AT-700, 30 July, 1974, at 0000 GMT.	24
7	The surface synoptic map of the dust outbreak of 29 July, 1974, 1200 GMT.	26
8	Regions of the dust fall-out in the Atlantic from the data in Ref. 8.	30
9	Meridional profiles of aerosol characteristics from TROPEX-72 data.	32
10	Spectra of particles' size from the TROPEX-72 data.	33
11	Comparison of the air temperature meridional curves at altitudes of 27 m (1), 1000 m (2), 2000 m (3), 3000 m (4), and variation of the value of direct solar radiation attenuation due to aerosol (5).	35
12	Light-scattering indicatrices in the near-water atmospheric layer.	43
13	The scheme of the ships' location in the GATE test area.	44
14	Vertical profile of aerosol concentration of 4 July, 1974.	48
15	The Complete Radiation Experiment.	49
16	Vertical profiles of the total radiation: 1 - 4 July, 1974, 1330 GMT. 2 - 13 August, 1974, 1350, GMT. 3 - 14 August, 1974, 1420, GMT. 4 - 4 September, 1974, 1300, GMT.	58

LIST OF FIGURES - Continued

<u>FIGURE</u>		<u>PAGE</u>
17	Vertical profiles of the shortwave upwelling radiation fluxes. Notations, dates and measurement times are the same as in Fig. 16.	59
18	Vertical profiles of albedo A. Notations, dates and measurement times are the same as in Fig. 16.	61
19	Vertical profiles of the longwave downwelling, L_{\downarrow} , and upwelling, L_{\uparrow} , radiation fluxes. Notations, dates and measurement times as in Fig. 16.	62
20	Vertical profiles of radiative heat flux divergence. Notations, dates and measurement times as in Fig. 16.	64
21	Spectral downwelling, $K_{\lambda\downarrow}$, and upwelling, $K_{\lambda\uparrow}$, radiation fluxes at different atmospheric levels.	68
22	Spectral net radiation, B_{λ} , at different atmospheric levels.	71
23	Spectral albedo of the "ocean surface-atmosphere" system.	72
24	Spectral absolute, ζ_{λ} , and relative β_{λ} radiative heat flux divergence in atmospheric layers of various thicknesses.	76
25	Absolute aerosol radiative heat flux divergence (double dashing) and molecular radiative heat flux divergence (single dashing) for the whole of the sounded atmosphere.	78
26	Spectral radiative heat flux divergence in the atmosphere with a continuous Sc layer.	80
27	Spectral relative radiative heat flux divergences, β_{λ}^i , transmission coefficients, $T_{\lambda}(a)$, and albedo $A_{\lambda}(b)$ as inferred from the measurements made on 4 September, 1974, at 1200 with $h_{\odot} = 71^{\circ}$ by the SPI-74 (2-10) and K-2 (1,11) spectrometers.	84
28	Spectral relative radiative heat flux divergences, β_{λ}^i , transmission coefficients, $T_{\lambda}(a)$ and albedo $A_{\lambda}(b)$ as inferred from the measurements made on 4 September, 1974, at 1450 with $h_{\odot} = 76^{\circ}$ by the SPI-74 (2-7, 9-12) and K-2 (1, 8) spectrometers.	85
29	Spectral transmission coefficients, T_{λ} , and relative radiative heat flux divergences, β_{λ}^i , as inferred from the measurements made on 31 August, 1974, at 1251 with $h_{\odot} = 79^{\circ}$ (a) and at 1500 with $h_{\odot} = 63^{\circ}$ (b) by the SPI-74 spectrometer.	88

LIST OF FIGURES - Continued

<u>FIGURE</u>		<u>PAGE</u>
30	Vertical profiles of the spectral albedo as inferred from measurements made on 31 August, 1974 (a) and 22 September, 1974 (b).	89
31	Spectral relative radiative heat flux divergences β'_{λ} transmission coefficients, $T_{\lambda}(a)$ and albedo $A_{\lambda}(b)$ as inferred from the measurements made on 12 July, 1974 at 1330 with $h_{\odot} = 81^{\circ}$ by the SPI-74 and K-2 spectrometers.	93
32	The spectral albedo vertical profiles measured by the albedometer.	97
33	The angular dependence of brightness coefficient with the sun vertical for $\lambda = 0.99 \mu\text{m}$ and different flight altitudes.	100
34	Vertical profiles of the reflection asymmetry coefficient with the sun vertical for different days and wavelengths.	102
35	Vertical profiles of the reflectivity anisotropy coefficient for different days and wavelengths.	104

1. INTRODUCTION

One of the characteristic features of the tropical atmosphere's general circulation is the significant effect upon it of radiation factors [1, 41], which explains the important role of the GATE Radiation Subprogram and the need for adequate incorporation of the radiative flux divergence in solving the main problems of GATE.

The conditions of the radiation transfer in the tropical atmosphere of the equatorial Atlantic are rather specific: high temperature and high air humidity, frequent African dust-sandy outbreaks of large areal extent, specific (and drastically variable depending on latitude) conditions of cloudiness - all these cause the necessity for elaborating specific techniques for parameterizing the radiation processes and the checking of such techniques by the GATE RSP data.

The incorporation of the aerosol effects on the shortwave and long-wave radiation transfer is an important aspect of parameterization. Therefore, the present paper discusses mainly this aspect. The ship and aircraft observations carried out within the framework of the GATE RSP [30] have made it possible to obtain the extensive material allowing the complete analysis of both the characteristic features of the time-spatial variation of the aerosol concentration field and its properties (size distribution, chemical composition, optical parameters), and the effect of aerosol on atmospheric transparency and radiation transfer.

In connection with this, special attention is paid to the problem of the Saharan Aerosol Layer (SAL) effect on radiation transfer and meteorological regime, when gigantic dust clouds flow from the Sahara, (which sometimes cross the Atlantic Ocean and reach the American coast). It is beyond doubt that the study of the SAL and other analogous aerosol formations is of great interest from the point of view of the 'climate and aerosol' problem.

It would be quite natural to begin with a discussion of the GATE RSP data already processed: i.e. characteristics of the meteorological conditions, analysis of the origin and areal extent of the Saharan dust-sandy flows from the geostationary satellite photographs (Section 2). Then the data on size distribution and chemical composition of the dust aerosol are considered (Section 3). The characteristic features of the radiative climatology in the GATE area are described in Section 4, and the data on the atmospheric transparency are given. The characteristic features of the vertical profiles of radiation fluxes and radiative heat flux divergences vs. the vertical structure of the aerosol concentration field, as inferred from the aircraft data, are given in Section 5. Section 6 deals with the spectral measurements of the shortwave radiation fluxes. The paper ends with Section 7 dedicated to studies of angular and spectral characteristics of shortwave radiation reflectance.

2. ORIGIN AND AREAL EXTENT OF THE DUST AEROSOL

The powerful dust outbreaks from the Sahara over the Atlantic ocean are rather frequent. The zone of the main dust fall-out (the so-called "Sea of Darkness") was determined from the data of numerous ship observations.

Aside from this zone of reddish-brown dust fall-out brought by the north-east trade winds, the area of the dust fall-out was found in the zone affected by the "harmatan" effect (the east wind developed in the southern Sahara). The satellites contributed much to the detailed study of these phenomena: the dust clouds were studied from space photographs [2, 3, 29, 40]. With the help of the images obtained from the ATS-1 geostationary satellite one could observe the development of an enormous dust cloud [28]; and the Saharan dust was sampled near the Barbados Island [39].

From the satellite and ground-truth data, the variation of dust composition was studied versus geographical location of the dust outbreak [37].

In April, 1972, on board the ship "Akademik Shirshov", the aerosol measurements in the region of a large dust cloud registered from the meteorological satellite TV images, were carried out. They made it possible to assess the dust mass in the cloud to be about 5 million tons [5].

During the Soviet expedition TROPEX-72, interesting results were obtained which indicated that the drastic deterioration of transparency, and the highest aerosol concentrations coincided with the powerful dust flows from Africa [4].

However, all the above-mentioned data are rather scarce and fragmentary. These data were analyzed without regard for conditions of the dust

flow's origin and development over land, which are connected with meteorological conditions and characteristic features of the underlying surface; also the dust flow dynamics were not considered, and the chemical composition of the dust was studied insufficiently.

The GATE made it possible to carry out the complete complex investigations of the powerful dust pollution of the atmosphere. Apart from the ship measurements, aircraft soundings were performed, during which the aerosol was sampled, and spectral measurements of radiation fluxes were made.

At the same time, a large sea area was investigated, which made it possible to obtain the data on aerosol spatial variations. The GATE area images obtained from the Soviet meteorological satellites "Meteor-16, 17, 18", the American geostationary satellites ATS-6, SMS-1, and quasipolar satellites NOAA-2, NOAA-3 are an important source of information.

The most powerful dust pollution of the atmosphere detected from the TV and IR images during GATE was observed on the 4th and 30th of July. In both cases during the dust cloud passage, complex measurements were carried out by the ship scientists, including actinometric, spectral and aerosol observations. The MGO flying laboratory (IL-18M) sounded the atmosphere to measure meteorological, aerosol and radiation parameters. Since the most intensive dust pollution of the atmosphere was observed on 29-30 July (all the ships, including "Passat", being located near the equator, registered the sharp deterioration of atmospheric transparency and the increase of aerosol concentration), it was decided to concentrate on the analysis of this case.

2.1 Characteristic Features of the Underlying Surface of the Western Sahara and its Effect on the Origin of the Dust Outbreaks

As the analysis of the space TV and IR images shows, the dust flows over the Atlantic originate from the desert zone of the Western Sahara, the dry savannas and partly the savannas within the gigantic "amphitheatre" surrounded on the north, east and south by mountains (Atlas Mountains, Ahhagar Mountains, Mountains of the Guinea Coast) and their foothills (Fig. 1). The altitudes in this region are 200-500 m above sea level. The maximum heights of the surrounding hills are 1000 m in the south, 2000 m in the east, and 3500 m in the north. Even though the "wall" of these hills is broken, its elevation shows variations, and, in the south it recedes beyond the Sahara, nevertheless the infrastructure of the relief affects, to a certain extent, the atmospheric circulation in the lower troposphere over this part of the continent, and provides for northeast to southwest and east to west air fluxes out of this natural amphitheatre and into the Atlantic.

The dust fluxes are formed within a triangle defined by the coordinates 16°W , 5°E and 28°N , 16°N . The southern boundary of this triangle is located far from the south "wall" of the hills and follows closely the border of the desert and the dry savannas. The relief of the amphitheatre's floor is formed by two main types of the underlying surfaces, namely stony plains and sandy massives.

It is interesting to note that some of these large sandy massives, Erg-Shelly (1000 km long and 200 km wide), and Erg-Igudy (700 km long and 70 km wide) are oriented from northeast to southwest, with a corresponding bend in the direction of the dominating winds.

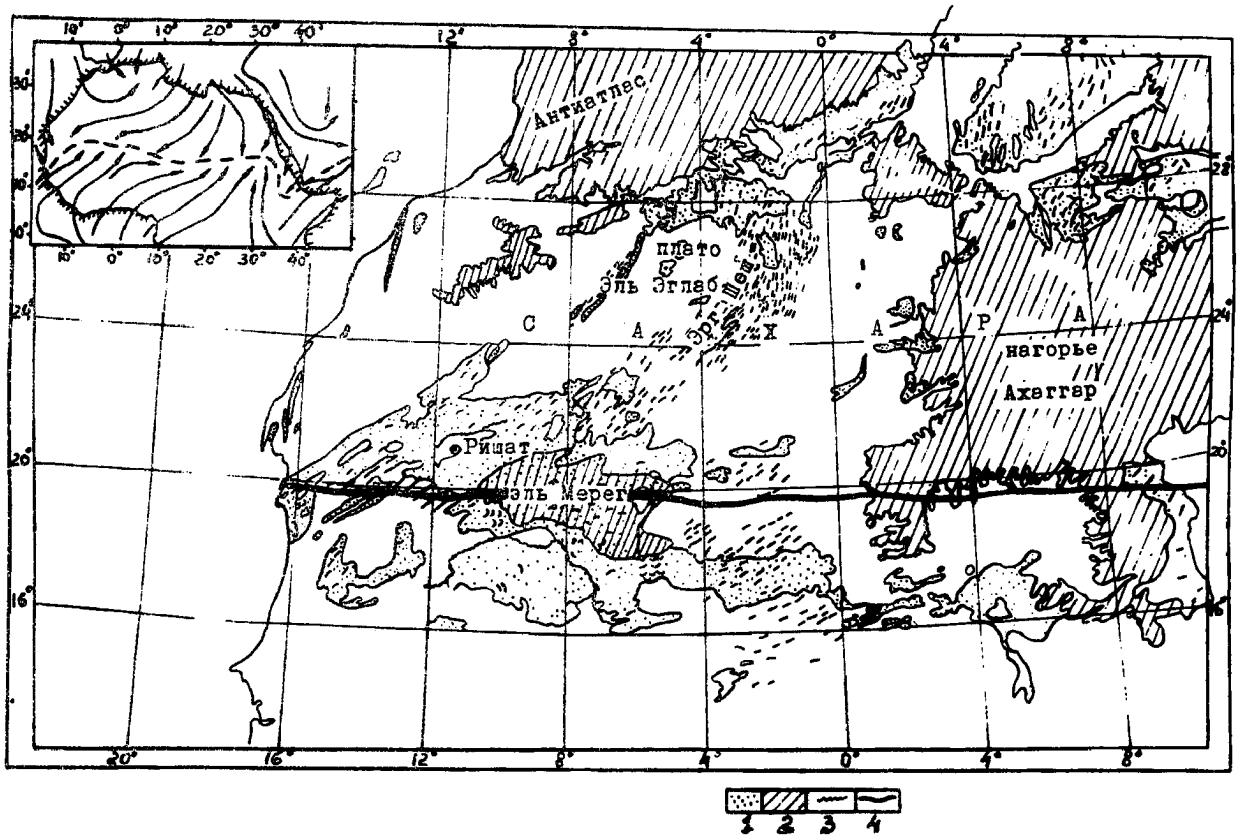


Fig. 1 The scheme of the Western Sahara underlying surface in the region of dust storms development from the "World Atlas" (Moscow, GUGK, 1967).

Notations:

- 1) Sands with dunes and barchanes.
- 2) Relief with altitudes from 500 m and higher.
- 3) Ledges.
- 4) Boundary separating the tropical belt from the sub-equatorial one (the desert and semi-desert zone from that of savannah and thin forests). - Inserted: the scheme of the direction of the dominant air flow in the surface atmospheric layer over the Northern Africa from "Climates of Africa" (Gidrometeoizdat, Leningrad, 1967).

The dominating eolian relief forms occurring in the zone of the sandy massives are longitudinal (relative to the wind direction) with sandy ridges up to several kilometers long stretching from north-northeast to south-southwest, and from northeast to southwest. The fields of these dunes stand out clearly in the photos from the manned aircraft. In the images from ERTS-1, they are observed, in some cases, not only within the sandy massives - ergs, but also on the surface of the stony plains.

The specific relief features of the stony plains, plateaux and separate hills in this particular region appear as a vast development of deflated furrows and hollows (associated with the extracting effect of the dust-sandy fluxes). The deflated forms of the relief in this region have been known before [7]. However, only with the help of the space survey did it become possible to establish the vast areal extent of such formations: they are observed even in small-scale TV images, especially in the region of Adrar plateau and in the regions located south of the residual hills (Fig. 2a). The deflated furrows cause the striped patterns of the image (associated with alternation of ridges formed of the dark-colored rocks, and depressions between them). The deflated furrows of the relief in this region are oriented from northeast to southwest. The surface deposits here vary greatly: one can observe gravel, usually rather poor deposits seated upon the native bedrock of different composition, on the stony plains, plateaux and residual hills. In some places, pebble deposits are found; but the eol sands, which are devoid of vegetation are a practically inexhaustible source of dust fluxes and are the most wide-spread particles among the loose deposits.

The sands of the Saharan ergs are mainly fine-grained quartz particles whose size is mainly 0.25-1.1 μm . They are a reddish color caused by the

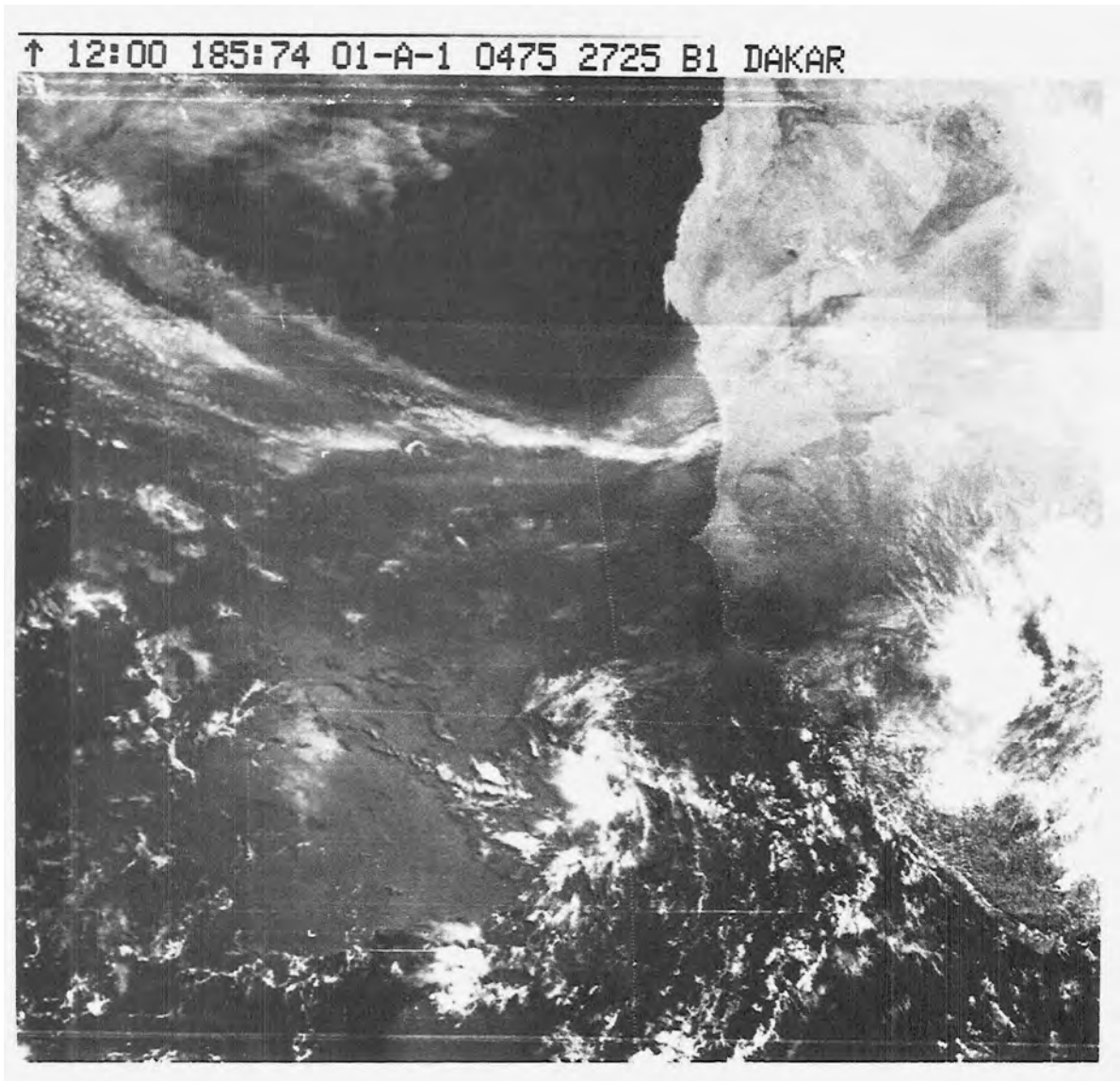


Fig. 2a Photo of the dust outbreak over the Atlantic taken from SMS-1 on 4 July, 1974.

↑ 13:00 211:74 01-A-2 0325 2500 C1 DAKAR

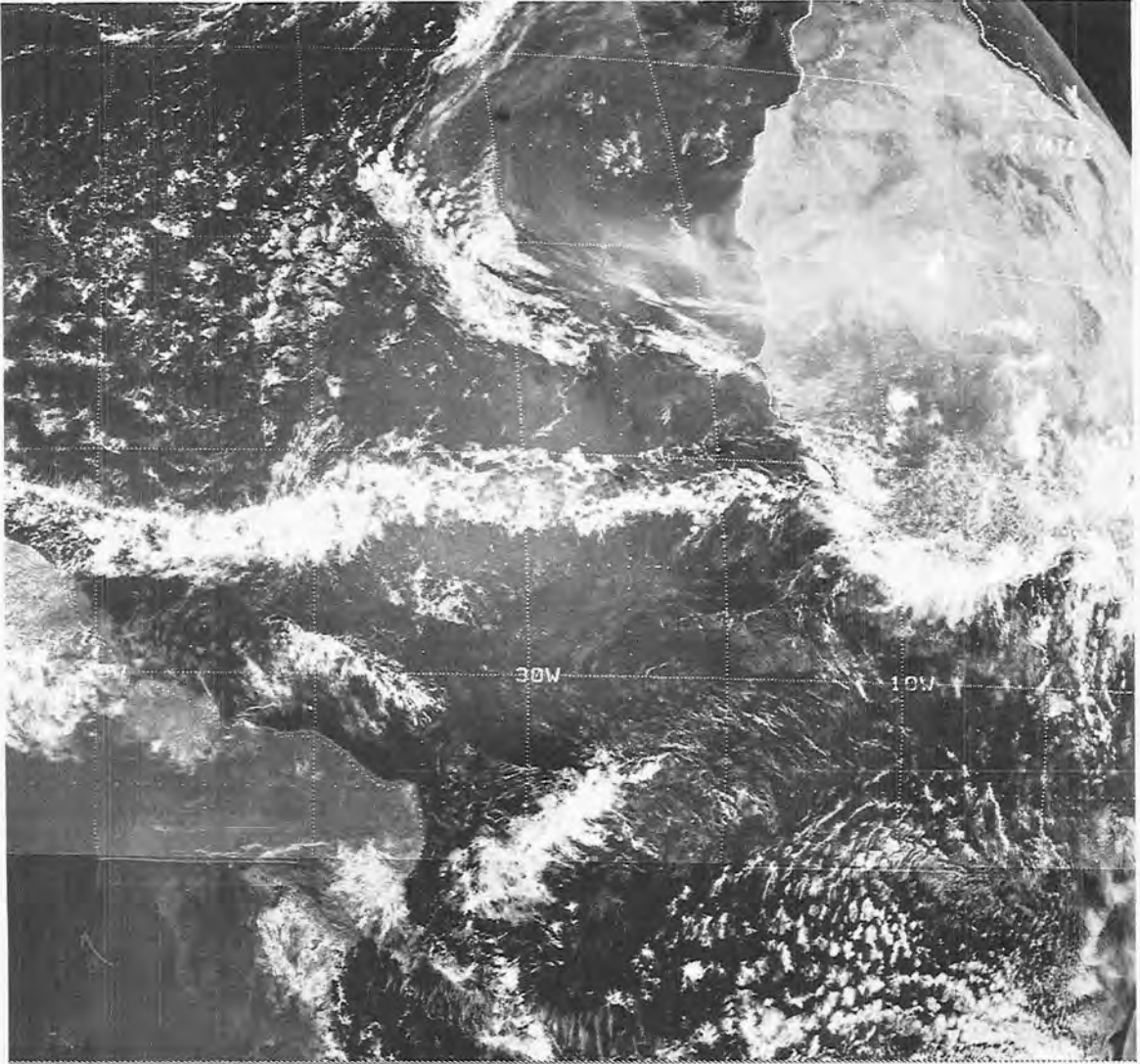


Fig. 2b Photo of the dust outbreak over the Atlantic taken from SMS-1 on 30 July, 1974.

grains' ferruginous coating - the desert crust consists of Fe_2O_3 [6, 31]. The large areal extent of such deposits observed also on the stony plains caused the reddish-pinkish tint in the color images of the region taken from aboard the manned spacecraft. This fact also causes the reddish coloration of the atmospheric dust formations flowing out from this region, which was often recorded by ships and aircraft.

Some light-colored (white, yellowish) sands are locally observed in the considered region, these being younger than the reddish sands. Finally, the alluvial sandy deposits and those containing silt are observed in the southern part of the region investigated, within the alluvial lowland of the Niger River; they are light-colored and silicon enriched due to a high content of fresh-water diatoms. Such light orange deposits are the feeding source for the dust flows to the Atlantic associated with the development of harmatan.

2.2 Characteristic Features of the Dust Outbreaks' Images Obtained From Space

The photographs from the SMS-1 geostationary satellite were used for analysis. Images of different spacial resolution and survey obtained in the visible and IR were considered, namely, the global IR images (the portion of the hemisphere seen from the satellite) with a 4 km resolution in the center, and the TV images covering the area of 6000 x 6000 km and having the resolution of 1.5 km.

The authors analyzed the images obtained during the experiment, and also used the images of the dust-flows obtained at a different time before the experiment.

In the visible, the dust flows are more distinctly seen over the aquatic area (Figs. 2a, 2b). This is caused by the larger brightness

contrast of the dust clouds over water as compared to that of the dust clouds over land. The identification of dust-flows over land in the visible is particularly complicated for this region, due to the large areal extent of the light-colored sandy deposits, which form the background surface. Besides, when passing over land, the dust flows mask the residual hills, ridges and plateaux of dark-colored rocks, which are easily singled out in the images taken in the absence of the dust-flows.

The comparison of the images of the same region taken at different times, together with characteristic features of such hills serving as marking points, makes it possible to evaluate the development of the dust-flow. This is, in particular, clearly seen in the image obtained on 30 July (Fig. 2b). The powerful dust cloud masks the details of the relief to the north and south of the Adrar plateau, that are distinctly seen in the images taken in the absence of the dust over the same region (Fig. 2a). In the images, the dust-flows often, though not always, stand out as a pronounced striped formation caused by the inhomogeneity of the dust turbidity spatial development and by the streamed structure of the dust cloud.

The presence of dust-flows is accentuated by the cloud orientation, especially in the cases when both dust-flows and clouds are drawn into the same system of the atmospheric circulation. Most often such phenomena are observed in the images over the Atlantic far from the center of the dust-flow generation (Figs. 2a, 2b). The dust-flows over the aquatic area are recognized in the TV images by the decreasing brightness of the cloud masses located below the dust cloud, i.e. the dust albedo is lower than cloud albedo. The cloud masses below the dust cloud "grow grey", and their boundaries become dim. In the IR images, the dust turbidity of the atmosphere is depicted by the light

grey tint, i.e. they are cold formations when compared to the land surface, but darker (warm) when compared to the cloud upper boundary (Figs. 3a, 3b, and 3c). In the IR day-time images, the dust formations are more distinctly seen over land, which is explained by the higher temperature contrasts of the "land-dust" system. The IR images allow one to trace the development of dust clouds not only in the day-time (as in the TV images), but also at night. By night, when the land surface is strongly cooled, the temperature contrast of the "land-dust cloud" system decreases.

The joint usage of the IR and TV images is most informative for the analysis of the dust outbreak.

2.3 Characteristic Features of the Western Sahara Dust Outbreak's Spatial Extent Over the Atlantic

Photographing from satellites has made it possible to obtain unique information about the size, configuration and areal extent of the dust outbreaks. The size of dust clouds varied during GATE within wide limits which is quite natural, and is determined by the duration of the dust outflow from the feeding center, as well as by peculiarities of the synoptic situation and atmospheric circulation.

In the images, dust clouds of quite different configuration were traced, e.g. comparatively small, almost linear, or slightly curved, like the clouds seen in the IR image obtained on 29 July (Fig. 3a). This dust cloud was 1300 km long and 200-500 km wide.

Sometimes the dust flowing from the continent to the Atlantic formed a large cloud, corresponding to the zone of "Sea of Darkness", like the situation registered at 1500 Z, 9 July. In other cases, the dust flowing to the Atlantic was drawn into the gigantic circulation of the Azores anticyclone, and as a result, the dust cloud drifted along an

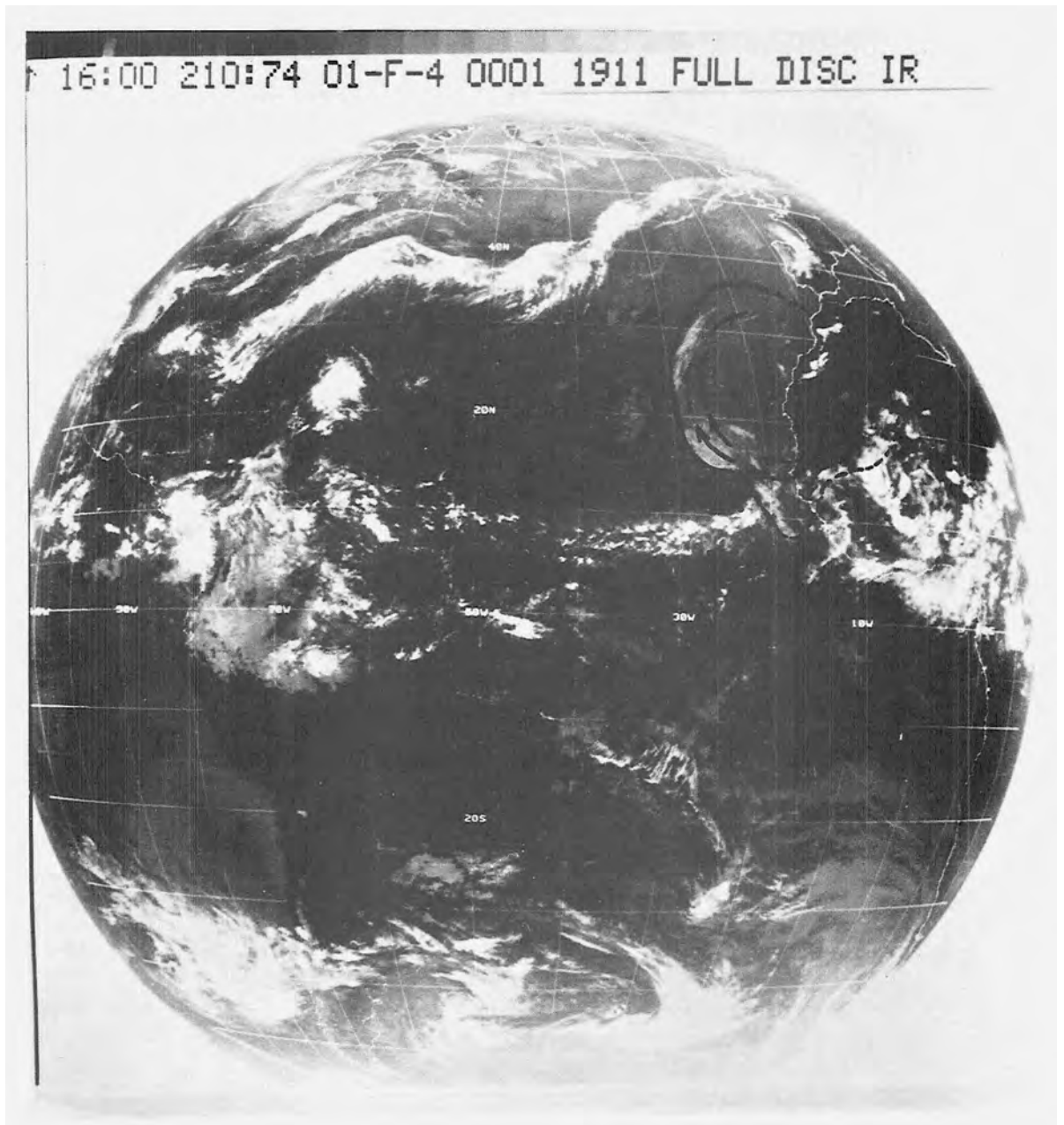


Fig. 3a Dynamics of the dust cloud of 29 July, 1974, at 1600 GMT, as inferred from the IR SMS-1 images.

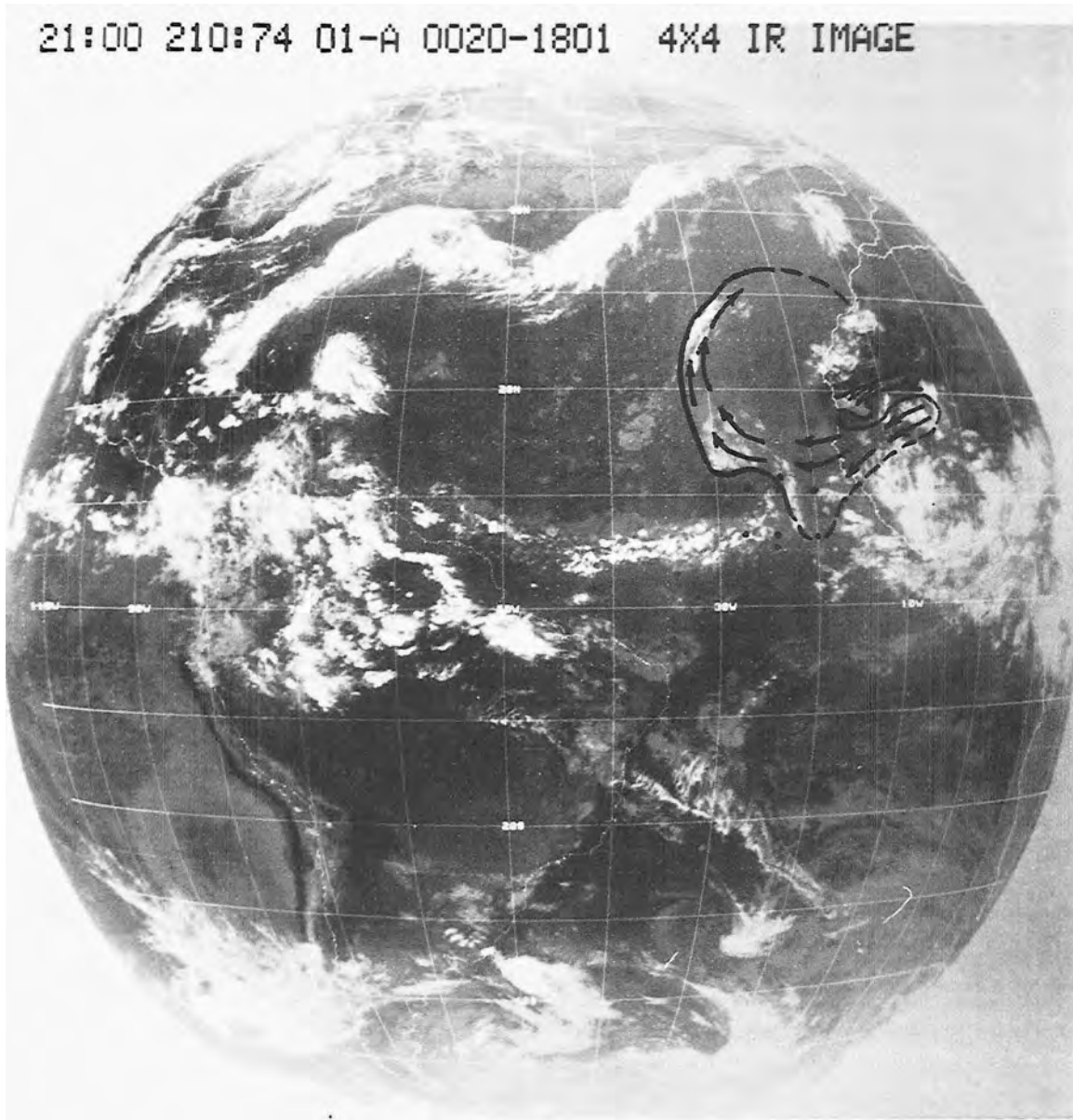


Fig. 3b Dynamics of the dust cloud of 29 July, 1974, at 2100 GMT, as inferred from the IR SMS-1 images.

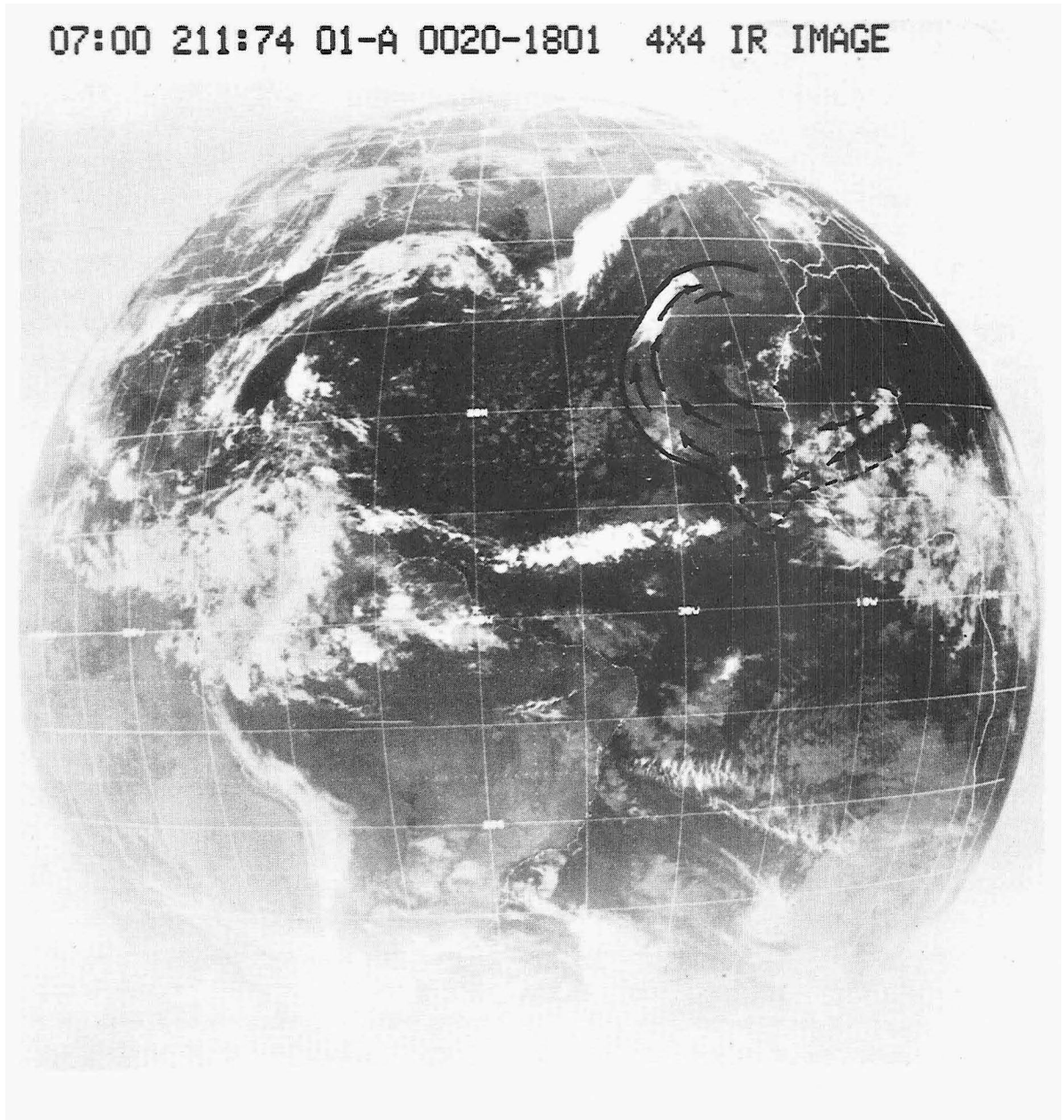


Fig. 3c Dynamics of the dust cloud of 30 July, 1974, at 0700 GMT, as inferred from the IR SMS-1 images.

enormous arc reaching the Northwestern African coast and southern Europe. This case was traced, in particular, in the IR image obtained on 30 July (Fig. 3c). The cloud was 4500 km long and 500-700 km wide. In some cases, during the western drift, the dust cloud moved to the American coast.

Such an outbreak was registered, for example, on 8 July 1974, in the image obtained from SMS-1 [32]. On 5 August, the dust cloud was detected (also from the SMS-1 images) near the eastern coast of Florida [33]. The area of the dust clouds varies depending on the power of the dust source, and the character of the atmospheric circulation; and averages several thousand square kilometers. Sometimes, dust zones of great length are observed. For example, the dust turbidity of the atmosphere over Western Africa and the Atlantic registered at 0700 Z, 30 July, covered about 6800,000 km². The area of the dust cloud was 1,500,000 km² over land and approximately 5,300,000 km² over the sea. Of even greater size was a gigantic dust cloud registered in the image on 3 July 1969, which moved toward the South American coast over the Atlantic. Its area was about 6,000,000 km², i.e. this cloud covered about 0.1% of the globe [28].

The area of the contrasting "small" independent dust cloud was much smaller (approx. 160,000 km). As the analysis of the IR images showed, such a cloud was comparatively "young", and had not combined with the dust cloud drawn out to the ocean previously (Fig. 3).

The dust-flows registered in the photographs taken from space, come from different parts of the Western Sahara. With the help of the space images it was possible to locate several centers that produce the dust outbreaks. Some of them are located northwest of the Ahhagar foothills (2-3°E, 26°N). It is quite possible, that their formation is associated

with the maximum heating of the dark-colored stony surfaces of this region and subsequent formation of the powerful vertical convective fluxes which then drift towards Erg-Shelly and further over that sandy massif which feeds them with dust.

The second center generating the dust outbreaks is less distinctly outlined in the IR image. It is located southwest of the Ahhagar foothills on the plateau Tassilin-Ahhagar (23-24°N, 3-4°E), and as in the first case, is associated with the intensive heating of the stony surfaces and, probably, penetration of the cooler monsoon. In the area where the monsoon meets the heated surface, the convection significantly increases.

The local dust-flows can be associated with strong deflection of small sand massives. Two such massives are located in the coastal region of the Western Sahara (Agerger region), and judging by the TV images, serve as the center of the local dust outbreaks over the Atlantic. The principal directions of the dust drift are also depicted from the space images. One of the main trajectories of the dust movement goes from center No. 1 over the gigantic sand massif Erg-Shelly southwest of the Adrar plateau and further on to the coast. The sand deposits of Erg-Shelly serve as a feeding source for this dust-flow. The fact that the moving dust-flow masks the hills' tops of up to 600 m elevation south of Adrar plateau (this is seen when the images of 4 and 30 July are compared - Fig. 2a, 2b), enables one to infer that the flow moved aloft up to 0.6 km, i.e. it rose from the ground for at least several hundred meters.

From the region of the second center, the dust cloud moves southwest, judging by the IR images (Fig. 3a), and passing over the lowland of the Niger River, catches the light-colored particles associated with the silt deposits of Niger floods.

2.4 Meteorological Conditions in the Zone of Dust Clouds

As a rule, cloud-free weather or few clouds were observed in the zone of dust outbreak. It was noted also that intensive development of convective cloudiness together with accompanying phenomena takes place at the boundary of the Saharan aerosol layer, or in its absence, over the whole intertropical convergence zone. These observations enable one to assume the aerosol cloud to have certain properties stopping the development of cloud convection and some self-stabilizing mechanism that maintains the dust cloud's spatial structure.

2.4.1 Principal Meteorological Characteristics of the Saharan Aerosol Layer (SAL)

In summer months, the anticyclonic formations over Western Africa favor the heated air and dust outflow over the Atlantic between 10° and 25°N. The aerosol cloud with its base at 0.5-1 km and its top at 4-6 km moves together with the western air flow going as far as 3-4 thousand km from the African continent and reaches the coasts of the North and South America in 6-8 days at an average speed of 15-20 km/hr. The lower boundary of the aerosol layer usually coincides with the upper boundary of the trade wind inversion. Beneath the inversion, a heavily moistened air layer is located, where the trade-wind inversion cloudiness is formed, amounting to 5-8 eights cloud cover. Though the surface air layer contains a great amount of water vapor, the trade wind inversion inhibits the development of convective cloudiness.

The lower boundary of the aerosol layer is usually distinctly pronounced and can be determined by the moment of the horizon disappearance (the mean height of the base is 0.38 km). The lower part of the aerosol cloud is 5-6°C warmer as compared to the normal dust-free tropical air.

Higher, up to the altitude of 4-5 km (the mean value of 4.8 km), a distinctly pronounced colored aerosol layer is located, characterized by a sharp deterioration of visibility down to 500 m, high potential temperature (higher than 40°C) and a sharp decrease of the water vapor content.

The stepped structure of the vertical profile of the absolute air humidity (q) through the aerosol layer is rather typical (Fig. 4). The anomalous overheating remains through the aerosol layer up to the 650 mb level (3.5 km), above which the dusty air turns out to be cooler as compared to the clear atmosphere. At the external boundaries of the aerosol cloud, sharp horizontal gradients of meteorological elements are observed up to $1-2^{\circ}\text{C}$ change in the air temperature and $5-6^{\circ}\text{C}$ change in the dew-point temperature. On the whole, the aerosol cloud presents a large-scale temperature inhomogeneity somewhat lifted over the ocean level and characterized by high self-stabilizing properties.

The analysis of the data from 20 flights in the cloudless tropical troposphere with a strongly pronounced aerosol layer, makes it possible to draw the mean vertical profiles of the meteorological elements and to reveal their most characteristic properties. Figure 4 presents an idealized picture of the air temperature, absolute humidity and wind speed profiles.

The trade wind inversion is smoothed down in the averaged profile of the air temperature, but the general background of the thermal anomaly in the zone of the aerosol layer is pronounced distinctly. Inhomogeneities of the averaged profile of wind speed correlate with the zones of temperature anomalies: the first maximum at the altitude of 2.5-3 km coincides with the mean level of minimum visibility in the aerosol layer and with a maximum of aerosol concentration. The second maximum of the wind speed

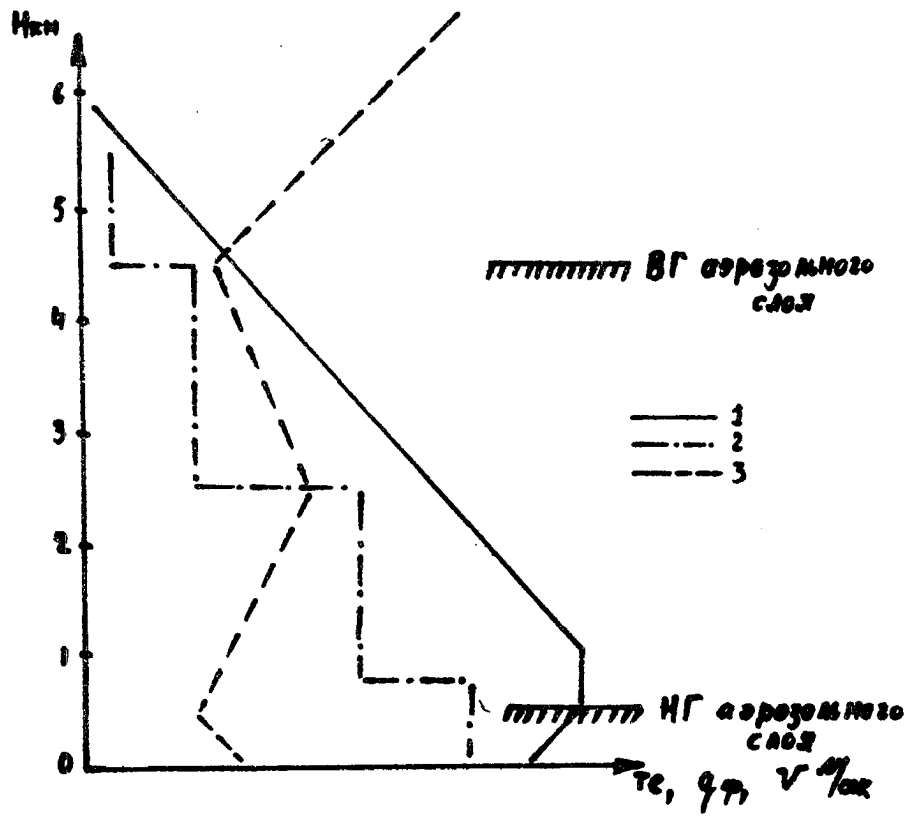


Fig. 4 Typical meteorological conditions in the dust cloud zone.
1 - air temperature
2 - absolute humidity
3 - wind speed

coincides with the top of the aerosol cloud. The distribution of absolute humidity is characterized first of all by the stepped structure, which indicates the stratified character of the aerosol cloud.

Let us discuss a specific synoptic situation during one of the most powerful dust flows on 29-30 July 1974.

2.4.2 Synoptic Situation During the Powerful Dust Outbreak on 30 July, 1974.

In July, the second (after January) largest dust storm is observed in the Western Sahara. At this time the outbreaks originate not because of strong winds, but due to powerful overheating of the lower air layers, intensive convection and formation of baric depressions. When the dust rises to a certain altitude, it is carried away by the northeastern trade wind, and being drawn into the Azores anticyclone circulation is transported over the Atlantic Ocean first eastward, and then to the north and northwest along the periphery of the anticyclone. Gradually, the dust covers all the area occupied by the anticyclone. As a result, an enormous dust cloud is formed which sometimes reaches South America while drifting westward.

For such a distant dust transfer, strong stationary northeastern winds in the lower troposphere are necessary. They occur when the center of the Azores anticyclone drifts to the southeast towards the African coast. At the altitudes over the southern part of the Western Sahara, high baric gradients are formed, which lead to the strengthening of the northeastern trade wind and harmatan.

A similar situation was observed on 29 July, 1974. The center of the Azores anticyclone was located in the extreme south (30°N , 25°W - near surface, and 30°N , 10°W - at the 700 mb level). This caused the increase of the baric gradients, which in turn led to the strengthening of the northeastern trade wind. The anticyclone in the southern hemisphere

drifted northward too. The pressure crest stretched towards the equator, along 20°W ; as if an arch was created between the Azores anticyclone and the southern hemisphere. The intertropical convergence zone was divided into two branches (Fig. 5). The possibility now occurs for air exchange between the northern and southern hemispheres.

Using extensive statistical data from the ATS-III geostationary satellite, TV images, together with simultaneous synoptic data and dust concentration measurements, the American researchers have put forward a circulation model of the powerful dust outbreaks into the Atlantic [29]. According to this model, an atmospheric front is born in the lower atmospheric layers when hot African air meets with the cool and humid Atlantic air mass. This front is clearly traced in TV images as a cloud field generated during an overflow of clean (dust-free) hot African air. Afterwards, this disturbance drifts westward together with dust clouds. In the IR image dated 29 July, 1600 GMT, a cloud ridge stretching from southwest to northeast (along 20°W) and contacting the ITCZ in the south stands out particularly clearly. Obviously, it is associated with such a front in the clear air zone. Over the West African coast a cyclonically bent dust cloud connected with the northern extreme of this surface front in the area of the dusty air outbreak can be traced from the shore to 12°W and from $18-20^{\circ}\text{N}$. The surface front is expressed as a pressure gradient.

In the surface pressure chart (Fig. 6), a low pressure zone with two centers is present: one in the dust cloud area, the other coincides with the cloud front. The positioning of this surface front corresponds to the beginning of a new hot Saharan air outbreak into the ocean.

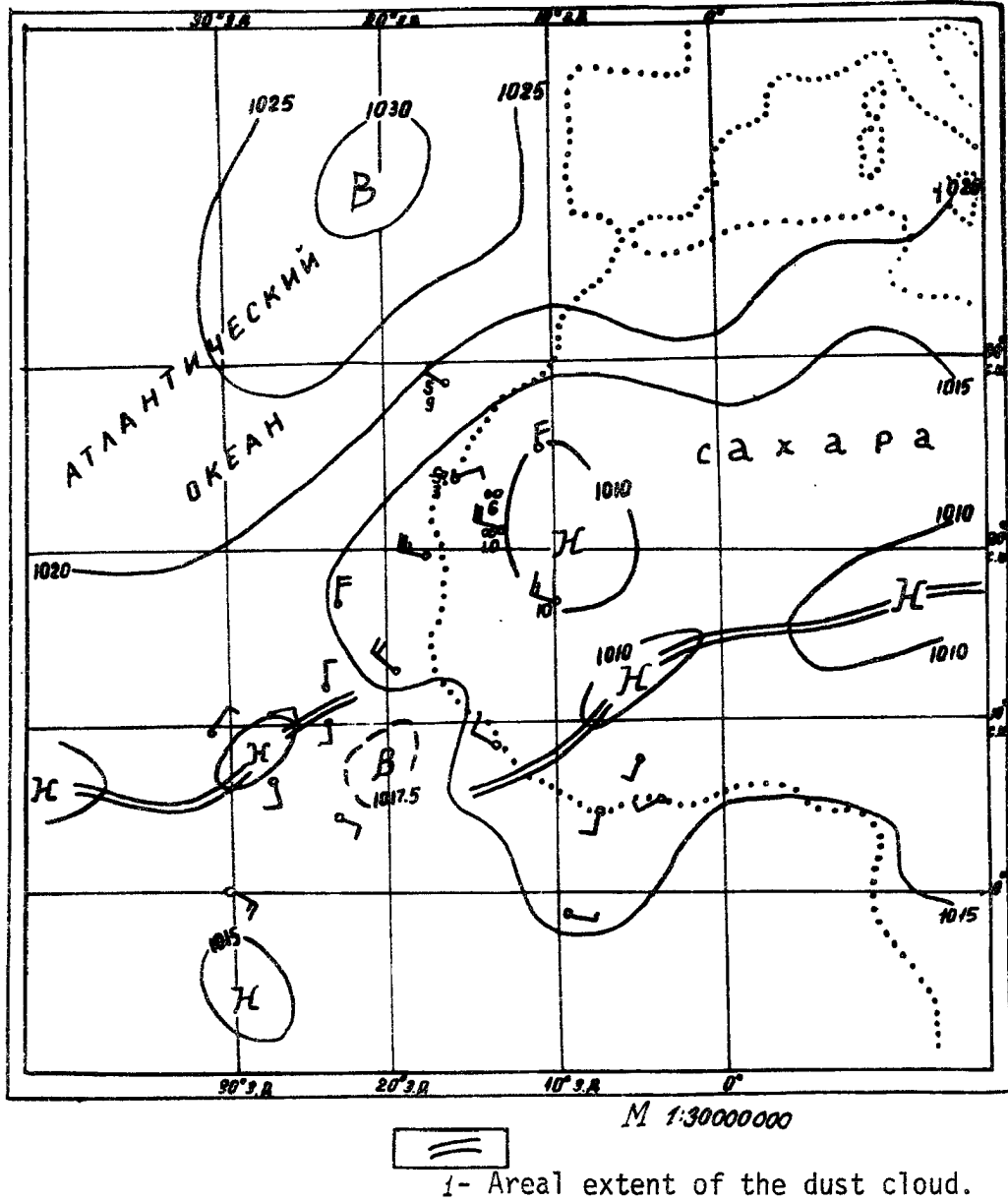


Fig. 5 The surface synoptic map of the dust outbreak area of 30 July, 1974, 0000 GMT.

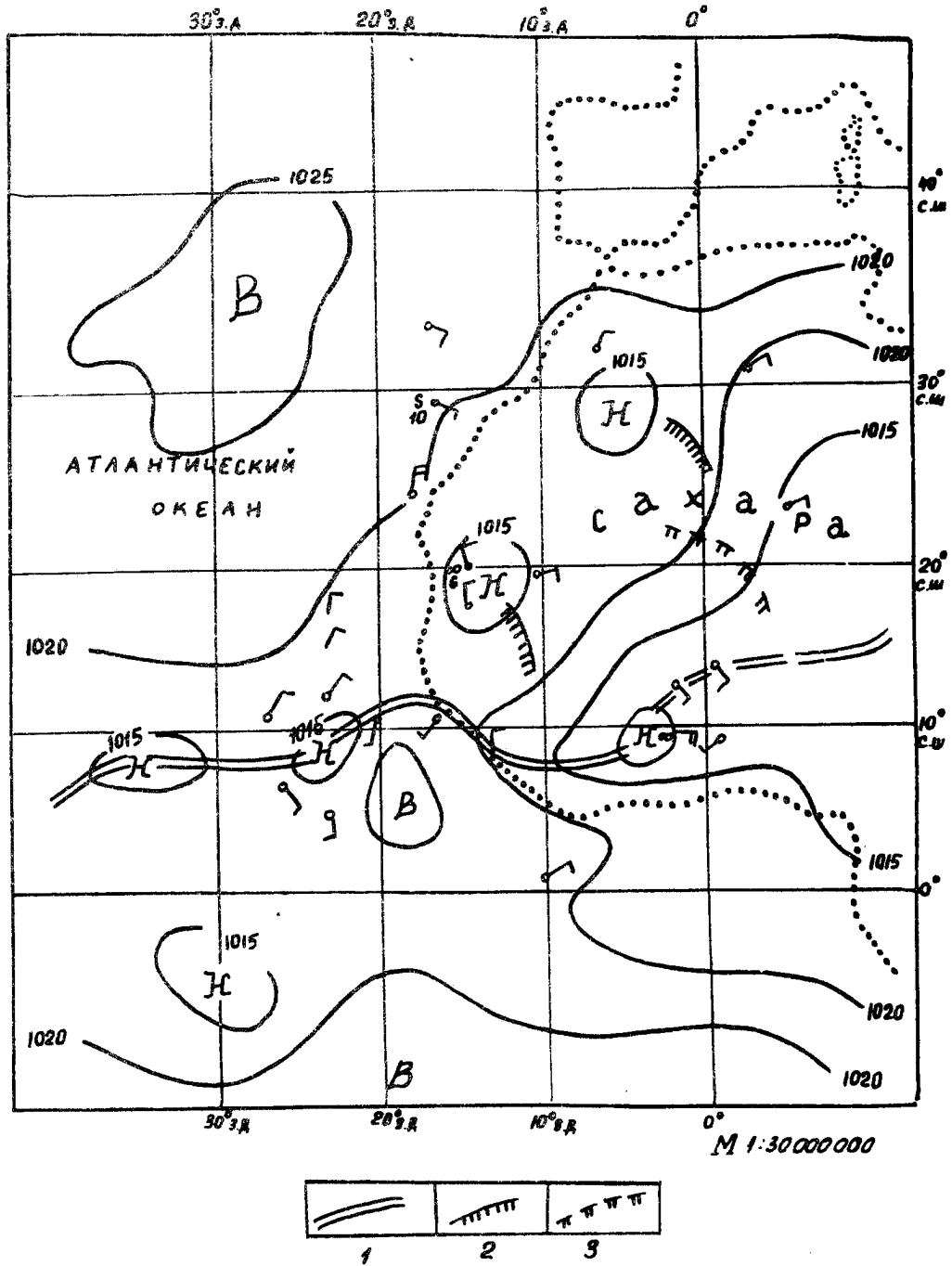


Fig. 6 The baric topography map AT-700 of 30 July, 1974, 0000 GMT.
Notations:
1) The areal extent of the dust cloud.
2) The dust cloud boundaries obtained from the TV images.
3) Direction of the dust-wind fluxes.

In the Western Sahara, the dust storm centers originated near the surface, and they reached their maxima in the afternoon of July 29 (Fig. 6). One center with the coordinates of 18°N , 8°W was formed as a result of cool western monsoon air colliding with dry and hot eastern flows. The second center arose in the western region of the central Sahara (31°N , $0-5^{\circ}\text{W}$) due to the formation of the powerful convective fluxes when the surface was strongly heated. For the same reason, the third center of dust storms was produced in the region of $5^{\circ}\text{W} - 0^{\circ}$ and $20^{\circ}\text{N} - 25^{\circ}\text{N}$. The first two centers can be spotted in the synoptic map and IR images, the third center only in the image. As is seen from the 29 July IR images (Fig. 3a), the enormous dust cloud was caused by the lifting of the dust from the first center of the storm, with its subsequent transfer over the Atlantic along the Azores anticyclonic circulation. The analysis of the baric topographic maps has shown that this dust transfer over the Atlantic occurred at the altitude of about 3 km (Fig. 7). On 30 July, a further formation of the gigantic dust flow over the Atlantic was observed, as a result of dust transfer from the other dust storm centers into the high-altitude atmospheric circulation.

2.4.3 Dynamics of the Dust Flow From Africa on 29-30 July, 1974.

The joint analysis of the IR and TV images obtained from a geostationary satellite on 29-30 July, 1974, makes it possible to trace the dynamics of development of the dust cloud under consideration. The first IR image in which a dust flow was spotted, was seen at 1600 on 29 July. At this time two storm centers were easily seen in the form of dust clouds (one in the region of 18°N , 8°W , the other in the region of 31°N , 0°W). Judging by the image, the first center was the source of the

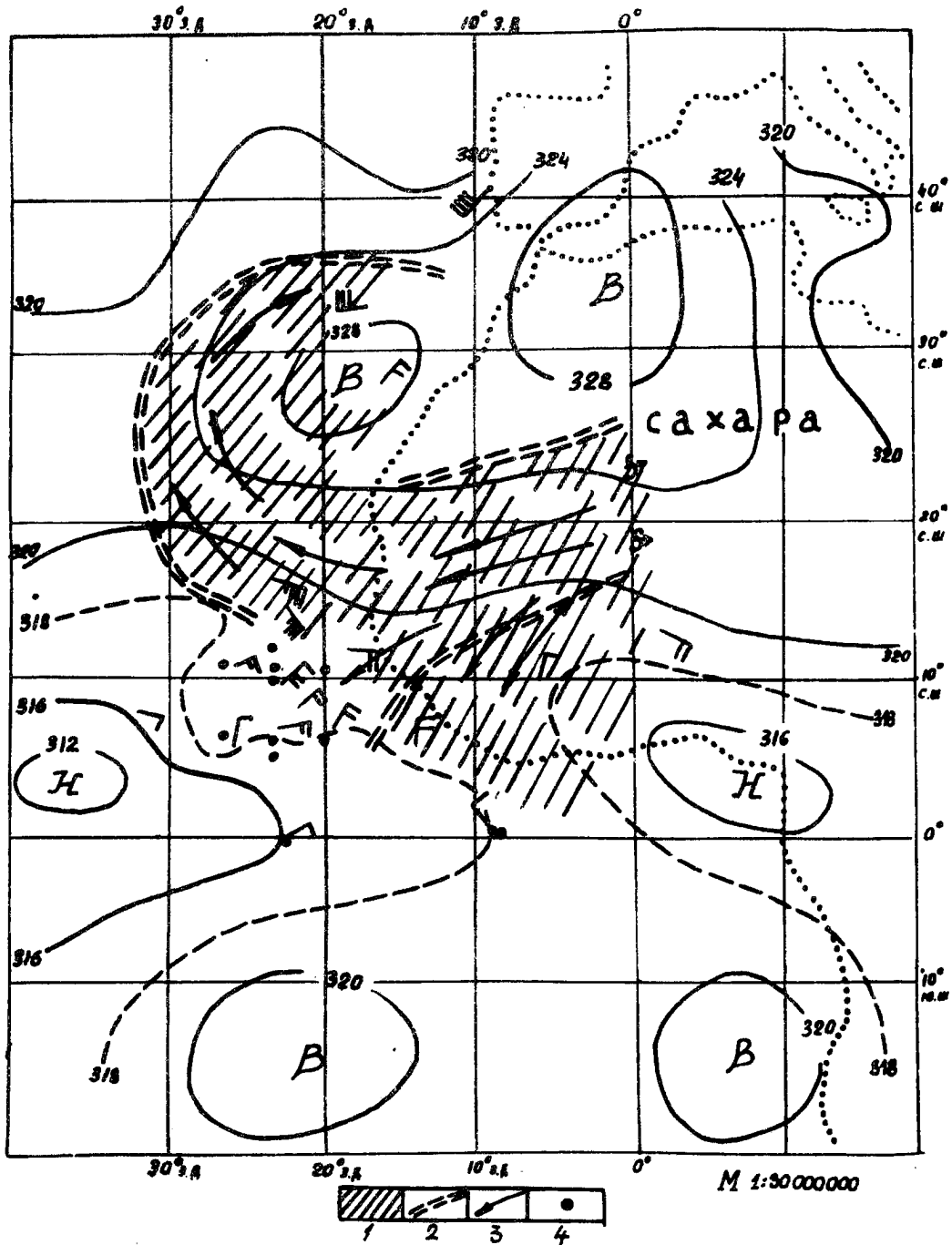


Fig. 7 The surface synoptic map of the dust outbreak of 29 July, 1974, 1200 GMT.

Notations:

- 1) The intertropical convergence zone.
- 2) The dust storms front location.
- 3) An approximate location of the dust storms front.
- 4) Location of the Soviet weather ships participating in GATE-74.

dust cloud registered at this time over the Atlantic. The second center was identified by a stretched broadening cloud consisting of individual streams.

From the analysis of the subsequent images obtained on 29 and 30 July, one can see the way the dust transfer from the second center over Africa to the Atlantic happened (Fig. 3a, 3b). Comparing the IR images obtained at 1600 and 2100 on 29 July, we see that the front edge of the cloud drifted a distance of about 5° in five hours, latitudinally, i.e. this transfer went on with the speed of about 30 m/sec. Since the network of aerological stations in the region considered is rather sparse, this fact is an important additional source of information about the northeastern trade wind speed at the altitudes of 1-3 km.

The simultaneous analysis of TV images (1800) and the surface relief showed that the base of the cloud was higher than 600 m. Later on, the dust cloud drawn into the Azores anticyclonic circulation, drifted over the ocean filling the Azores anticyclone (Fig. 3). In 10 hours (0700, 30 July), the frontal part of this outbreak was near the meridian of 25°W . The transfer speed appeared again to be 30 m/sec.

Now, let us trace the changes of the dust cloud boundaries over the aquatic area. At 1600 on 29 July, the front(western) cloud edge reached 30°W , the northern one - 35°N , and the southern one was at about 10°N . It is interesting to single out a small spur of the dust cloud which, as if breaking the ITCZ, edges itself between its two branches, reaching 10°N and possibly moving even further to the south. In the image obtained at 1600 on 29 July (Fig. 3a) the cloudiness located along the western boundary of this dust spur is traced up to 9°N . The westward reach of the spur went as far as 21°W . In five hours (2100), the western edge of

the main cloud reached 33°W, and the southern spur was observed at 23°W. The cloud spur drifted southward to 7°N (further southward movement of dust is difficult to discern). At 0700 on 30 July, the western boundary of the main cloud reached 35°W, and the southern spur - 25°N. The cloud westward drift went at a speed of about 10 m/sec.

On 29-30 July, 1974, some of the GATE ships happened to be in the region of the cloud's southern spur. While only "Poryv" was in the cloud at 1600, 29 July, at 0700 on 30 July, "Vize" and "Korolov" were embraced by the dust zone as well. The ship data made it possible to obtain information on the optical and microphysical characteristics of the dust cloud.

Let us turn now to a discussion of these observational data aiming at the subsequent consideration of the aircraft aerosol measurements results (Chapter 4) both in the dust zone and beyond it.

3. MICROPHYSICAL AND OPTICAL CHARACTERISTICS OF THE DUST AEROSOL AS INFERRED FROM THE SHIP DATA.

As was already noted, the region of the Atlantic from 22°N to 10°N and down to 40°W (the so-called "Sea of Darkness") [18] is characterized by systematic dust outbreaks over the ocean from the African deserts due to the northeastern trade wind. This feature is superimposed on all the specific aerosol optical characteristics of the atmosphere in this part of the global ocean.

Figure 8 depicts the dust fallout regions into the Atlantic on three different occasions [8]. The first maximum fallout is observed in February and reaches 21.6%, the second one in August (10.4%) and the minimum of 1.6% in November [9]. Up to the present time, the atmospheric aerosol research in the "Sea of Darkness" has been qualitative. The first quantitative data were obtained in March-July 1970 by the scientific research ship "Akademik Shirshov" [5] and in 1972 - during the USSR TROPEX-72 national experiment by weather ships "Musson" [10] and "Akademik Kurchatov" [4, 11, 12].

The specific nature of the atmospheric aerosol and its radiative characteristics in the region of "Sea of Darkness" is distinctly presented through the data obtained during TROPEX-72 by the ship "Musson" while it performed a meridional cross-section along the 19 W longitude from 30 N to 15 S. These data are represented in Fig. 9 [10].

In the region under consideration, the aerosol and optical properties of the atmosphere depend significantly on the air masses' trajectory, especially in the lower 2 km layer. In the beginning of the meridional cross-section from 30°N to 25°N, the mean wind in the 2 km layer gradually turned from west to north. At these points, the pure oceanic air masses

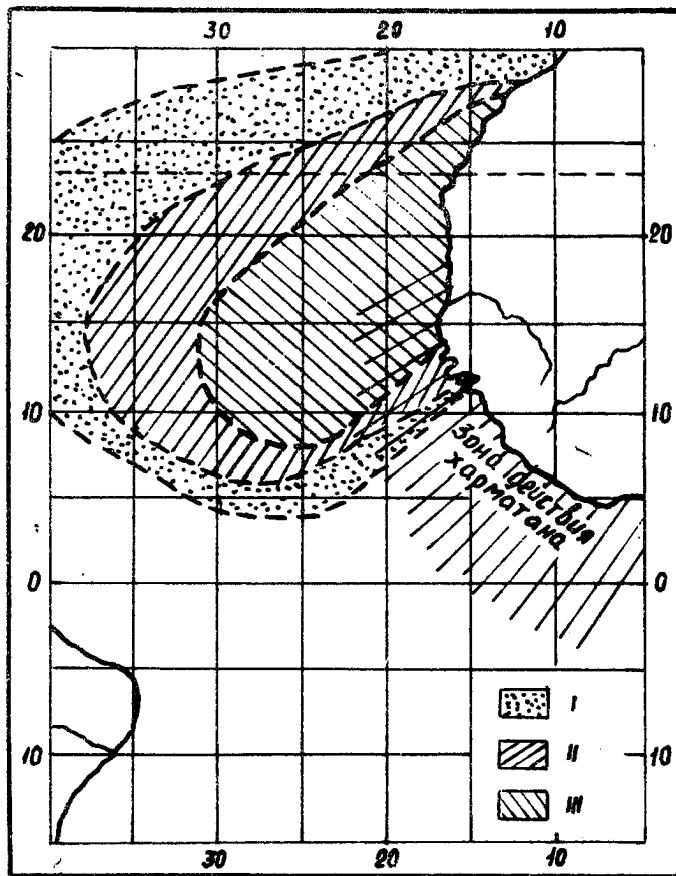


Fig. 8 Regions of the dust fall-out in the Atlantic from the data of Ref. 8:
1 - rarely observed
2 - more often
3 - very often

entered the investigated region; these air masses were characterized by low aerosol particle concentration and slight aerosol attenuation of the solar radiation. The northeastern trade wind dominated over the band of 22-10°N. This area clearly stands out in Fig. 9 due to its aerosol-radiative characteristics. Radiation attenuation due to aerosol, concentrations of all the measured particle fractions, and the weight concentration reach their maxima in this region.

The filter exposed from 15 to 10°N turned out to be covered by a layer of yellow sandy dust. The spectra of particle size registered along the axis of the "Sea of Darkness" (14°N, 19°W) are given in Fig. 10.

For comparison, the mean spectra of the surface air layer aerosol size observed in the countryside over the Central part of the USSR European territory under the conditions of high atmospheric transparency (meteorological visibility $S_M = 30$ km) and dense haze ($S_M = 2$ km) are shown in the same Figure [13].

The gigantic particle concentration over the "Sea of Darkness" greatly exceeds the mean concentrations registered over the USSR central European area in dense haze. Minimum concentrations measured over the ocean (Fig. 10, curve 3) are tenfold lower than those found in the surface air layer over the USSR central European area.

The second meridional cross-section during the TROPEX-72 made also by ship "Musson" along 26°W, from the equator to 22.5°N (27 August - 1 September) showed that the maximum aerosol concentrations were observed in the zone of maximum dust fallout over the "Sea of Darkness". As a rule, the particle concentration along 26°W turned out to be lower than the corresponding values along 19°W. Apparently, this is associated with the ship moving away from the African continent, over which the

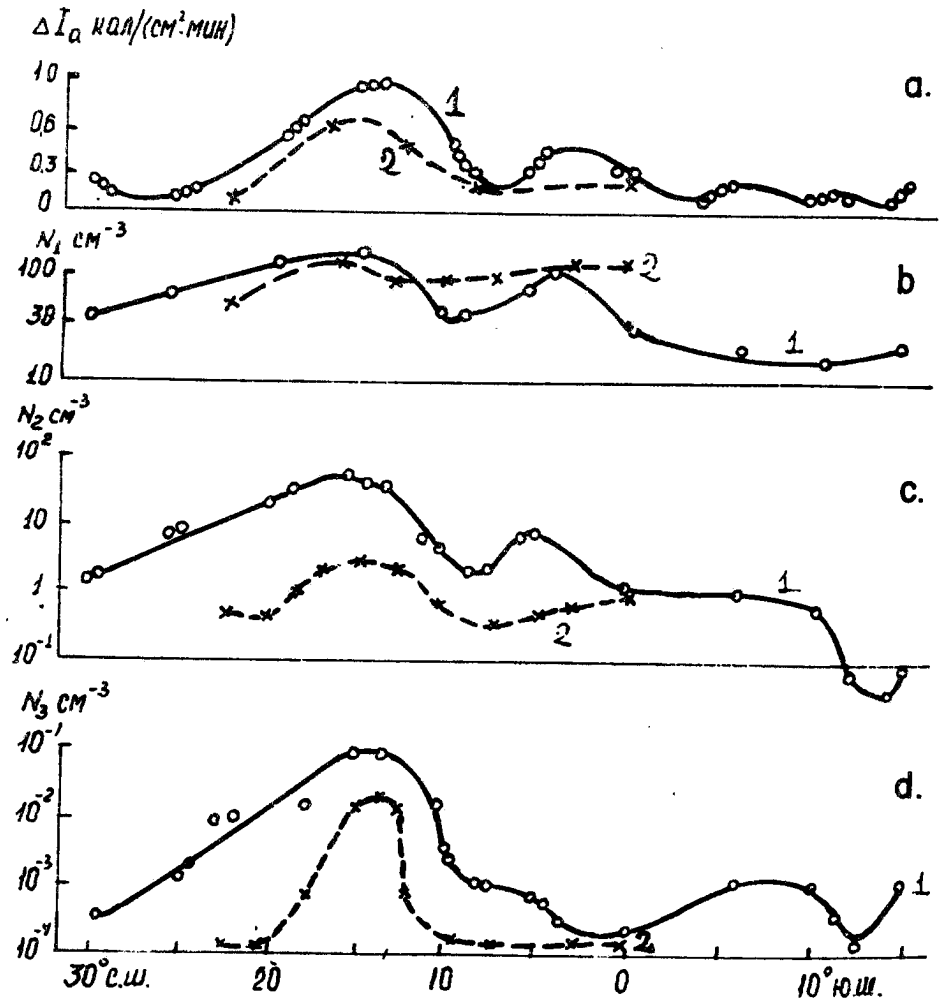


Fig. 9

Meridional profiles of aerosol characteristics from the TROPEX-72 data:

- a - direct solar radiation attenuation due to aerosol
- b - condensation kernels' concentration
- c - large particles' concentration
- d - gigantic particles' concentration

- 1 - meridional profile along 19°W
- 2 - meridional profile along 26°W

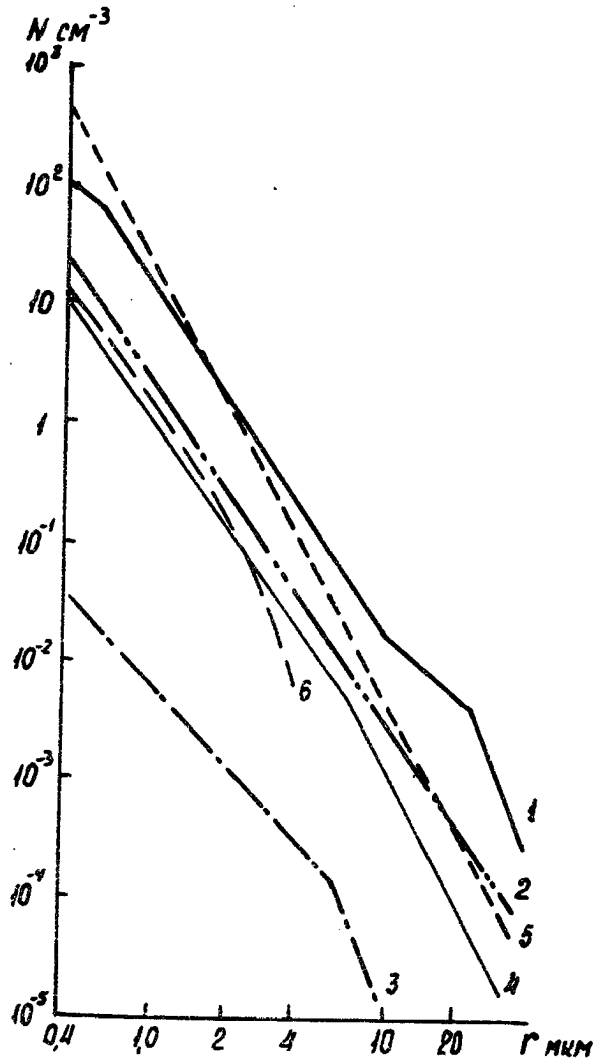


Fig.10

Spectra of particles' size from the TROPEX-72 data:
1, 2, 3 - oceanic, registered in the region of maximum (19°W, 14°N) and minimum (19°W, 14°S) particles' concentrations
4, 5 - middle spectra of the continent aerosol at meteorological visibility of 30 and 2 km [23].
6 - spectrum of particles' size from the 30 July, 1974 data (equator, 10°W).

trade winds are constantly blowing. For the 12 to 24°N region, the shortest distance from Africa to the 19°W meridian constitutes 300 km, while for 26°W, it is about 900-1000 km.

The decrease of large and gigantic particle concentration observed when moving away from Africa, testify to the continental origin of the main bulk of aerosol particles for this region of the Atlantic. The atmospheric particle concentration registered at 19° and 26°W, practically coincide, which is associated with their slow fallout and washout from the atmosphere.

Comparison of the radiation attenuation values due to aerosol, with the aerosol particle concentration in the near-water atmospheric layer has shown that a maximum of aerosol attenuation (transparency coefficient $P_{aer.} = 0.52$, $P_2 = 0.43$) is observed in the areas of the highest aerosol concentrations.

As is known, the radiation absorbed by water vapor and aerosol particles heats the lower troposphere. According to the data of Ref. 14, the value of radiative heating in the lower troposphere in middle latitudes is near 0.06 - 0.1°/hr for clear summer days, reaching in some layers 0.2°/hr. The particle content in the atmosphere over the "Sea of Darkness" is high, and the total atmospheric water vapor content reaching 4-5 cm is much higher than the middle latitudes [15].

Therefore, one can expect a more intensive air heating due to absorption of solar radiation by aerosol particles and water vapor. Measurements and calculations of aerosol absorption carried out in [14, 16] have shown that radiative heating can lead to the formation of an inversion in the lower tropospheric layers. In Fig. 11, the meridional trend of the air temperature variations over the tropical Atlantic (19°W) at the

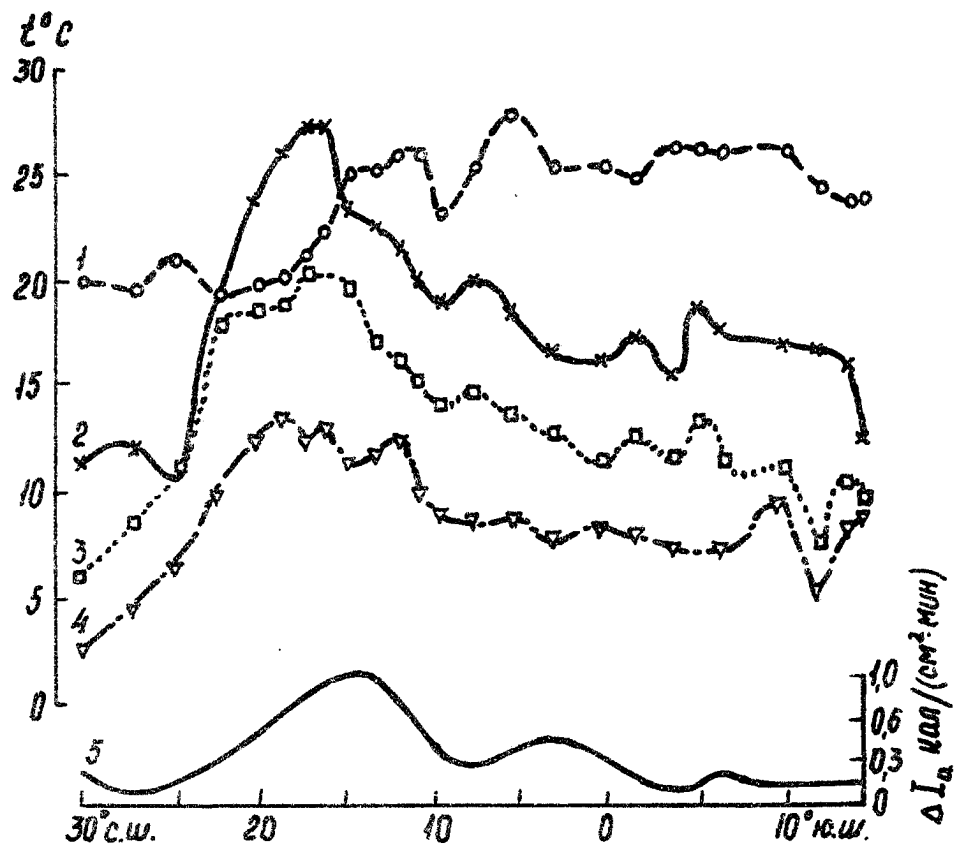


Fig. 11 Comparison of the air temperature meridional curves at the altitudes of 27 m (1), 1000 m (2), 2000 m (3), 3000 m (4), and the variation of the value of direct solar radiation attenuation due to aerosol (5).

altitudes of 27, 1000, 2000 and 3000 m, plotted according to the data of four times-a-day soundings from aboard the "Musson" is compared with the simultaneously measured intensity of the aerosol attenuation of solar radiation [10].

As follows from Fig. 11, the maximum temperature of +28°C was registered in the sub-equatorial zone at 5°N in the near-the-water air layer. The maxima of air temperatures at the altitude of 1-3 km are shifted further north (13-20°N). The region of the maximum air temperatures in the lower 3 km layer is located in the area of the "Sea of Darkness" and correlates with the zone of the maximum direct solar radiation absorption by the aerosol. The maximum air temperature at the 1 km altitude correlates well with the area of maximum aerosol absorption through the meridional cross-section over 26°W.

However, at the altitudes of 2 and 3 km such a correlation was not observed. It should be mentioned that though the causes of the trade wind inversions' generation are well known, namely: the downward movement of air in the anticyclone, the intrusion of air masses into the tropical zone; the intensive solar radiation absorption by aerosol particles and water vapor, will play a certain role in the inversions' deepening over the "Sea of Darkness".

The constant presence of dust alters the optical properties of the atmosphere over the region of the "Sea of Darkness". As the results of the expedition TROPEX-72 [4] have shown, the principle feature of radiation attenuation in the 0.35 - 1 μm region of the spectrum over this oceanic area is similar to the peculiarities of radiation attenuation over desert areas, including the increase of attenuation near $\lambda = 0.38 \mu\text{m}$, which is to all appearances caused by absorption by haematite particles (Fe_2O_3) [10].

Table 1 presents examples of comparing the optical characteristics of the atmosphere and the total water vapor content (W) for the Kara-Kum sandy desert and the sub-equatorial Atlantic subjected to the Saharan dust outbreaks. Here P_2 is the integral atmospheric transparency coefficient reduced to the mass $m = 2$ through S. I. Sivkov's technique [18]; τ^*_λ is the aerosol optical thickness of the atmosphere; n is the index of power to which the wavelength is raised in the Angstrom formula $\tau^*_\lambda = \beta\lambda^{-n}$ that characterizes the degree of the aerosol attenuation selectivity. Aerosol optical thickness at $\lambda = 1 \mu\text{m}$ corresponds to the Angstrom index of the atmospheric turbidity β .

Let us point out that according to data measured during TROPEX-72 and GATE, the aerosol attenuation followed the usual dependence of $\tau^*_\lambda = \beta\lambda^{-n}$.

Table 1. Optical characteristics of the atmosphere in the Kara-Kum Desert in the tropical zone of the Atlantic.

Place of Observation	Date	P_2	τ^*_λ		n	W cm
			$\lambda=0.33 \mu\text{m}$	$\lambda=1 \mu\text{m}$		
The Atlantic Ocean	24.06	0.59	0.345	0.271	0.2	3.2
Kara-Kum Desert	10.09	0.58	0.345	0.254	0.1	2.7
The Atlantic Ocean	24.06	0.55	0.421	0.322	0.2	3.1
Kara-Kum Desert	16.09	0.67	0.450	0.115	0.2	0.7
The Atlantic Ocean	20.07	0.73	0.198	0.097	0.7	4.9
Kara-Kum Desert	19.09	0.77	0.184	0.078	0.8	0.6

As is seen from Table 1, the values of aerosol optical thickness can be close to each other for the two global regions under consideration, in spite of the great difference in water content. In those rare cases when the values of W were of the same order, not only spectral but also the integral characteristics of transparency coincided as well. In other cases, a heightened water content over the equatorial Atlantic caused the decrease of integral transparency.

The powerful dust flows from the continent - the result of dust storms over the African deserts, change the optical and aerosol characteristics of the atmosphere even more.

Table 2 and Fig. 10 show the effect of a dust cloud outbreak on optical and aerosol characteristics of the atmosphere in the sub-equatorial zone of the Atlantic as inferred from the data obtained during TROPEX-72 by the weather-ships "Akademik Kurchatov" and "Musson". The ships were in the bunkering area near the Mauritanian coast under coordinates of $\phi = 18^{\circ}8'N$, $\lambda = 16^{\circ}5'W$ [4, 10, 12]. In the given season, the boundary between the Azores oceanic anticyclone and the summer baric depression existing over the Sahara passes through that area. The high-altitude northeastern winds were carrying great amounts of dry dust through which the higher clouds could hardly be observed (the stable northwestern winds enveloped only the lower layers). The effect of the dust flow was so powerful that the mean transparency coefficient for the whole atmosphere reduced to mass 2 constituted 0.58 (the integral optical thickness $\tau_2 = 0.372$), reaching in some cases 0.43 ($\tau_2 = 0.845$). Meteorological visibility dropped down to 8.7 - 12 km, the values of n and β reached 0.2 and 0.34, respectively. The last line of Table 2 gives the mean values of the enumerated parameters, typical for the sub-equatorial zone of the Atlantic Ocean

during this period. The values of the integral aerosol atmospheric transparency coefficient and the integral aerosol optical thickness calculated according to [18] are given in brackets. Note, that the obtained values of atmospheric transparency for the near-water layer agree with the values in [34], according to which the "Sea of Darkness" is characterized by meteorological visibility of about 15 km, and 25 to 30 km for the equatorial Atlantic. The spectrum of aerosol particles registered on board the "Musson" ship [10] at the same time is presented in Fig. 10. Curve 2 corresponds to the particle size distribution obtained on 1 August, 1972. Curve 3, as was stated above, was obtained in a practically dust-free region of the Atlantic at 14°S, 19°W. As follows from Fig. 10, particle concentrations differ by the order of three for all the sizes, the particles with radius $r > 10 \mu\text{m}$ being practically absent in the pure oceanic aerosol.

Table 2. Atmospheric transparency in the zone of the dust outbreak.

Weather ship "Akademik Kurchatov"	Vertical transparency of the atmosphere		$\tau_h^* = \beta\lambda^{-n}$		Horizontal transparency of the atmosphere	
	P_2	τ_2	n	β	S_M, km	α, km^{-1}
1 August 1972	0.58(0.69)	0.545(0.372)	0.2	0.34	12	0.250
Averaged for the period of TROPEX-72	0.66(0.78)	0.416(0.249)	0.6	0.12	30	0.100

Three dust outbreaks from the African continent were recorded during the GATE from aboard the ship "Passat" lying at the equator under

$\lambda = 10^\circ\text{W}$. In this region, the increase of the atmospheric dust content was mainly associated with the dust transfer from the central and southwestern regions of Africa by the so-called harmatan wind.

Table 3 gives the value of the atmospheric optical characteristics observed under maximum turbidity on the given days and the values averaged over the first and second phases of GATE. As follows from Table 3, the most powerful dust outbreak in this region was observed on 11 August (this outbreak has lasted for several days). In this period, both the vertical transparency of the whole atmosphere, and the horizontal transparency of the near-water air layer have dropped. Concentration of large aerosol particles $N_d > 0.63 \mu\text{m}$, reached 30 cm^{-3} .

As was stated above, the dust flow to the ocean observed on 30 July covered practically the whole area of the ship's location. During that period, a quick strengthening of atmospheric turbidity was recorded, the change being determined by the remoteness of each given point from the African continent.

As follows from Table 3, the optical characteristics of the atmosphere observed on 30 July 1974 at the point with $\phi = 0$, $\lambda = 10^\circ\text{W}$, are very close to those observed on 1 August 1972 over the "Sea of Darkness" (Table 2).

It must be pointed out that the dust outbreak registered by "Passat" on 15 July was not observed over the "Sea of Darkness" and was thus obviously generated by the local wind ("harmatan"). The rise of the "n" value with the appearance of African dust should be noticed. The separate measurements of pure oceanic aerosol showed that aerosol attenuation in the spectral region of 0.35-1 microns is close to neutral [4, 26], while the intrusion of continental aerosol could increase the

Table 3. Values of the atmospheric optical characteristics observed under maximum turbidity.

Weather-ship "Passat"	Vertical transparency		Horizontal transparency		$\tau_{\lambda}^* = \beta \lambda^{-n}$		Nd > 0.63 μm (cm^3) ⁻¹
	P_2	T_2	S_m	α	n	$\beta = \tau_{\lambda=1\mu\text{m}}^*$	
$\phi = 0, \lambda = 10^\circ\text{W}$							
15 July, 1974	0.61(0.72)	0.495(0.328)	17	0.180	0.9	0.29	15
Phase I Average	0.71(0.84)	0.342(0.174)	45	0.067	0.2	0.14	8.1
30 July, 1974	0.58(0.69)	0.545(0.372)	16	0.187	0.6	0.30	23
11 August, 1974	0.50(0.59)	0.694(0.528)	8.0	0.372	-	-	30
13 August, 1974	0.59(0.70)	0.528(0.356)	-	-	0.9	0.22	16
14 August, 1974	0.59(0.70)	0.528(0.356)	-	-	0.9	0.22	14
Phase II Average	0.68(0.81)	0.386(0.211)	40	0.075	0.8	0.16	8.5

α = aerosol attenuation coefficient.

selectivity of aerosol attenuation. The area where "Passat" lay was constantly under the influence of the dust outbreaks during the Phase II so the value of "n" practically did not vary.

The form of the indicatrix of light scattering $\rho(\gamma)$ in the near-the-water layer changes significantly under the influence of a dust outbreak into the ocean as well. Fig. 12 gives the indicatrices of light-scattering obtained on 11 August, 15 July, and the indicatrices typical of pure oceanic aerosol under meteorological visibilities of 40 and 100 km. As follows from Fig. 12, the form of the indicatrix changes with decreasing transparency, stretching forward and acquiring a more pronounced maximum at a scattering angle $\gamma = 0^\circ$ and a minimum in the region of $\gamma = 110-120^\circ$. The asymmetry coefficient, K, increases from 1.8 at $S_m = 100$ km to 12 at $S_m = 7.7$ km (curve 1). According to the TROPEX-72 [17] classification the GATE data for the near-the-water layer in the presence of dust correspond to the 6th and 7th class indicatrices of the "sharp" type. Under normal conditions, the light-scattering indicatrices of the 4-5th class of the 'sharp' type, analogous to curve 3 in Fig 12, can be most often observed in the near-water atmospheric layer over the ocean.

The actinometric data obtained on many ships have made it possible to evaluate the effect of the dust flows from the African continent on the optical properties of the atmosphere over the entire GATE area. From the data of ten Soviet ships (Fig. 13), the spectral atmospheric transparency coefficient (P_2) the turbidity factor (T), and the integral optical thickness of the atmosphere (τ) were calculated. The integral atmospheric coefficient (P_2) was calculated after S. I. Sivkov's technique [18], according to which the direct solar radiation was reduced either to the sun elevation $h_\odot = 30^\circ$, or to the relative atmospheric mass,

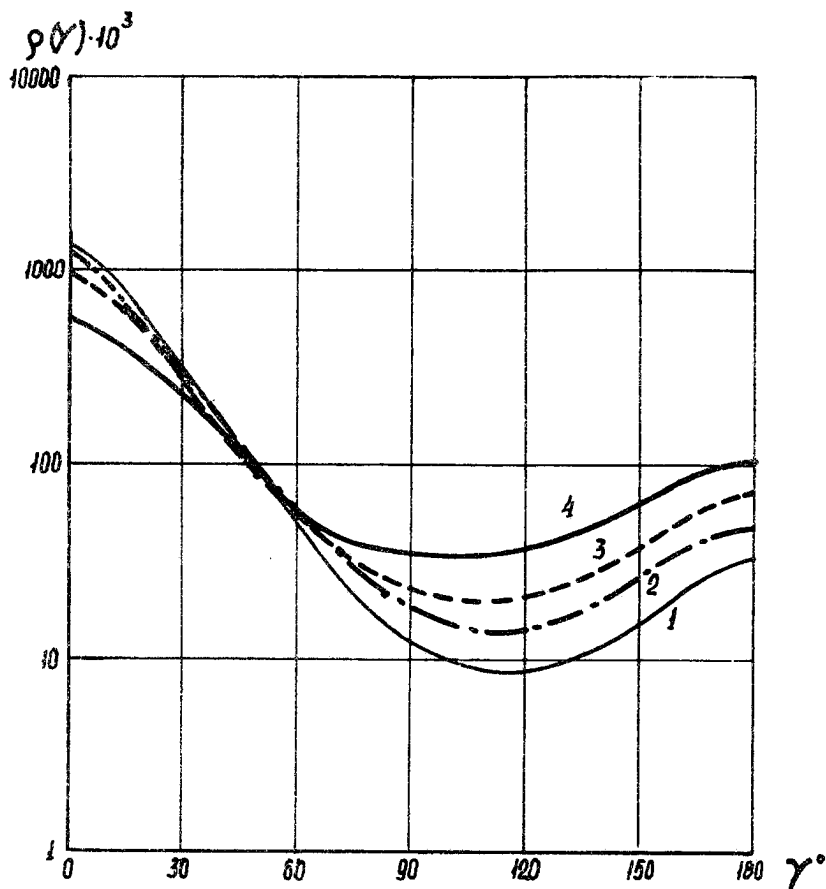


Fig.12 Light-scattering indicatrices in the near-water atmospheric layer:
1 - 11 August, $S_m = 7.7$ km, $K = 12$
2 - 15 July, $S_m = 17$ km, $K = 6.7$
3 - 30 August, $S_m = 40$ km, $K = 4.4$
4 - 26 August, pure oceanic aerosol, $S_m = 100$ km, $K = 1.8$

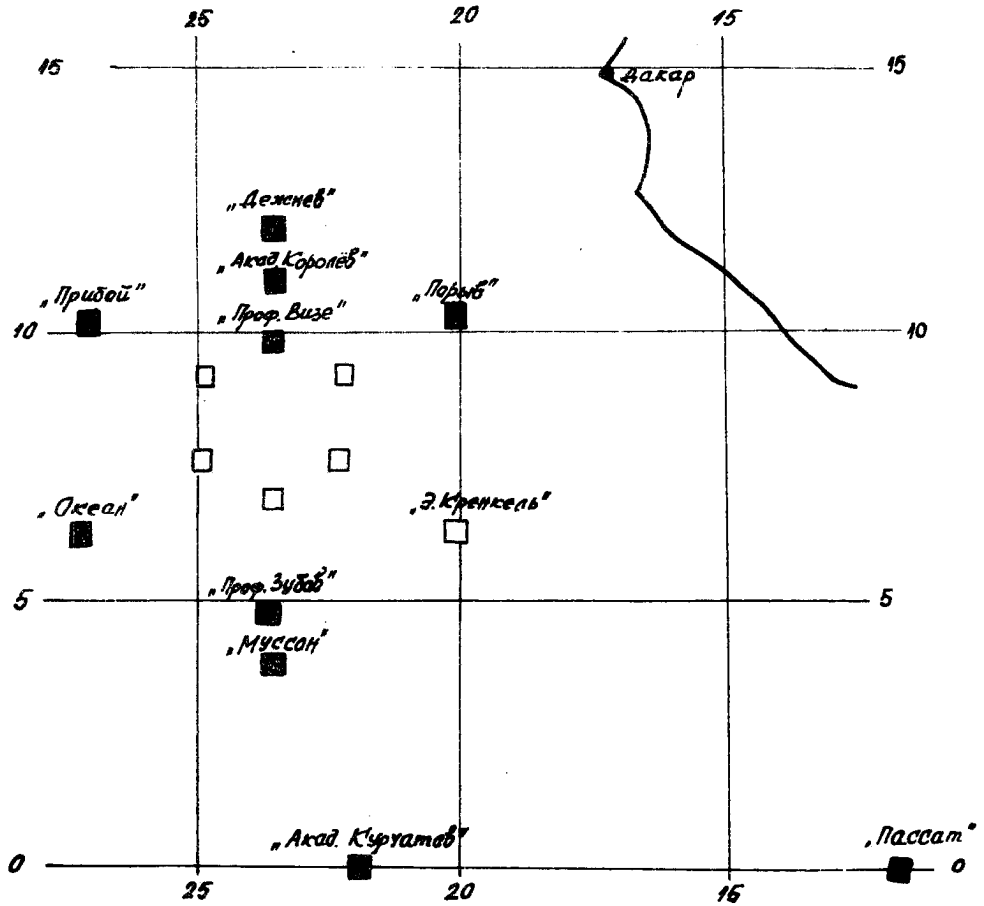


Fig. 13

The scheme of ships' location in the GATE test area (the shaded squares denote the ships, the actinometric data from which were used for preliminary processing).

$m = 2$, as well as to the average distance between the earth and the sun. In this case, the atmospheric transparency coefficient is calculated by the formula

$$P_2 = \sqrt{\frac{S_{m=2}}{S_0}}$$

where $S_0 = 1.98 \text{ cal/cm}^2\text{min}$.

For these calculations, only those intensities of direct solar radiation measured by the AT-50 actinometer were chosen which were acquired under the condition of the open solar disc (θ^2). Thus, not all the data could be processed because of the large amount of clouds for the ships located in the ITCZ.

Location of the weather ships at different points of the GATE test area has made it possible to assess the effect of the dust flows from the African continent on the optical characteristics of the entire region under investigation. For example, the dust flow from Africa in early July was traced by most ships. At first a powerful dust outbreak was observed by "Poryv" lying nearer to the African coast than the other ships. The data from "Poryv" showed that the first dust outbreak occurred during 1-6 July. These dust outbreaks lowered the atmospheric transparency down to $P_2 = 0.58-0.60$. Moving further, the dust cloud reached the ships "Akademik Korolov" and "Professor Vize" on 3-7 July, decreasing the atmospheric transparency down to $P_2 = 0.58-0.60$.

On 4-7 July, the cloud approached the ship "Priboy", the most distant from Africa and located along $10-12^\circ\text{N}$. As a result of a powerful dust outbreak, the ships "Professor Zubov" (7-9 July), "Musson" (8-10 July), and "Okean" (10-11 July) registered the decrease of the atmospheric transparency coefficient down to 0.65-0.66; 0.66; 0.61-0.62, respectively. The ship "Dezhnov" that stayed clear of the ITCZ happened not to be embraced by the dust cloud.

In this case the transparency coefficient was 0.73-0.75 during the whole period of the dust outbreak. The second wave of the dust outbreak came several days later. "Poryv" registered it on 9 July ($P_2 = 0.60$), and the other ships fixed it with a time lag of several days: "Professor Vize" on 10-11 July ($P_2 = 0.63$), "Akademik Korolov" on 11-12 July ($P_2 = 0.60$), "Priboy" on 10-12 July ($P_2 = 0.59$), "Okean" on 10 July ($P_2 = 0.61$), "Musson" on 14 July ($P_2 = 0.64$).

The third wave of the strong atmospheric turbidity was registered on 28-30 July by the ships "Poryv", "Professor Vize", "Dezhnov", "Priboy", when the atmospheric transparency coefficient decreased sharply down to 0.59-0.63. In the zone of the other ships' locations, the atmospheric turbidity was quite high: $P_2 = 0.70-0.75$ ("Professor Zubov", "Musson", "Okean").

On 3-4 August and 10-11 August, the ships "Poryv", "Professor Zubov", and "Priboy" registered the powerful dust outbreaks which decreased the atmospheric transparency coefficient down to 0.60. The second wave of the atmospheric turbidity reached the ships "Professor Zubov" and "Musson" on 14 August.

4. AIRCRAFT AEROSOL OBSERVATIONS

The IL-18 aircraft based in Dakar was equipped with the following complex of aerosol instrumentation:

- an impactor effective for capturing the particles of $r \geq 0.2 \mu\text{m}$;
- a filtering arrangement with FPA filters for analyzing the chemical composition and dispersion of aerosol with $r \geq 0.03 \mu\text{m}$;
- a photoelectric counter registering numerical concentration and dispersion of the particles with $r \geq 0.2 \mu\text{m}$.

One of the main goals of aerosol investigations was to study 1) the processes forming the Saharan dust layer, 2) the processes of the layer wash-out from the atmosphere, 3) interaction of the continental dust with marine aerosol, 4) the chemical composition of aerosol.

Aircraft observations have made it possible to study the time-spatial variability of the dust cloud, and the dust transfer from Africa towards America over the Atlantic. During the GATE, the thickness of the dust layer varied from 1-1.5 km to 4-4.5 km. The central part of the dust layer was usually at the level of 3-4 km. The region of the "Sea of Darkness" was characterized by a distinctly pronounced aerosol layer of specific structure: the highest numerical concentration of aerosol particles at the boundaries of the dust layer and the lowest numerical concentration in the center of the layer, where at the same time the highest mass concentration of dust particles was observed (Figs. 14, 15). The decrease of aerosol concentration from the base of the layer to the sea surface is explained by the ability of the sea surface to easily trap aerosol particles (due to the particles' sedimentation and their capturing by wave crests and spray), and by the vertical profiles of temperature in the troposphere (the upwelling fluxes in the lower part of the dust layer). Of some interest is an unusual dependence of the

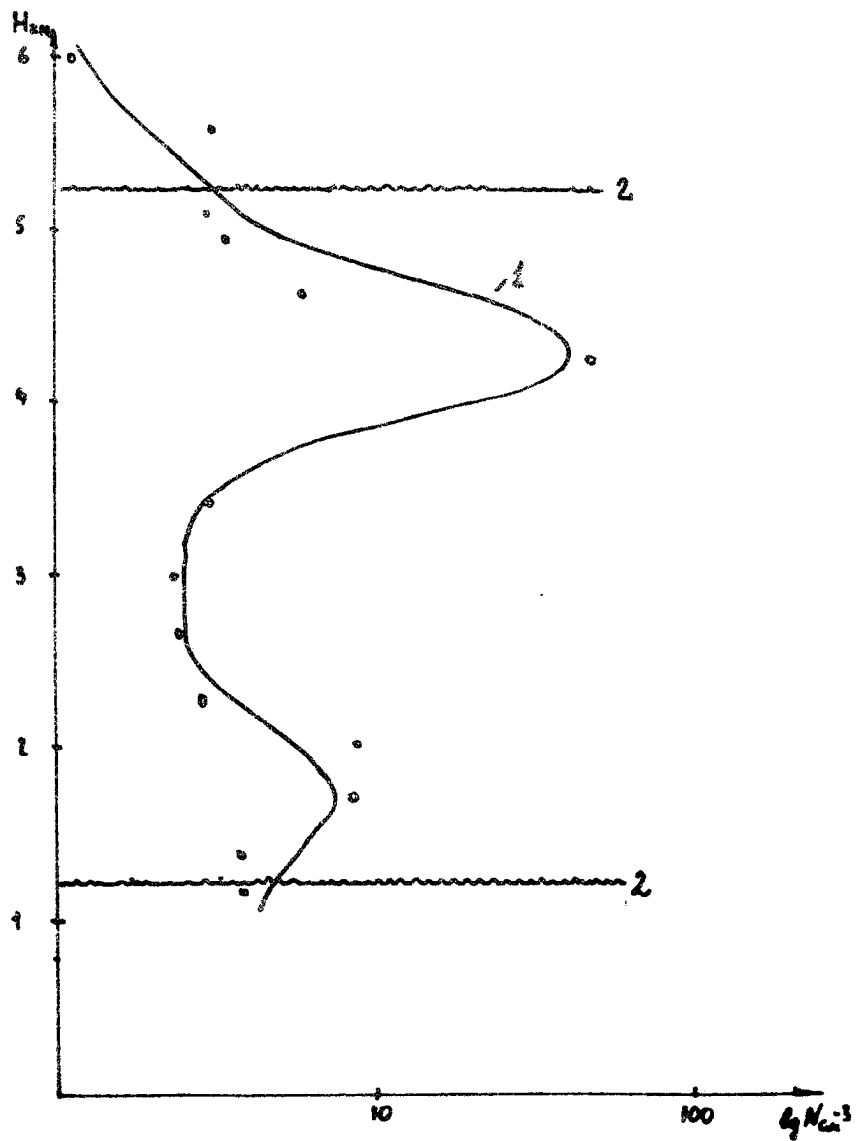


Fig. 14

The vertical profile of aerosol concentration of 4 July, 1974:
1 - calculating aerosol concentration
2 - aerosol layer boundaries

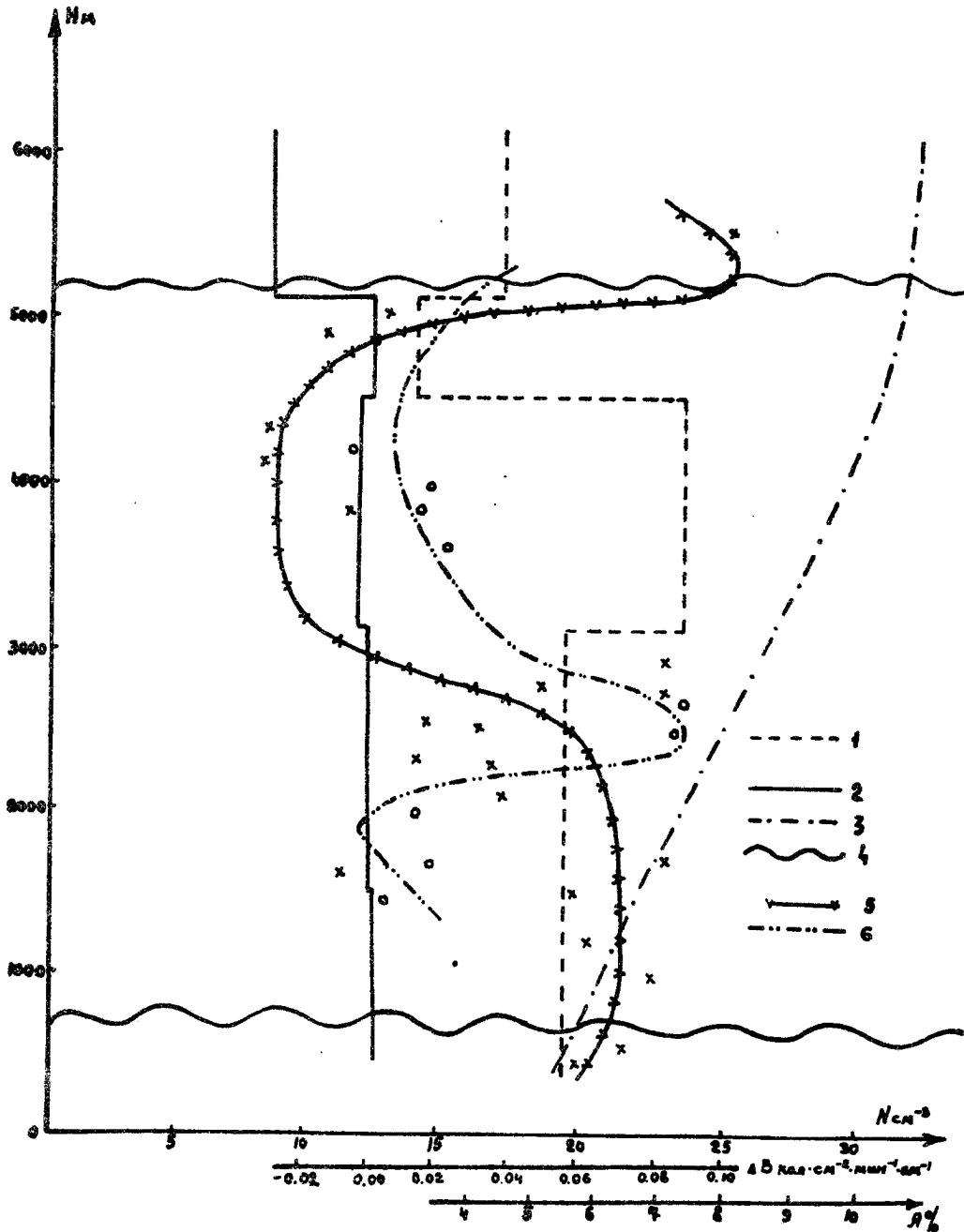


Fig. 15

The Complete Radiation Experiment:

- 1 - shortwave radiative heat flux divergence, ΔB_K
- 2 - longwave radiative heat flux divergence, ΔB_L
- 3 - albedo
- 4 - aerosol layer boundary
- 5 - profile of the calculating aerosol concentration (1130-1200)
- 6 - profile of the calculating aerosol concentration (1405-1435)

aerosol particle size spectrum on height: the aerosol fraction of rough dispersion in total particle content increases appreciably with height. This testifies to a comparatively recent generation of aerosol particles (several hours-days), a rather high speed of the upwelling fluxes (exceeding the speed of the gigantic aerosol particles fall: $W \geq 10$ cm/sec), and the significant role of coagulation in modifying the aerosol spectrum (apparently, the developed turbidity inside the dust cloud sharply increases the coagulation speed).

The microstructural investigations have shown the large particles to be mostly conglomerates of smaller ones. A good correspondence of aerosol numerical concentration with a minimum inside the dust cloud, to a maximum of the solar radiation absorption is of special interest. Since the radiation absorption is proportional to aerosol mass, one can suppose that either the imaginary part of the refraction index is small ($n_{i\lambda} < 0.01$) or the absorbing particles with high $n_{i\lambda}$ are inserted into larger particles.

A significant amount of particles with inhomogeneous structures is observed in the electronic microscope images, which testifies in favor of the second assumption. The plate crystals form rather a large portion of the particles. Apparently, they are not the salt particles brought from the continent. A considerable number of the particles are dark brown. Some filters were colored by these particles. They most probably consist of ferric oxides which noticeably absorb radiation in the visible.

The data of the chemical analysis for Fe content show this too. The Fe concentration in aircraft aerosol samples of the dust layer practically always exceeded 10 mkg/m^3 . The content of the metals is rather high (Table 4).

Table 4. Chemical analysis data for the aerosol particles sampled by the IL-18 aircraft in the dust cloud.

Date	Height meters	Elements, mkg/m ³						
		Fe	Cu	Cr	Pb	Mg	Al	Ca
12 July	300	12.0	0.4	0.03	0.2	14.9	25	30
13 August	450	-	-	-	-	-	-	-
4 September	450	14.0	3.0	0.15	0.2	7.0	9.0	-
4 September	450	20.0	-	0.04	0.2	-	4.0	-
12 July	1500	-	-	-	0.1	-	19.3	-
13 August	1500	-	-	-	-	6.0	5.0	-
13 August	1500	14.0	-	4.0	0.2	5.0	7.0	-
4 September	1500	14.0	3.0	0.15	0.2	7.0	9.0	-
12 July	3000	11.0	0.3	0.04	0.7	21.14	21.0	6.0
13 August	3000	14.0	-	4.0	0.2	5.0	7.0	-
4 September	3000	14.0	-	0.08	0.1	-	6.0	-
12 July	4500	-	-	0.04	-	10.2	12.0	-
4 September	4500	14.0	1.0	-	0.3	6.9	12.0	-
4 September	5200	14.0	-	0.04	3.4	-	-	-
4 September	6000	14.0	-	0.02	3.0	-	5.0	-
13 August	6080	-	3.0	-	-	-	-	-
14 August	6100	-	-	-	0.3	1.0	7.0	-
12 July	6400	-	0.1	0.02	-	4.0	20.0	-

Table 4a. Chemical analysis for aerosol particles sampled by the IL-18 aircraft in a dust-free atmosphere.

Date	Height meters	Elements, mkg/m^3						
		Fe	Ni	Cr	Pb	Mg	Al	Ca
31 August	450	-	-	-	-	-	6.0	-
31 August	900	-	-	-	-	2.0	-	-
30 August	3000	-	0.6	-	0.1	5.0	-	10.0
30 August	4500	5.0	-	0.1	0.1	4.0	-	6.5
31 August	6000	-	-	-	-	-	6.0	-
30 August	6100	12.0	0.6	0.2	0.1	-	-	4.0

Most of these elements are typical of continental dust but not of sea salts. The high content of Al exceeding $5-10 \text{ mkg/m}^3$ in some samples is striking. This fact should be compared in future with the possibility of aluminum containing compounds rising into the air.

The content of Ca is very unstable. However, judging by the data of the approximately simultaneous measurements, it varies but little. This fact indicates that the dust particles can be produced by different sources. The particles containing calcium are not large ($r \leq 10 \text{ }\mu\text{m}$), whereas the separate particles containing [Mg], [Al] are considerably larger: $r > 10-20 \text{ }\mu\text{m}$.

The morphological analysis of aerosol samples for the elements typical of sea salts, and for sulphate particles, shows that these compounds are not found in aerosols.

The analysis of the aerosol sampled by the "Professor Vize" shows that even in the near-water atmospheric layer a considerable portion of aerosol particles are not of marine origin. This is shown by a relatively high content of elements [Fe], [Ni], and [Ca] in the samples. However, the elements' ratio differs considerably for the samples taken on "Professor Vize" from that in the aircraft samples. Therefore, we can state that aerosol particles containing [Fe], [Al], [Pb] do not descend from the troposphere to the near-water layer in the region of the "Professor Vize".

The situation is quite different for the samples taken on "Passat". The content and the elements' ratio in the samples taken on the aircraft and on the "Passat" are very similar. One can suppose that in the region

of "Passat" the particles fall out of the dust cloud coming from the Sahara, which is explained by the existence of an air current that carries the dust cloud base southward towards the region of the "Passat".

5. VERTICAL PROFILES OF RADIATION FLUXES AND RADIATIVE HEAT FLUX DIVERGENCES.

The actinometric observations from the MGO IL-18 flying laboratory were made within the GATE-74 program with the help of radiation thermo-elements - pyranometers and pyrgeometers of the Leningrad Electro-Technical Institute (Kozyrev). The spectral regions of the sensitivity of these sensors are 0.3-3 and 3-30 μm , respectively. According to the manufacturers, the error in a single measurement is 5-6% for a pyranometer and 8-10% for a pyrgeometer.

Calibrations and comparisons with the reference ship actinometers carried out before the beginning of the experiment, as well as the inter-comparison flights with the other aircraft, participating in the experiment, have shown that all the sensors used maintain their sensitivities. For pyranometers, the deviations from the mean values of the observed fluxes during the intercomparison flights, were 1-3% for K_{\downarrow} and 4-8% for K_{\uparrow} and for pyrgeometers, 2-4% for L_{\downarrow} and up to 10% for L_{\uparrow} .

The comparisons revealed the systematic discrepancies between the data on the atmospheric counter-emission L_{\downarrow} obtained on the MGO IL-18 and the American NOAA C-130 and NCAR Sabreliner. Therefore, the data on the downwelling longwave fluxes are not discussed in this paper. The value of radiative heat flux divergence at the upper levels (5-6 km) could be underestimated by about 20% due to the possible errors in L_{\downarrow} values.

The accomplishment of the GATE Radiation Subprogram has made it possible to study, along with the other problems, the behavior of the radiation fluxes and heat flux divergences in the presence of dust-sand flows from the African continent (the so-called Saharan Aerosol Layer - SAL). From the point of view of analyzing these features, the results

of aircraft actinometric measurements in missions 7A and 7B (according to the GATE international classification [3]) are of special interest. These programs correspond in general to aircraft missions of the National Soviet program CENEX, accomplished with the use of the MGO IL-18 flying laboratory [36].

The actinometric data obtained from the MGO IL-18 flying laboratory on 4 July, 13 August, 14 August, and 4 September, 1974, are discussed below. These dates were chosen because they enable one to reveal the principal changes in the vertical profile of radiation fluxes and radiative heat flux divergences, occurring with the appearance of the dust layer, in comparison with the clean atmosphere. Measurements of 4 July and 4 September, 1974 were made in the presence of a distinctly expressed aerosol layer (SAL), and those of 13 and 14 August - in the absence of continental aerosol with the top of the haze being at about 5000 m.

It should also be mentioned that the haze was observed during all the measurements in the cloudless atmosphere. In that situation, even the visual observations from aboard the aircraft enabled one to simply classify the cases of SAL.

The continental aerosol is characterized by a reddish tint, its layer being quite dense with a clear upper boundary that can be determined with the accuracy of about 50 meters by the appearance or disappearance of the horizon during the ascent or descent of the aircraft.

From the observed data for the above mentioned dates, the curves of the short and long wave downwelling and upwelling radiation fluxes K_{\downarrow} , K_{\uparrow} , L_{\downarrow} , L_{\uparrow} temporal variations were drawn which made it possible to plot the immediate radiation profiles of the atmosphere for particular moments.

Such a technique is considered to be standard in the CENEX data processing and is described in detail in [36].

Figure 16 gives the vertical profiles of the downwelling short wave radiation fluxes K_{\downarrow} ($\text{cal cm}^{-2} \text{min}^{-1}$). The corresponding radiation profiles of the atmosphere are plotted for 4 July - 1330, 13 August - 1330, 14 August - 1420, and 4 September - 1300 GMT, i.e. approximately for conditions of the local noon, the case of 14 August excepted. The sun elevations were respectively: 4 July - 77.3° , 13 August - 86° , 14 August - 76.3° , and 14 September - 78° . As is seen from Fig. 16, the vertical profile of K_{\downarrow} sharply alters in the presence of aerosol layers. The profiles for 13 and 14 August indicate a considerable rise of the total radiation attenuation with a decrease of altitude.

On 4 July and 4 September [40] the strongest attenuation is observed at the top of aerosol layer. Because of this the downwelling radiation flux turns out to be considerably less on all the levels within the aerosol layer than in the absence of aerosol. So, on 4 July, at the altitude of 3100 m, the radiation flux is smaller by $0.15 \text{ cal/cm}^2 \text{ min}^{-1}$ as compared to the corresponding values of 13 August. It is also characteristic that at the expense of less intensive net radiation attenuation at the base of the aerosol layer, the values of fluxes at the lower measurement level are considerably closer. In some cases, a highly transparent layer is observed below 1.5 km as revealed, for example, by the data of 4 July and 13 August. The layer of aerosol or haze turns out to be elevated over the ocean surface, and its base corresponds to the level of the trade wind temperature inversion.

The analysis of the upwelling short wave fluxes profiles (Fig. 17) shows that in the presence of aerosol the upward radiation flux grows

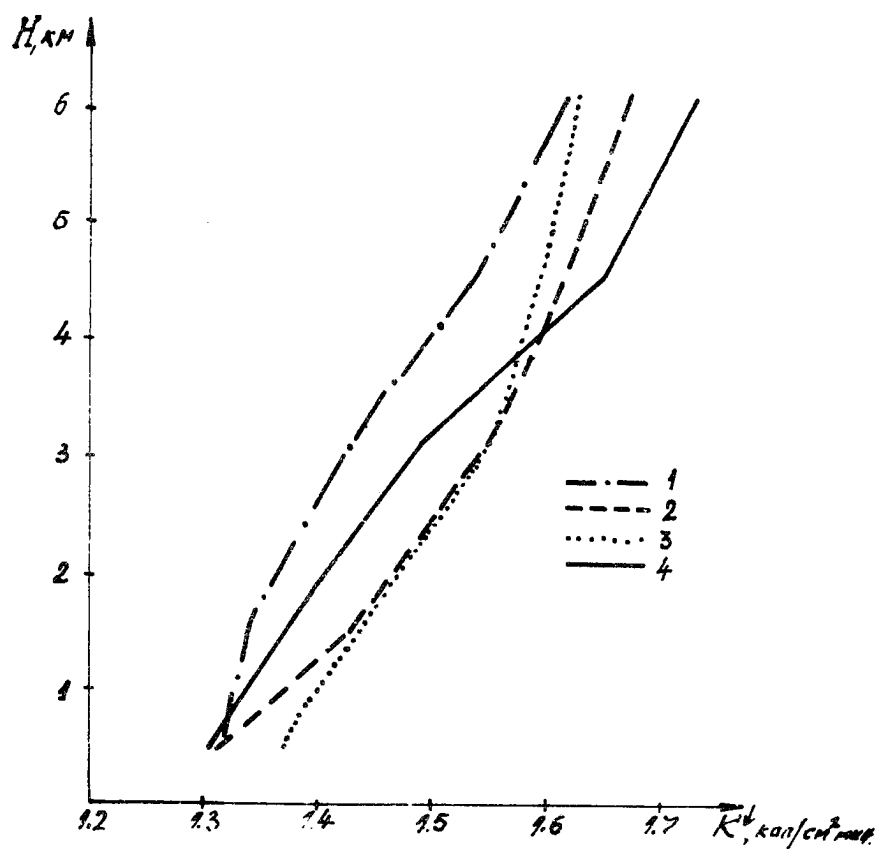


Fig. 16 Vertical profiles of the total radiation:
1 - 4 July, 1974, 1330 GMT;
2 - 13 August, 1974, 1350 GMT;
3 - 14 August, 1974, 1420 GMT;
4 - 4 September, 1974, 1300 GMT;

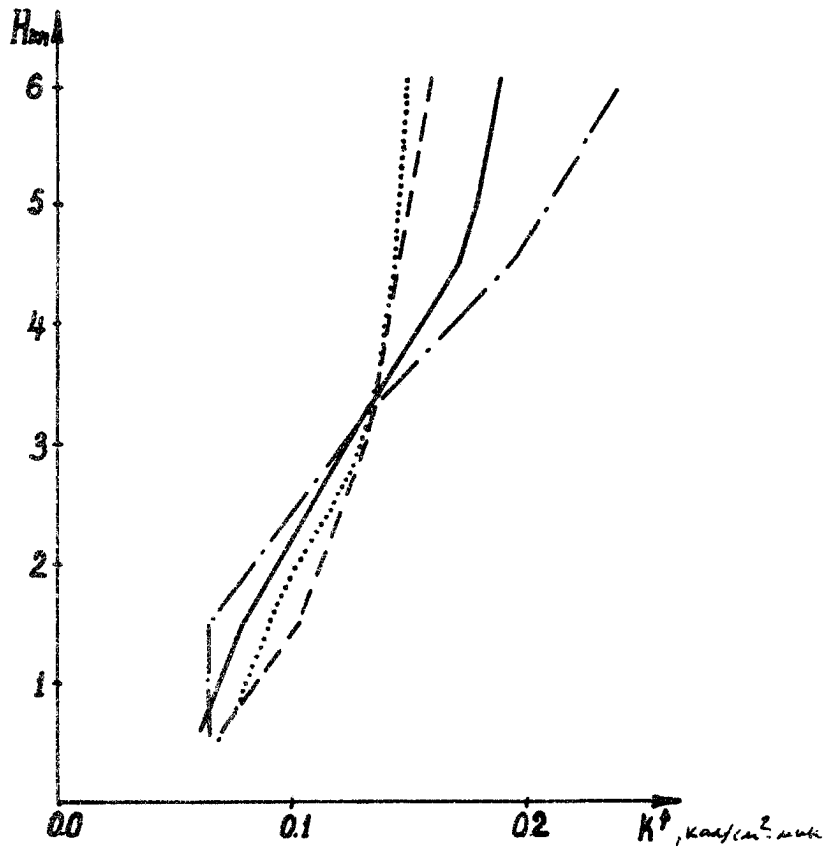


Fig. 17 Vertical profiles of the shortwave upwelling radiation fluxes. Notations, dates and measurement times are the same as in Fig. 16.

faster with altitude, this growth being practically uniform through the entire layer. In other words, while the net radiation attenuation due to aerosol is concentrated mainly in the upper part of the layer, all the levels contribute to the backscattered radiation. These variations are distinctly seen on the albedo vertical profiles (Fig. 18).

In the presence of an aerosol layer, the albedo increases with altitude more quickly, the rate of increase being practically stable up to the top of the layer. On 4 July, the albedo variations were especially great: from 5.9% at the base of the layer to 12.7% at the top [41]. In this case, a layer was observed below 1.5 km, where the albedo was practically constant and equal to the ocean surface albedo (about 5%), which again indicates the presence of an optically "empty" layer near the surface. It follows from Fig. 19 that on 13 August the scattering properties of the haze layer were analogous with the SAL. However, in this case, the radiation absorption is quite different, apparently due to peculiarities in the particle size distribution and chemical composition of the aerosol. Examination of the albedo vertical profile for 14 August enables one to state that on this day the layer of an optically active haze was concentrated between 3 and 0.5 km.

In the presence of aerosol the long wave radiation exhibits a sharper decrease of the upwelling radiation flux with altitude, which can be understood as masking of the surface by a cooler aerosol cloud. On 13 August and 4 September, the L_{\uparrow} fluxes differ by $0.12 \text{ cal/cm}^2 \text{ min}^{-1}$ at the altitude of 3 km.

The observations show that in the presence of aerosol, the downwelling long wave radiation flux has a greater decrease with altitude too.

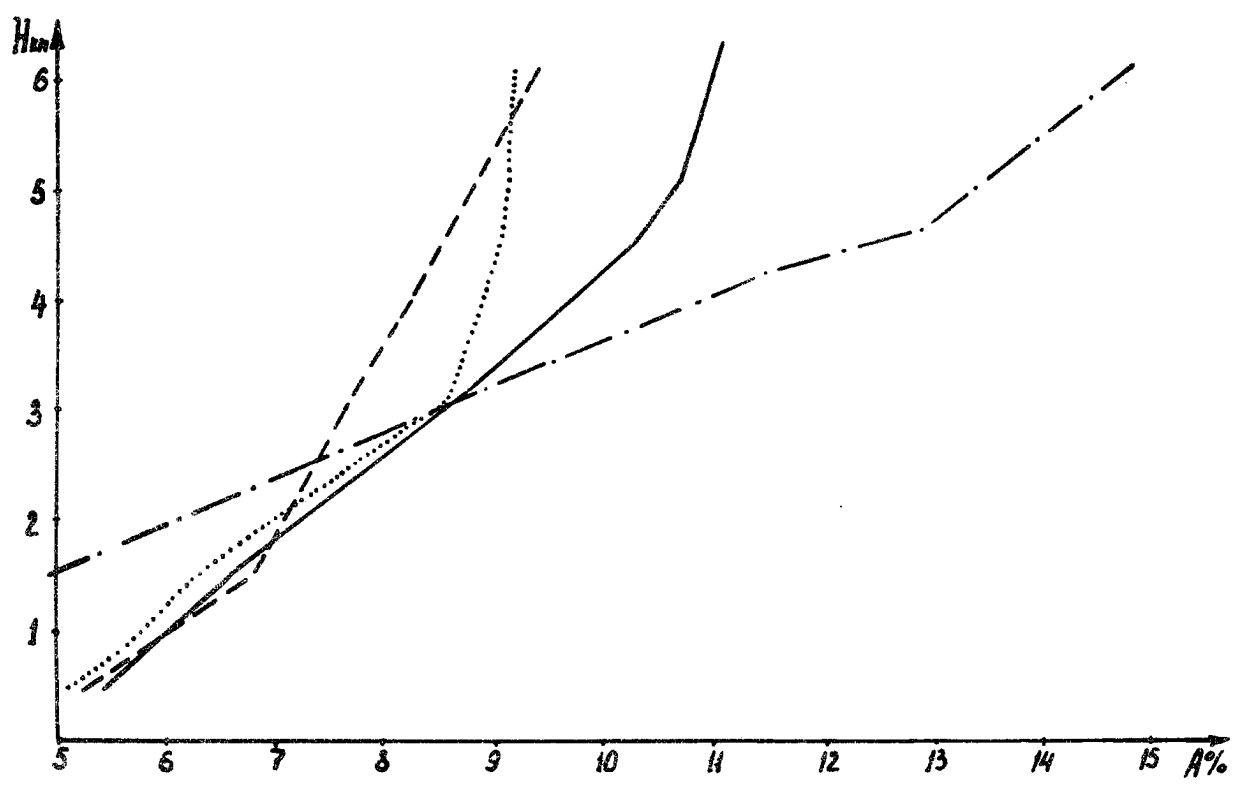


Fig. 18 Vertical profiles of albedo A. Notations, dates and measurement times are the same as in Fig. 16.

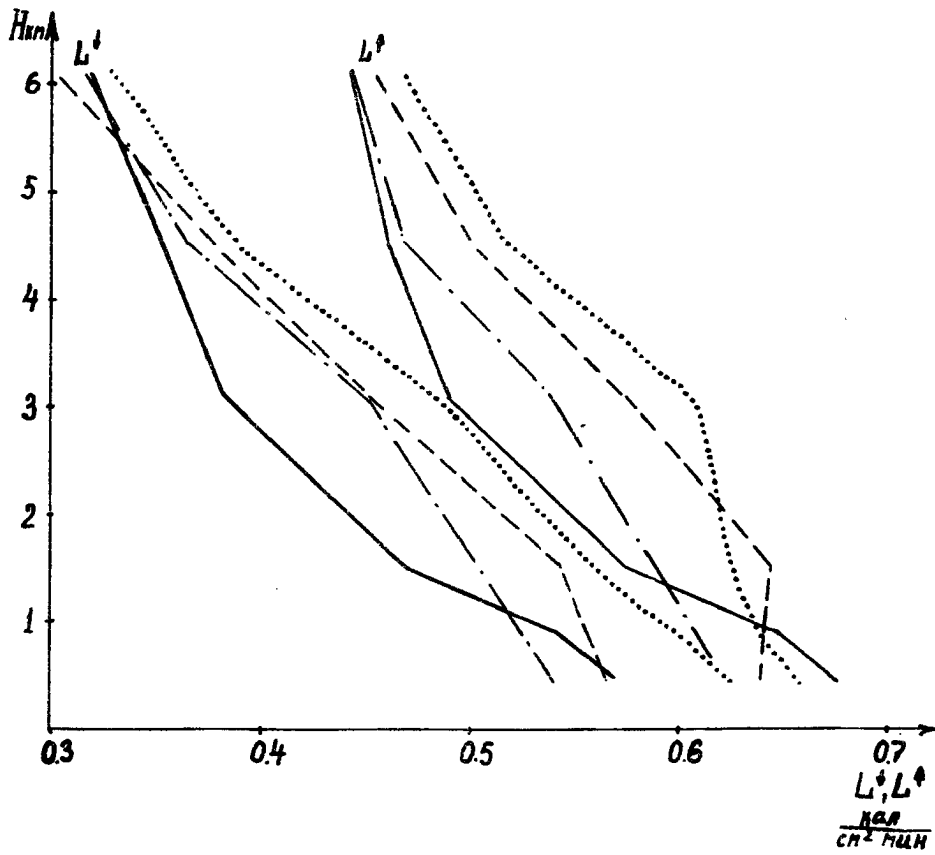


Fig. 19 Vertical profiles of the longwave downwelling L_{\downarrow} and upwelling L_{\uparrow} radiation fluxes. Notations, dates and measurement times as in Fig. 16.

For analyzing the characteristic features of radiative flux divergence ΔB vertical profiles, the most typical data for 13, 14 August and 4 September 1974 are presented in Fig. 20. As is seen, the most characteristic feature of the shortwave radiative heat flux divergence vertical profile in the presence of an aerosol layer (the right half of Fig. 20) is a maximum of absorption in the upper part of the layer. The analysis of the synchronous aerosol observation data shows that the appearance of this maximum can be explained by the fact that the most optically active particles are concentrated there (see Section 2) [42]. The heat flux divergence remains practically constant in the middle part of the layer and even decreases below 1.5 km in the optically less active zone below the base of the aerosol cloud.

In the absence of a dust outbreak, the vertical profile of the short wave radiation absorption turns out to be quite the opposite: the heat flux divergence increases with a decrease in altitude reaching a maximum at the lowest level.

The net radiative heat flux divergence is also greater in the presence of the aerosol: on 4 September, 1974, the heat flux divergence to a layer of 0.45 - 6.1 km was $0.31 \text{ cal/cm}^2 \text{ min}^{-1}$; on 13 August it reached $0.23 \text{ cal/cm}^2 \text{ min}^{-1}$ to the layer of 0.3-6.1 km, the additional (as compared to the clean atmosphere) absorption contained in the upper part of the aerosol layer. In the absence of a distinctly pronounced aerosol layer, the longwave radiation exchange leads to cooling on all the levels. However, in the middle troposphere the cooling is negligible, and only above the upper boundary of haze does it become comparable with the value of shortwave heating (Fig. 20). A maximum cooling is always associated with the top of the aerosol or haze layer. So, on 14 August, the maximum is contained in the 1.5 - 3 km layer (compare with the vertical profile of albedo).

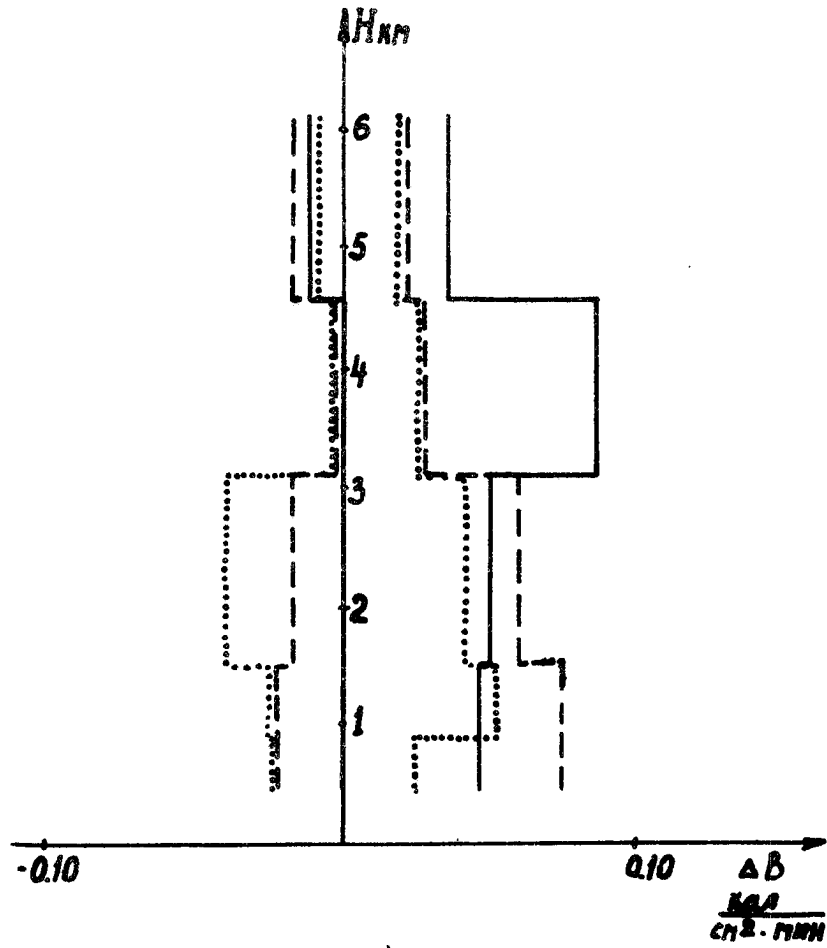


Fig. 20 Vertical profiles of radiative heat flux divergence. Notations, dates and measurement times as in Fig. 16.

The information obtained on 13 August and 4 September, 1974, makes an analysis possible within the framework of the complete radiation experiment realization. On these days, a complete radiation data set was obtained together with aerosol sampling, and meteorological parameters of the atmosphere. The observational conditions met the requirements for the complete radiation experiment in a cloudless atmosphere. The data on the content and chemical composition of the atmospheric aerosol (SAL) enable one to understand the nature of aerosol absorption [43].

The actinometric data show that the radiative properties of the aerosol layer have altered during the sampling process. The total short wave radiation absorption by the 450-6100 m layer at 1200 GMT reached $0.34 \text{ cal/cm}^2 \text{ min}^{-1}$. By 1500 GMT it decreased down to $0.23 \text{ cal/cm}^2 \text{ min}^{-1}$. The net long wave cooling for the same layer and the same time span amounted to $0.028 \text{ cal/cm}^2 \text{ min}^{-1}$ and $0.007 \text{ cal/cm}^2 \text{ min}^{-1}$, respectively. The radiation profile of the atmosphere plotted in Fig. 15 for 1300 GMT, presents the vertical distribution of radiation fluxes and heat flux divergences.

The analysis of the data obtained makes it possible to draw a conclusion that the change of radiative heat flux divergence and its vertical distribution with time are caused by variations of the aerosol's radiative properties. Observations show that the small and most optically active particles ($r \approx 0.2-0.3 \text{ }\mu\text{m}$) were concentrated in the upper part of the layer, and their concentration is significantly higher in the case of the first sounding. This explains a high absorption in the first case. The available data on the particles' chemical composition and (aerosol) size distribution will make it possible to construct a model of the

complex index of particle refraction and to theoretically calculate aerosol absorption. In connection with this, the analysis of data on the shortwave spectral fluxes in a free atmosphere is of great importance.

6. SPECTRAL DISTRIBUTION OF THE SHORTWAVE RADIATION FLUXES AND RADIATIVE HEAT FLUX DIVERGENCES.

Two spectrometers (K-2 and SPI-74) on board the IL-18 aircraft enabled one to measure radiation fluxes over the regions of 0.4 - 0.95 μm (K-2), and 0.4 - 2.5 μm (SPI-74). The overlapping of the instruments' spectral ranges enable one to accomplish reciprocal accuracy control of the results obtained and to reduce the SPI-74 readings (which has not been calibrated in absolute units) to the absolute scale.

Let us begin with the K-2 spectrometer data regarding mainly the visible part of the spectrum.

6.1 Visible Part of the Spectrum

The measurements made with the help of two identical short wave K-2 spectrometers, provided the spectral downwelling and upwelling radiation fluxes, which made it possible to further calculate the spectral net radiation, spectral albedo and spectral radiative flux divergence. The spectral resolution was about 0.002 μm , the angle of vision 180° , time of scanning over the entire operational wavelength region was about 10 sec. The measurements were taken at different levels in the free atmosphere during the horizontal flight, and as a rule, in the "fast" descent regime [19].

6.1.1 Spectral Fluxes and Balances in a Cloudless Atmosphere and in the Presence of a Stratocumulus Cloud Layer.

Figure 21 (a, b, d, e) shows the spectral downwelling $K_{\downarrow\lambda}$ and upwelling, $K_{\uparrow\lambda}$ radiation fluxes at various levels in the atmosphere, measured on 4 September, 1974, and 13 August, 1974, in the cloudless atmosphere. In the visible, the curves are smoothed down. As is seen from the figure, the absolute values of spectral fluxes depend

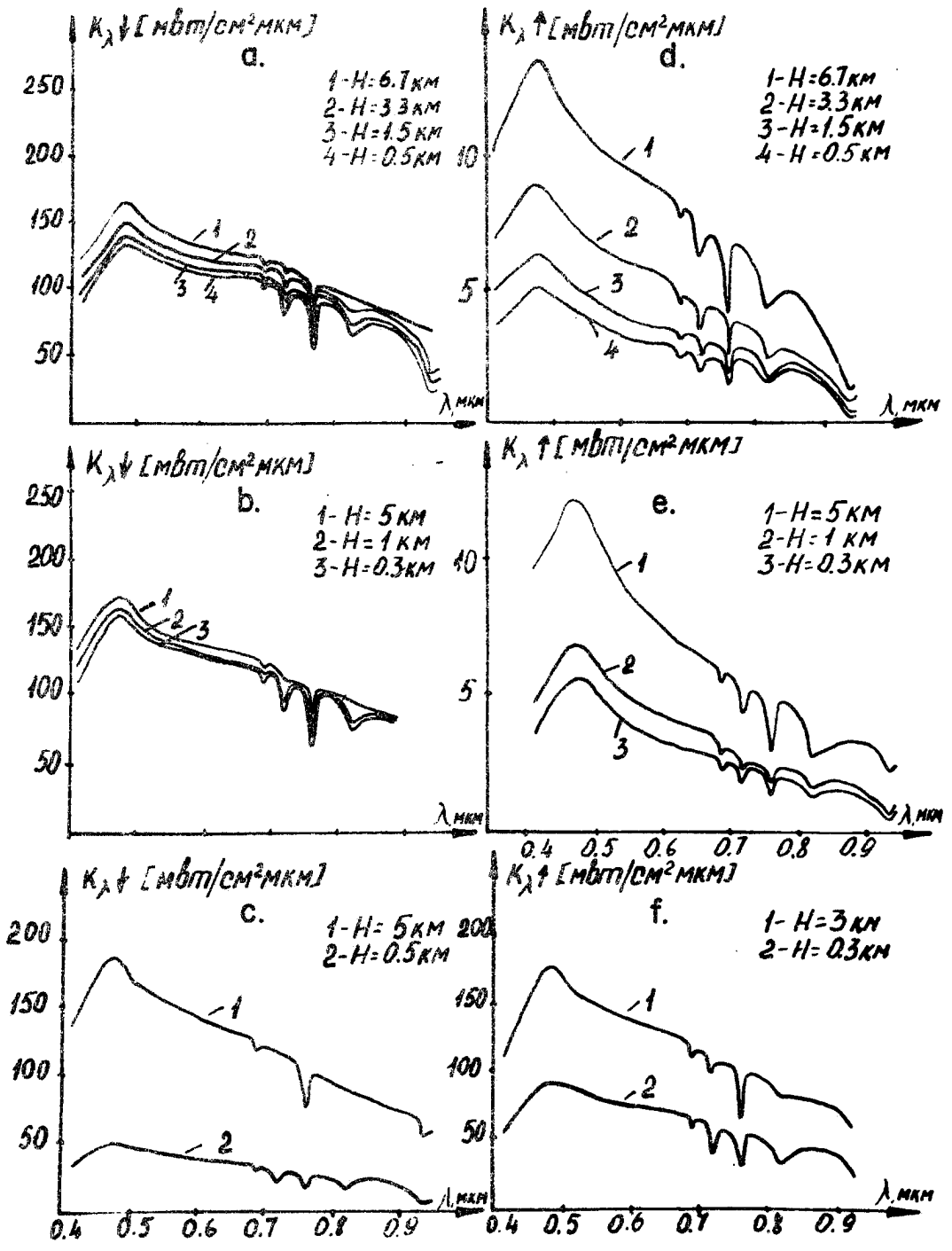


Fig. 21 Spectral downwelling K_{λ}^{\downarrow} and upwelling K_{λ}^{\uparrow} radiation fluxes at different atmospheric levels:
 a, d - 4 September, 1974 | cloudless atmosphere
 b, e - 13 August, 1974 |
 c - 4 August, 1974 | cloudy atmosphere, (Sc, 10 points)
 f - 12 July, 1974 |

significantly on altitude. In the continuous spectrum, the fluxes decrease with decrease of flight level, the flux vs. height derivative varying from day to day due to peculiarities of the atmosphere stratification in the GATE area.

According to the CENEX data [20], a monotonous decrease of aerosol concentration with altitude and, hence, the monotonous vertical profiles of radiation fluxes were always observed.

Under a "two-layer" structure of the tropical atmosphere, the radiation fluxes variation with altitude is not monotonous. The fluxes are greatly attenuated in the upper part of the sounded atmospheric layer, where the dust aerosol is contained, and remain practically constant through the lower "clean" layer.

The dependence of $K_{\downarrow\lambda}$ and $K_{\uparrow\lambda}$ on altitude differs in the molecular absorption bands, i.e. the bands deepen with decreasing height in the downwelling fluxes spectra, but the relative band depth decreases for the upwelling fluxes spectra. These regularities particularly show themselves through in the water vapor absorption bands. In Fig. 21 (c, f) represent data from observations made on 12 July(f) and 4 August (c), 1974, namely the spectral fluxes $K_{\downarrow\lambda}$ and $K_{\uparrow\lambda}$ at two levels for the atmosphere containing a 10-point layer of stratocumulus (Sc) cloudiness.

In the first case, the exact data on the cloud thickness ΔH , the top height, H_t , and the base height, H_b , are absent, and in the second case, $\Delta H = 0.4$ km ($H_t = 1.3$ km, $H_b = 0.9$ km). The upper curves were obtained for the levels of $H = 3.3$ km (12 July 1974) and $H \approx 5$ km (4 August 1974), the lower curves [46] - below cloudiness. The radiation fluxes were measured also immediately above the cloud layer, however, since the

the stratocumulus cloudiness was horizontally inhomogeneous, the interpretation of the spectra turned out to be impossible due to the scarcity of the excerpts obtained.

Figure 22 (a, b) depicts the curves of the spectral net radiation ($B_\lambda = K\downarrow_\lambda - K\uparrow_\lambda$) at different levels according to the data obtained in the cloudless (a) and cloudy (b) atmosphere. As long as reflection by the ocean surface has no outstanding spectral features, the B_λ spectral curve follows the energy distribution in the downwelling fluxes. The variations of the absolute value of B_λ with altitude differ depending on optical conditions. In the case of the cloudless atmosphere (Fig. 22a), the decrease is most remarkable for the upper levels of the sounded atmospheric layer. In the lower layer, the B_λ value changes but little with altitude. In the cloudy atmosphere, the value of net radiation changes significantly with passing through a cloud layer (Fig. 22b).

6.1.2 The Albedo Transformation of the System "Ocean Surface - Atmosphere".

Figure 23 (a, c) shows the curves of the "ocean surface - atmosphere" system spectral albedo obtained on 4 September, 1974 (turbid atmosphere) (a), and 13 September, 1974 (relatively clean atmosphere) (c). The ocean surface spectral albedo (lower curves) is smooth and decreases towards the red part of the spectrum from 3-4% near $\lambda = 0.4 \mu\text{m}$ down to 2-3% near $\lambda = 0.8 \mu\text{m}$. Of the distinct spectral peculiarities (associated for example, with the presence of plankton, etc.) none are observed. With the increasing altitude, the spectral albedo also increases from 2-4% near the surface up to 8-10% at the altitude of about 6 km and shows substantial variation as a function of wavelength.

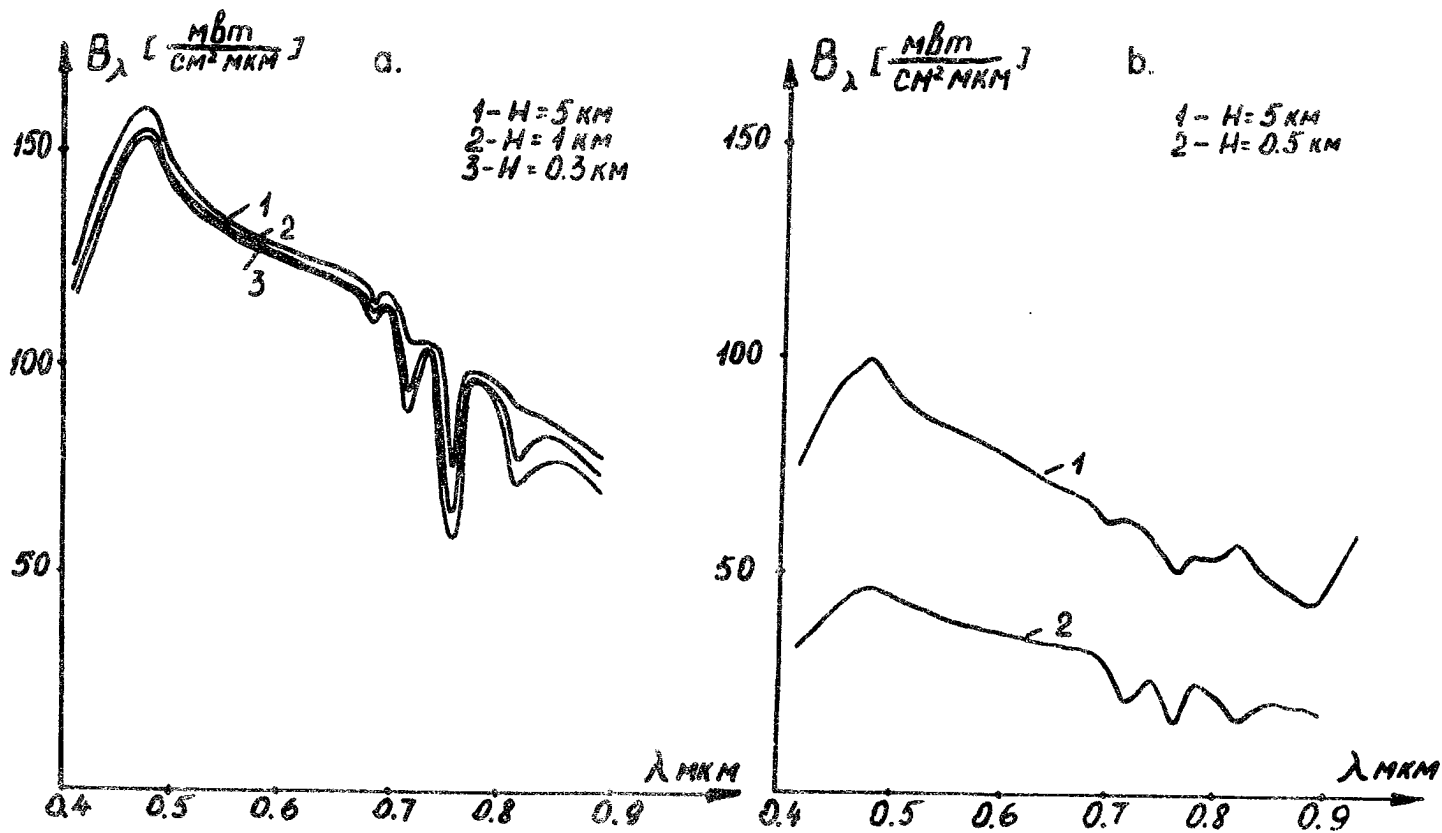


Fig. 22

Spectral net radiation B_λ at different atmospheric levels:
 a - 13 August, 1974, cloudless atmosphere;
 b - 4 August, 1974, cloudy atmosphere (Sc, 10 points)

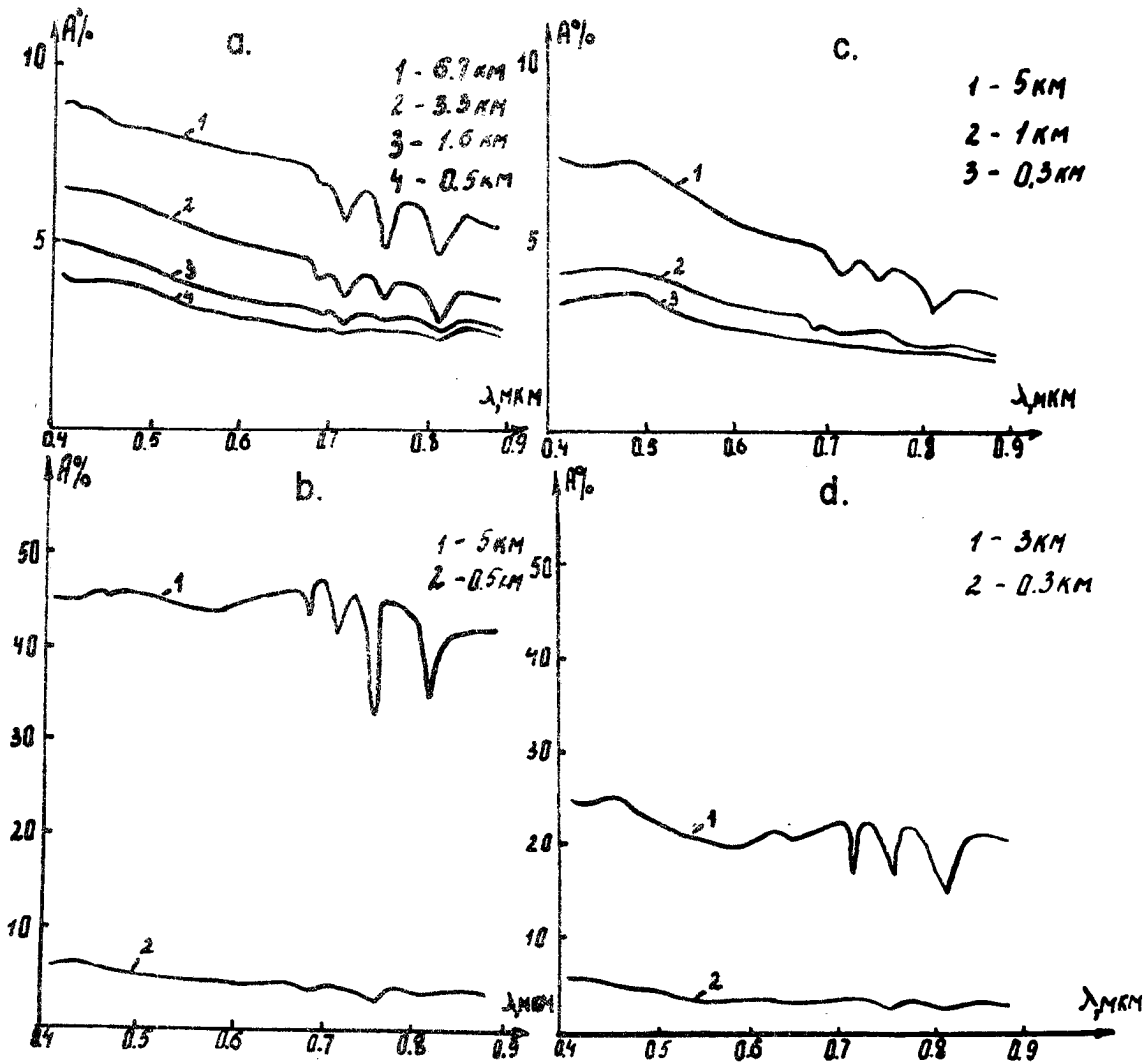


Fig. 23 Spectral albedo of the "ocean surface-atmosphere" system:
a - 4 September, 1974, clear weather;
b - 4 August, 1974, Sc, 10 points;
c - 13 August, 1974, clear weather;
d - 12 July, 1974, Sc, 10 points.

In the lower "clean" layer the A_λ increase with height is stronger with the shortening wavelength, which is caused by molecular scattering. In the dust layer, the albedo increases faster in the longwave part of the spectrum, and the more the dust layer thickens and the dust particles' concentration increases, the higher is the albedo increase. This albedo change is conditioned by the interaction of light with aerosol particles, selectively absorbing in the short wave spectrum region. These conclusions are well illustrated by the data of Table 5, where the "blue-red" ratios $A' = \frac{A_\lambda = 0.42 \mu\text{m}}{A_\lambda = 0.8 \mu\text{m}}$ are given for the dates and levels under consideration.

Table 5. "Blue-red" ratios for albedo.

13 August		4 September	
H, km	A'	H, km	A'
5	1.85	6.3	1.45
1	2	3.3	1.7
0.5	1.8	1.5	1.75
		0.5	1.55

Figure 23 (b, d) shows the measurement data on spectral albedo obtained on 12 July, 1974 (d) and 4 August (b) in the cloudy atmosphere. The water surface spectral albedo below the clouds (lower curves) is somewhat higher as compared to the case of cloudless atmosphere due to the diffuse character of the incident radiation, while the spectral curve remains the same. The spectral albedo of thin, translucent stratocumulus cloudiness obtained on 12 July, 1974 at the altitude of 3.3 km is 20-25%.

The albedo value increases towards the blue part of the spectrum (apparently due to the effect of dark ocean surface). In the case of a more dense Sc cloudiness ($H = 0.4$ km, 4 August, 1974, Fig. 23b) the spectral albedo is 45% and does not vary over the spectrum.

In cases of both cloudless and cloudy atmospheres, the spectral albedo curves have minima in the atmospheric gases' absorption bands, their depth increasing with altitude.

6.1.3 The Spectral Radiative Heat Flux Divergences in the Cloudless and Cloudy Atmosphere

The values of the spectral downwelling and upwelling radiation fluxes obtained at different levels ($K_{\lambda, H_i}^{\downarrow}, K_{\lambda, H_i}^{\uparrow}$) were used to calculate the spectral radiative heat flux divergences in the atmospheric layers of $\Delta H_{i, j} = H_j - H_i$. The spectral radiative heat flux divergence, $\zeta_{\lambda, \Delta H_{i, j}}$, in the atmospheric layer $\Delta H_{i, j}$ is equal to the difference between the spectral balances at the layer boundaries $\zeta_{\lambda, \Delta H_{i, j}} = B_{\lambda, H_j} - B_{\lambda, H_i}$, note this is an approximation of the horizontal optical homogeneity of the atmosphere.

In order to more clearly reveal the spectral peculiarities of radiation absorption by the atmosphere, it is necessary to take into account the characteristic features of the source spectrum (in our case - net radiation). For this purpose, the relative radiative heat flux divergence or the atmospheric absorption spectral function was calculated according to the formula:

$$\beta_{\lambda, H_2 - H_1} = \frac{\zeta_{\lambda, \Delta H_{1, 2}}}{K_{\lambda, H_2}^{\downarrow}} \cdot 100\%$$

where $K_{\lambda, H_2}^{\downarrow}$ is the downwelling spectral flux at the upper boundary of the layer under consideration.

Figure 24 represents the values of $\zeta_{\lambda, \Delta H_{i, j}}$ and $\beta_{\lambda, \Delta H_{i, j}}$ obtained in the cloudless atmosphere with great and small dust content (Figs. 24a, c and 24b, d, respectively). As is seen from Fig. 24c, a considerable selective absorption is observed over the entire region of the spectrum under consideration. The radiative heat flux divergence in the 0.4-0.6 mkm interval is produced by aerosol absorption alone. Sharp maxima are observed in the molecular absorption bands centered at 0.62 mkm (O_2, O_3, H_2O), 0.69 mkm (O_2), 0.72 mkm (H_2O), 0.76 mkm (O_2), 0.82 mkm (H_2O), and 0.93 mkm (H_2O). The spectral tendency of aerosol absorption follows qualitatively the spectral dependence of an imaginary particle, $n_{i\lambda}$ of haematite (mainly, Fe_2O_3) that has a maximum refraction index at $\lambda = 0.41 - 0.42$ mkm (the dashed curve in Fig. 24c). Identification of the observed aerosol absorption as absorption by haematite is verified by the analysis of the aerosol samples' chemical composition, which shows a great percentage of ferric oxides, and by the similarity of β_{λ} spectral trace for GATE and for the CENEX expedition, accomplished earlier in the region of the Kara Kum desert [21].

The value of aerosol absorption depends substantially on the density of the sandy haze which can be clearly seen from comparing the curves 1 in Fig. 24, which characterize the values of ζ_{λ} and β_{λ} for the entire sounded atmospheric layer. In case of a dense haze on 4 September, 1974 (Fig. 24c), the maximum relative aerosol absorption reaches 20% for the 6.3 - 0.5 km layer. For the thin haze on 13 August, 1974 (Fig. 24d), the value of β_{λ} is 5-7%.

By comparing the curves of Fig. 24a, b characterizing the spectral influxes to the atmospheric layers of different thickness, the main features of the aerosol absorption vertical distribution can be readily

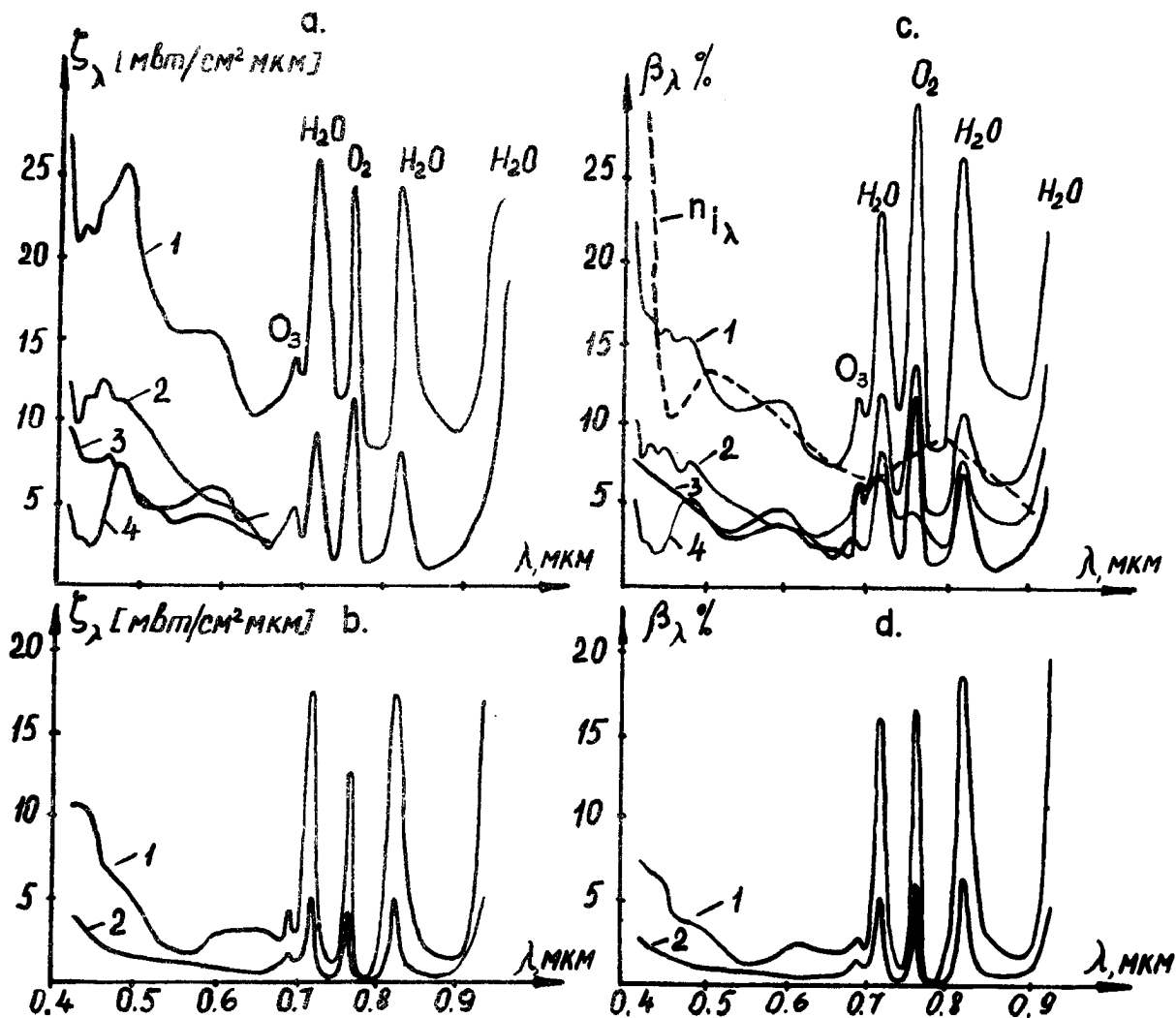


Fig. 24 Spectral absolute ξ_λ and relative β_λ radiative heat flux divergence in the atmospheric layers of various thicknesses:
 a) 4 September, 1974, ξ_λ ;
 c) 4 September, 1974, β_λ ;
 1 - $\Delta H = 6.7-0.5$ km;
 2 - $\Delta H = 6.7-3.3$ km;
 3 - $\Delta H = 3.3-1.6$ km;
 4 - $\Delta H = 1.6-0.5$ km;
 b) 13 August, 1974, ξ_λ ;
 d) 13 August, 1974, β_λ ;
 1 - $\Delta H = 5-0.3$ km;
 2 - $\Delta H = 1-0.3$ km;

revealed: 1) steep changes of the absorption absolute value due to stratified vertical distribution of the absorbing aerosol component; 2) maximum absorption at a certain altitude in the atmosphere.

In the dust-free lower layer, the top of which in the cases considered varied from 0.5 km (4 September, 1974) to 1 km (13 August, 1974), only molecular absorption and scattering were observed. Apparently, the marine aerosol (if present) absorbs radiation very poorly.

In Fig. 25, curve 1 characterizes the spectral distribution of the absolute radiative heat flux divergence, ε_λ , for the entire sounded atmospheric layer, and curve 2 is obtained by multiplying the coordinates of the relative spectral heat flux divergence, β_λ , (curve 1, Fig. 24c, d) approximated by the dependence of λ^{-1} , by the ordinates of continuous spectral distribution of energy for the incident radiation at the upper boundary of the layer. Curve 2 describes the spectral course of the averaged absolute aerosol radiative heat flux divergence in the atmospheric layer. The area under curve 2 characterizes the complete radiation absorption due to aerosol, the area between curves 1 and 2 determines the complete absorption due to the gaseous components of the atmosphere. In case of a heavily turbid atmosphere (4 September, 1974), the absorption due to aerosol is $0.045 \pm 0.01 \text{ cal/cm}^2 \text{ min}^{-1}$ (about 3.3% of the solar constant), and the molecular absorption is $0.015 \pm 0.005 \text{ cal/cm}^2 \text{ min}^{-1}$ (about 1% of the solar constant).

In a weakly turbid atmosphere on 13 August, 1974, the absorption due to aerosol was $0.0085 \pm 0.002 \text{ cal/cm}^2 \text{ min}^{-1}$ (approximately 0.6% of the solar constant), and the molecular absorption was $0.015 \pm 0.005 \text{ cal/cm}^2 \text{ min}^{-1}$ (about 1% of the solar constant). The results given above refer to the 0.4-0.95 μm spectral region.

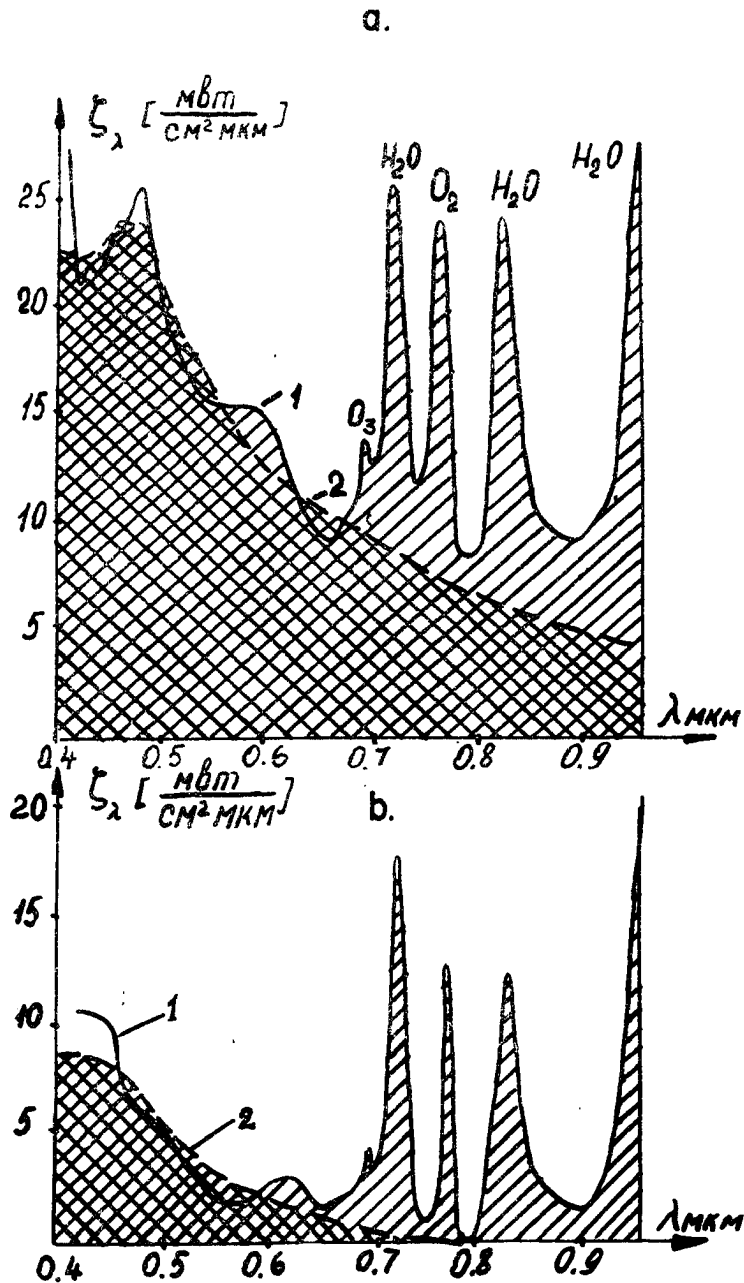


Fig. 25 Absolute aerosol radiative heat flux divergence (double dashing) and molecular radiative heat flux divergence (single dashing) for the whole atmospheric layer sounded:
a - 4 September, 1974;
b - 13 August, 1974;
1 - spectral absolute radiative heat flux divergence;
2 - spectral averaged absolute radiative heat flux divergence at the expense of absorption by aerosol.

Bearing in mind that the principle input to molecular absorption in the shortwave part of the spectrum is provided by the 1-2.5 mkm range, where the intensive water vapor and carbon dioxide absorption bands are located, one can assume that aerosol and molecular absorptions are comparable for a heavily turbid atmosphere, while in the weakly turbid atmosphere the molecular absorption by the atmospheric gases contributes mainly to the radiative heat flux divergence.

Figure 26 gives the spectral curves of the absolute τ_λ and relative β_λ radiative heat flux divergences in the atmospheric column containing a 10-point layer of stratocumulus cloudiness of varying thickness (in the "a", "c" cases the thickness of the layer is $\Delta H = 0.4$ km). The relative radiative heat flux divergence values vary from 25% up to 30% for different days considered. The β_λ spectrum is relatively neutral in the visible. Only sharp maxima in the molecular absorption regions are observed.

6.2 The Near-IR Spectrum Region.

The MGO IL-18 flying laboratory operating within the GATE program was equipped with the SPI-74 two channel prism-spectrometer to obtain data on radiative fluxes and heat flux divergences, transparency and albedo, on brightness indicatrices, as well as data on transformation of these values in the atmosphere over the 0.4-2.5 mkm spectrum region. The measurements made with the help of the SPI-74 spectrometer, mutually supplement the data of the K-2 spectrometers, the indicatometer, the albedometer and pyranometers. By the start of the IL-18 operations in Dakar, the spectrometer was reassembled, automatics, control and display systems were modified, the speed of the spectrum scanning was increased, however, its principal scheme and basic technical characteristics remained unchanged

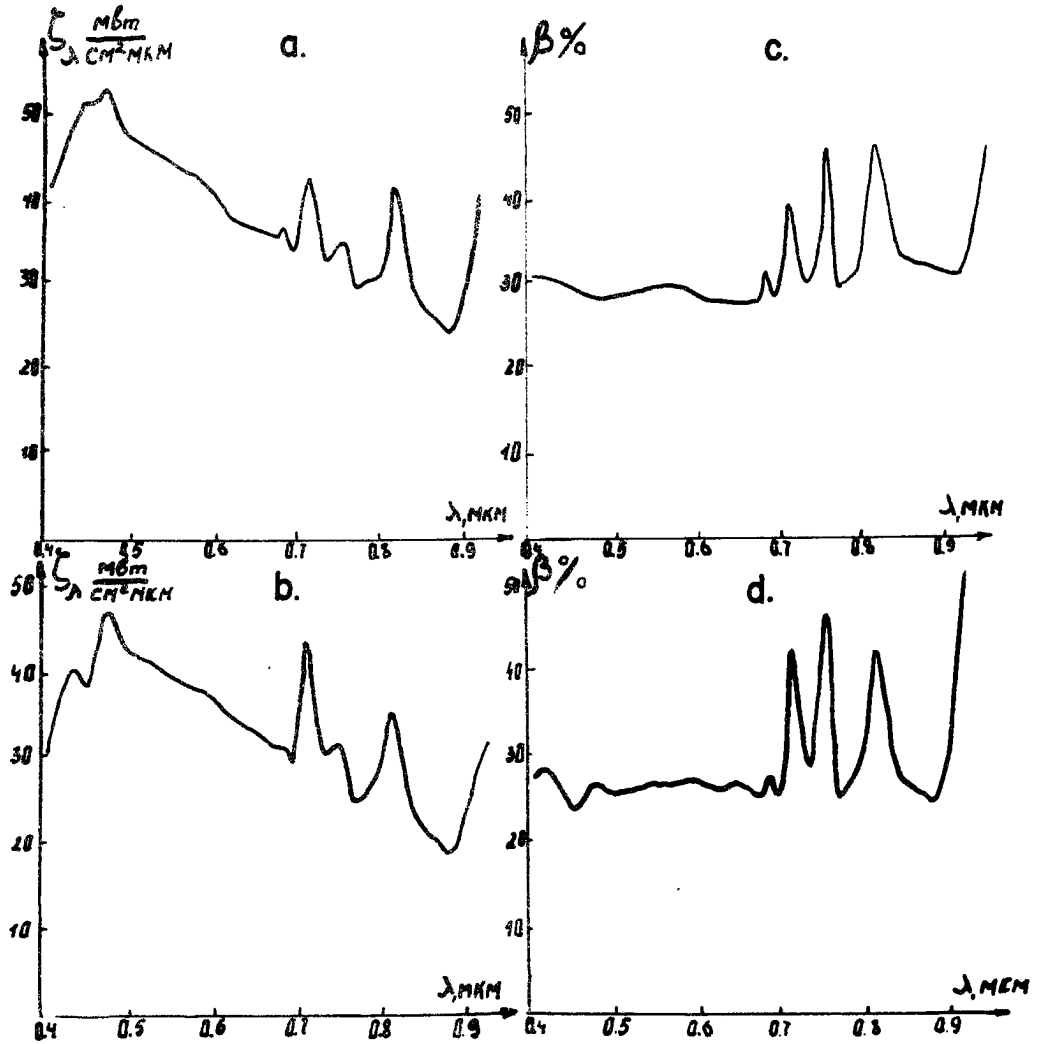


Fig. 26

Spectral radiative heat flux divergence in the atmosphere with a continuous Sc layer:
a, b - absolute radiative heat flux divergence ϵ_λ as of 4 August, 1974, and 12 July, 1974, respectively.
c, d - relative radiative heat flux divergence as of 4 August and 12 July, 1974, respectively (β_λ).

[21, 22], excepting an insignificant decrease of the spectral resolution. The measurement techniques by the SPI-74 spectrometer were those worked out for the CENEC program [21].

In this case, the specific conditions of operating in the tropics, with certain navigational limitations due to the simultaneous work of several aircraft in the zone, were taken into account. These measurements were characterized by the fact that the number of the azimuth profiles for measuring the brightness indicatrices did not exceed 2, and the azimuths were established irrespective to the sun. The latter hampers the processing and interpreting of the data obtained. At the given azimuths, the sky and the "ocean-atmosphere" system brightness were measured in 10-15 directions from nadir to zenith in the vertical plane. Also, the brightness of a reference plate illuminated by the sun was regularly registered at all the altitudes.

When processing the data, the downwelling radiative fluxes were calculated through the reference plate brightness corrected for illumination by the radiation scattered from that part of the sky which is screened from the reference plate by the elements of the instrument and the aircraft hull:

$$K_{\downarrow\lambda} = \varepsilon_{\lambda} \pi \left[\frac{y_{\lambda}^{\rightarrow}}{z_{\lambda}^{\rightarrow}} + a \sum_{n=1}^4 y_{\lambda}(i_n) \cdot S_{OTH}(i_n) \right] \quad (1)$$

where ε_{λ} is the instrument spectral sensitivity; $y_{\lambda}^{\rightarrow}$ and $y_{\lambda}(i_n)$ are signal amplitudes by the instrument, proportional to the brightnesses of reference plate and the sky in the i_n direction; $z_{\lambda}^{\rightarrow}$ is a spectral brightness coefficient for the reference plate; i is the zenith viewing angle; a is a portion of sky screened at a given azimuth; $S_{OTH}(i_n)$ is a relative area cut out from the spherical surface by two circumferences parallel

to the horizon and drawn at the angular distances of half-a-step between the measurements at succeeding zenith angles from zenith:

$$S_{OTH}(i_n) \cong 2(\cos \frac{i_{n-1} + i_n}{2} - \cos \frac{i_n + i_{n+1}}{2}) \cos i \quad (2)$$

The measurements were taken at zenith angles $i=0, 15, 30, 45, 70$ and 90° , and $i_n=15, 30, 45, \text{ and } 70^\circ$.

The upwelling radiative fluxes $K\uparrow_\lambda$ were calculated through the brightnesses measured at nadir angles $\theta = 0, 20, 40, 60$ and 90° , assuming that the brightness is independent of azimuth within the lower hemisphere:

$$K\uparrow_\lambda = \pi \epsilon_\lambda \sum_{n=1}^5 S_{OTH}(\theta_n) \cdot y_\lambda(\theta_n) \quad (3)$$

The value of $S_{OTH}(\theta_n)$ is calculated in the same way as $S_{OTH}(i)$. Under typical conditions, at high sun elevations, the assumption of the brightness indicatrix independence on azimuth is quite acceptable. So the error in determining the upwelling flux through such techniques does not exceed 15% according to evaluations made by V.I. Korzov. Considering the dominating contribution of the downwelling fluxes to the radiative balance, this error is insignificant for the sea measurements.

Below, the results will be given of calculating the relative spectral radiative characteristics of the atmosphere and the underlying surface: attenuation coefficients for the downwelling fluxes $T_\lambda|_z^{z \max}$, albedo $A_\lambda(z)$ and the relative radiative heat flux divergences $\beta'_\lambda|_z^{z \min}$ calculated by the formulae:

$$T_\lambda|_z^{z \max} = K\uparrow_\lambda(z) / K\uparrow_\lambda(z \max), \quad (4)$$

$$A_\lambda(z) = K\uparrow_\lambda(z) / K\uparrow_\lambda(z), \quad (5)$$

$$\beta'_\lambda|_z^{z \min} = [B_\lambda(z) - B_\lambda(z \min)] / K\uparrow_\lambda(z \max), \quad (6)$$

where $B_\lambda(z)$ are radiative balances;

$$B_\lambda(z) = K\uparrow_\lambda(z) - K\downarrow_\lambda(z).$$

In calculating, the relative values of radiation fluxes were used, i.e. formulae (1) and (3) were used without the factors of ϵ and π .

It should be mentioned that the error in determining the radiative heat flux divergences by formula (6) with the use of the SPI-74 data reaches 15-40% for different spectral regions. In all cases, the reduction of data obtained during a single sounding to one moment in time was accomplished proportionally to the variation of the sine of the sun elevation.

Up to the present time, 8 soundings have been processed for 6 days: 4 July, 12 July, 10 August, 31 August (two soundings), 4 September, (two soundings), and 29 September. According to visual assessment, the most transparent atmosphere was observed on 31 August. On 12 July, a dust layer was located over thin 9-10 point stratocumulus cloudiness. On 4 July, 4 September and 22 September, the flights were carried out in the turbid atmosphere. On 10 August, the unique measurements extra-program was accomplished in the dust storm. From the scientific-research ship "Musson" and meteorological satellite data, this latter was the south-western branch of a dust outbreak from the African continent.

Below, only those results of processing the SPI-74 data will be presented in detail, for the days on which all the available K-2 spectrometer data have already been processed.

Figure 27 gives the relative spectral influxes of radiative energy and albedo calculated for 1200, 4 September, and Fig. 28 gives the analogous data for 1350, i.e. the interval between soundings being almost 2 hours. It follows from comparison of Figs. 27 and 28 that during this time period, the radiative heat flux divergences in the 0.5-1.7 μm region increased by 10-15% in the 0.45-6.1 km, which corresponds to doubling of

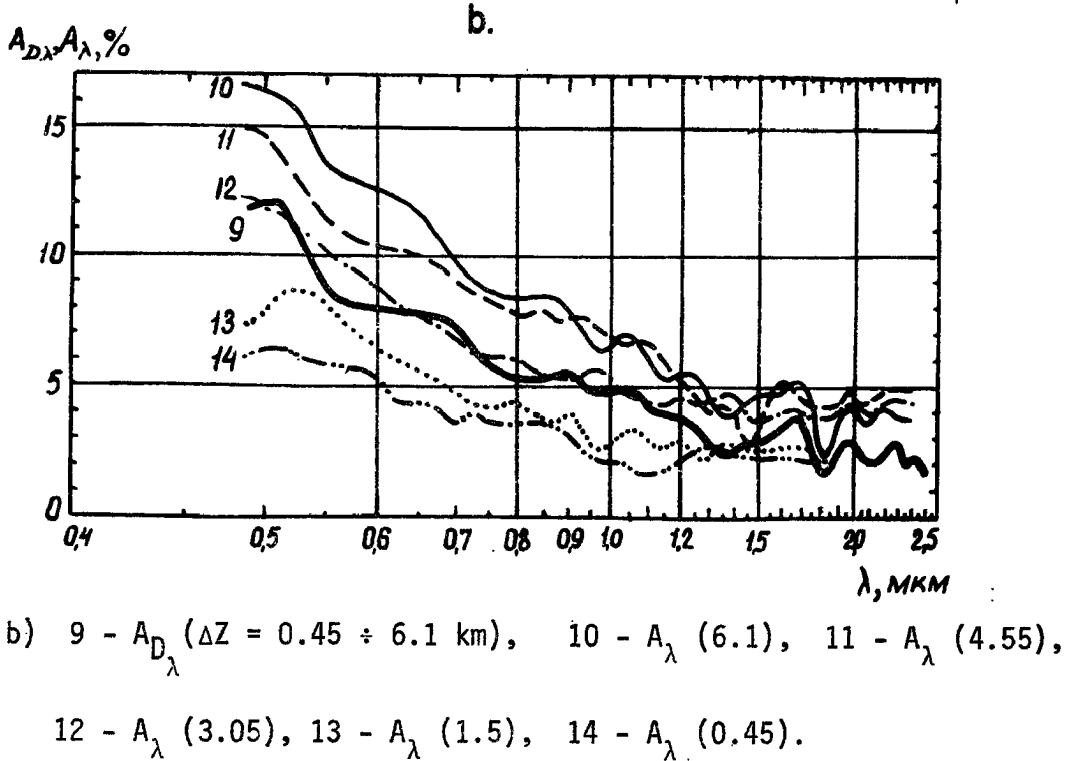
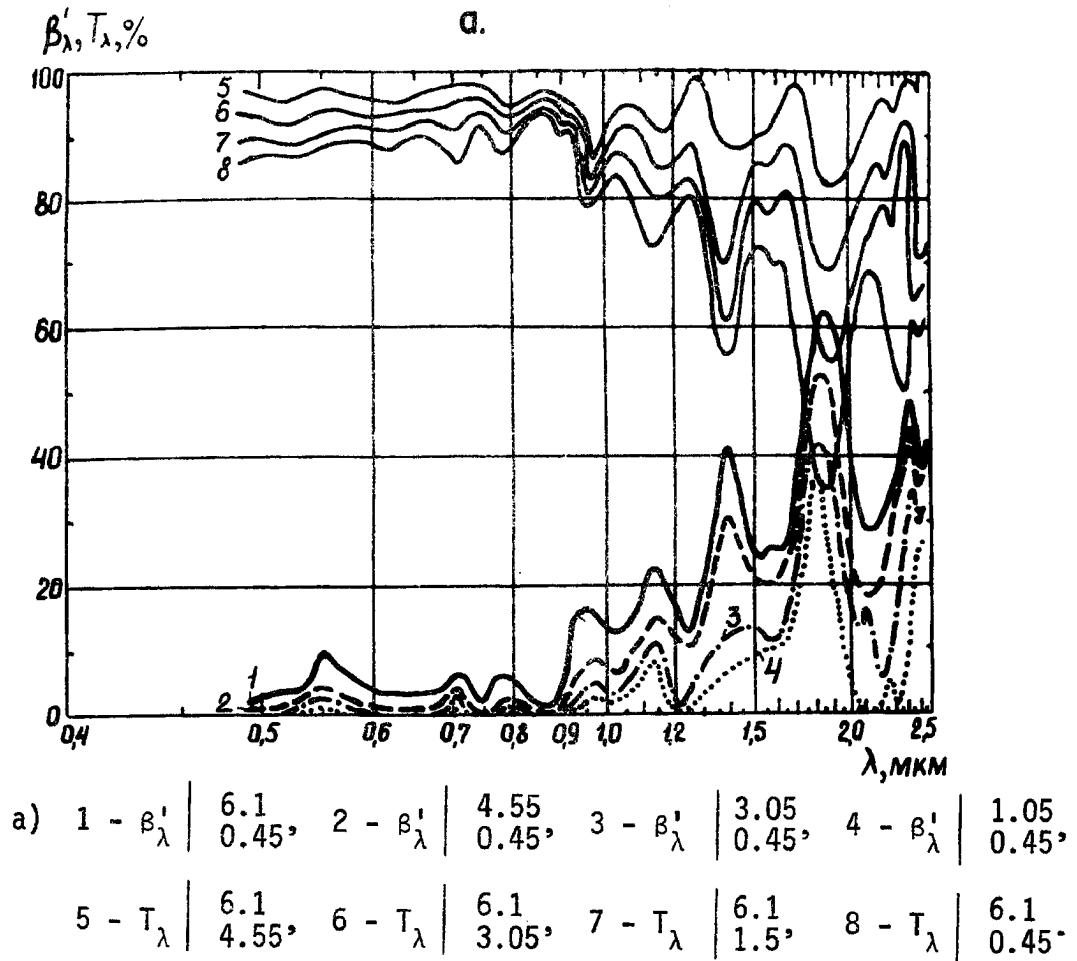


Fig. 27

Spectral relative radiative heat flux divergences β'_λ , transmission coefficients T_λ (a), and albedo A_λ (b) as inferred from the measurements made on 4 September, 1974 at 1200 with $h_\theta = 71^\circ$ by the SPI-74 (2-10) and K-2 (1, 11) spectrometers.

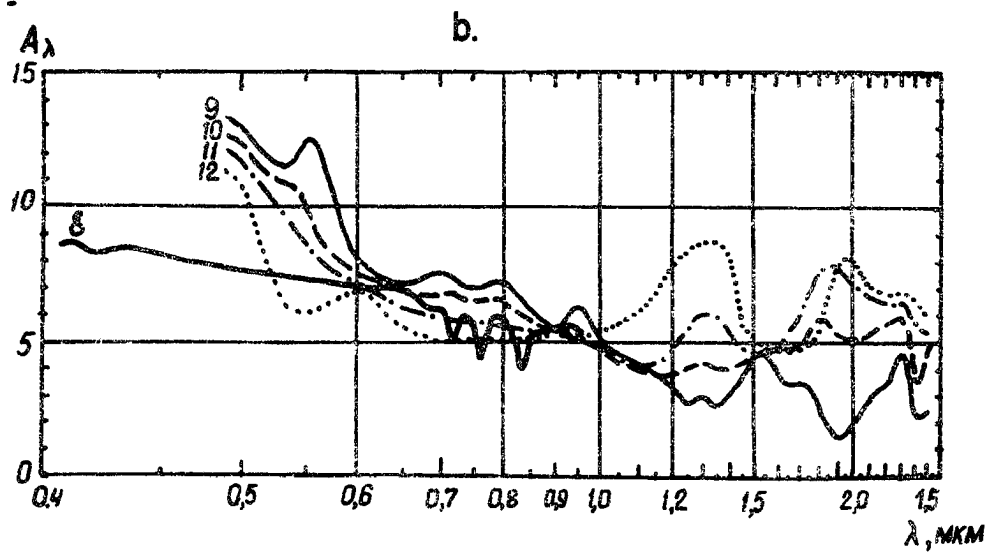
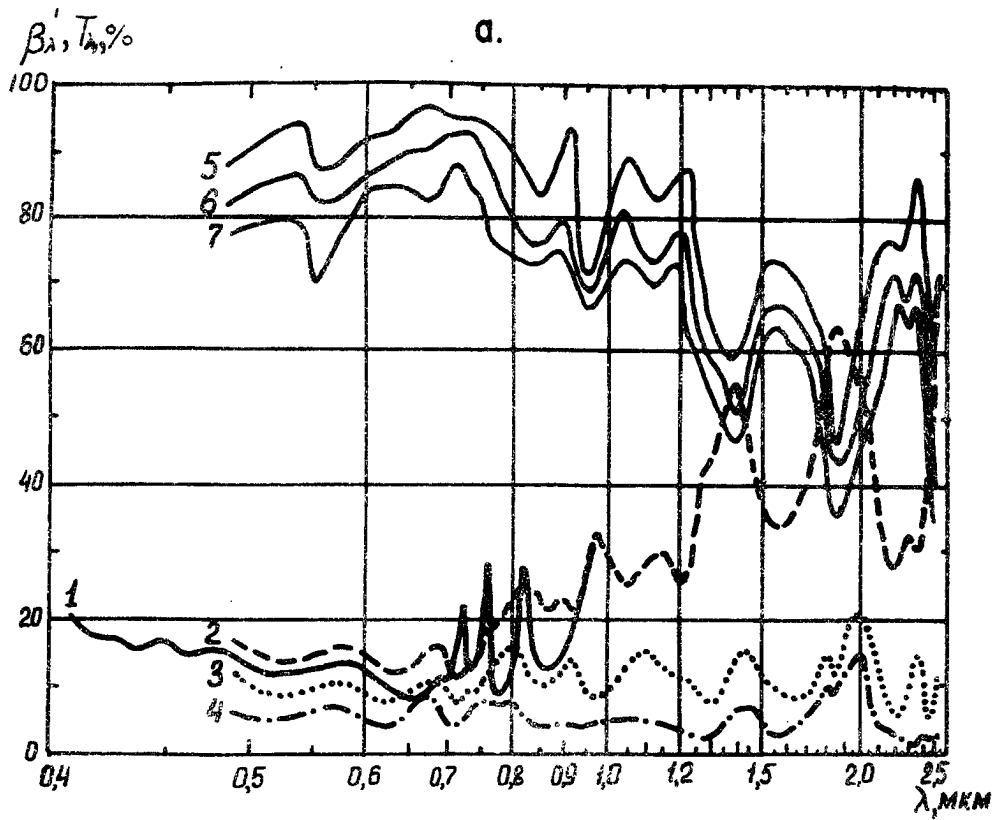


Fig. 28

Spectral relative radiative heat flux divergences β'_λ , transmission coefficients T_λ (a) and albedo A_λ (b) as inferred from the measurements made on 4 September, 1974 at 1450 with $h_0 = 76^\circ$ by the SPI-74 (2-7, 9-12) and K-2 (1,8) spectrometers:

a)	1,2 - β'_λ 6.1	3 - β'_λ 3.05	4 - β'_λ 1.5	5 - T_λ 6.1
	0.45	0.45	0.45	3.05
	6 - T_λ 6.1	7 - T_λ 6.1		
	1.5	0.45		

b) 8,9 - A_λ (6.1), 10 - A_λ (3.05), 11 - A_λ (1.5), 12 - A_λ (0.45).

divergence in the 0.5-0.9 mkm part of the spectrum. In this case, the albedo of the ocean-atmosphere decreased in the visible, the decrease being stronger expressed at shorter wavelengths. The data of Figs. 27 and 28 indicate the vertical inhomogeneity of the air mass's optical properties. Before noon, the most appreciable absorption is observed in the 4.5-6.1 km layer, but at the same time, the increase of albedo with altitude in the 0.5-1.3 mkm region is observed in the 1.5-4.5 km layer. The results of the afternoon sounding lead one to conclude that the strong radiative energy absorption registered before noon in the upper half of the sounded layer, both in the visible and IR, was observed in the afternoon only in the IR spectrum.

In Fig. 28a, the results of measuring the radiative heat flux divergences with the help of two types of spectrometers are intercompared. Due to a higher spectral resolution of the K-2 spectrometer, clearly observed maxima were obtained, which corresponded to the oxygen and water vapor absorption bands. A good agreement is observed between the spectral trace and values of heat flux divergences, obtained by different instruments.

Figure 28b gives the air haze albedo $A_{D\lambda}$ spectral trace. An approximate formula was used for the calculation:

$$A_{D\lambda} \approx \frac{K_{\lambda}(6.1) - K_{\lambda}(0.45) \cdot T_{\lambda} \Big|_{0.45}^{6.1} (m_{\theta} = 1)}{K_{\lambda}(6.1)} \quad (7)$$

As follows from the plot, the haze albedo decreases with wavelength from 11% down to 3% in the 0.5-1.2 mkm spectrum region and is almost constant at longer wavelengths with small maxima around the atmospheric transparency windows. According to the pyranometer data, the relative radiative heat flux divergences during the first and second soundings on 4 September are

20% and 13%, respectively. While the second value agrees with the corresponding data obtained by the K-2 and SPI-74 spectrometers, the pyranometer and SPI-74 data on heat flux divergences calculated for the first sounding differ substantially.

On 4 July at 1411, the values of the spectral and integral parameters, A , T , and β obtained by the SPI-74 spectrometer and pyranometers were analogous to those observed at 1350 on 4 September. From this, one can conclude that radiative properties of the atmosphere during these two days were similar.

On 31 August, the data of the SPI-74 and pyranometers agreed quite well. From 1250 to 1500 the integral heat flux divergence increased from 9.6% up to 22.7% according to the pyranometers' data. The analogous increase of radiative heat flux divergences was registered also by the SPI-74 spectrometer (Fig. 29). As follows from Fig. 29, a strong absorption was fixed in the 0.45-3.05 km layer, the increase of absorption by a factor of 1.5-2 being observed over the spectrum region up to 1.3 μm . On this visually transparent day, the albedo of the underlying surface-atmosphere system did not alter at the altitude of 6.1 km for two hours. However, after noon, the albedo increased at lower altitudes over the entire spectrum.

The albedo vertical profiles on the "transparent" (31 August) and "heavily turbid" (22 September) days are given in Fig. 30. These data are in good agreement with the analogous albedometer data for the same days. According to the above mentioned data, the albedo values on a turbid day exceeded those on a clear day by a factor of 1.5-2.

The bends in the curves of albedo vs. observation altitude correspond to the boundaries of aerosol layers and to special points on the curves of

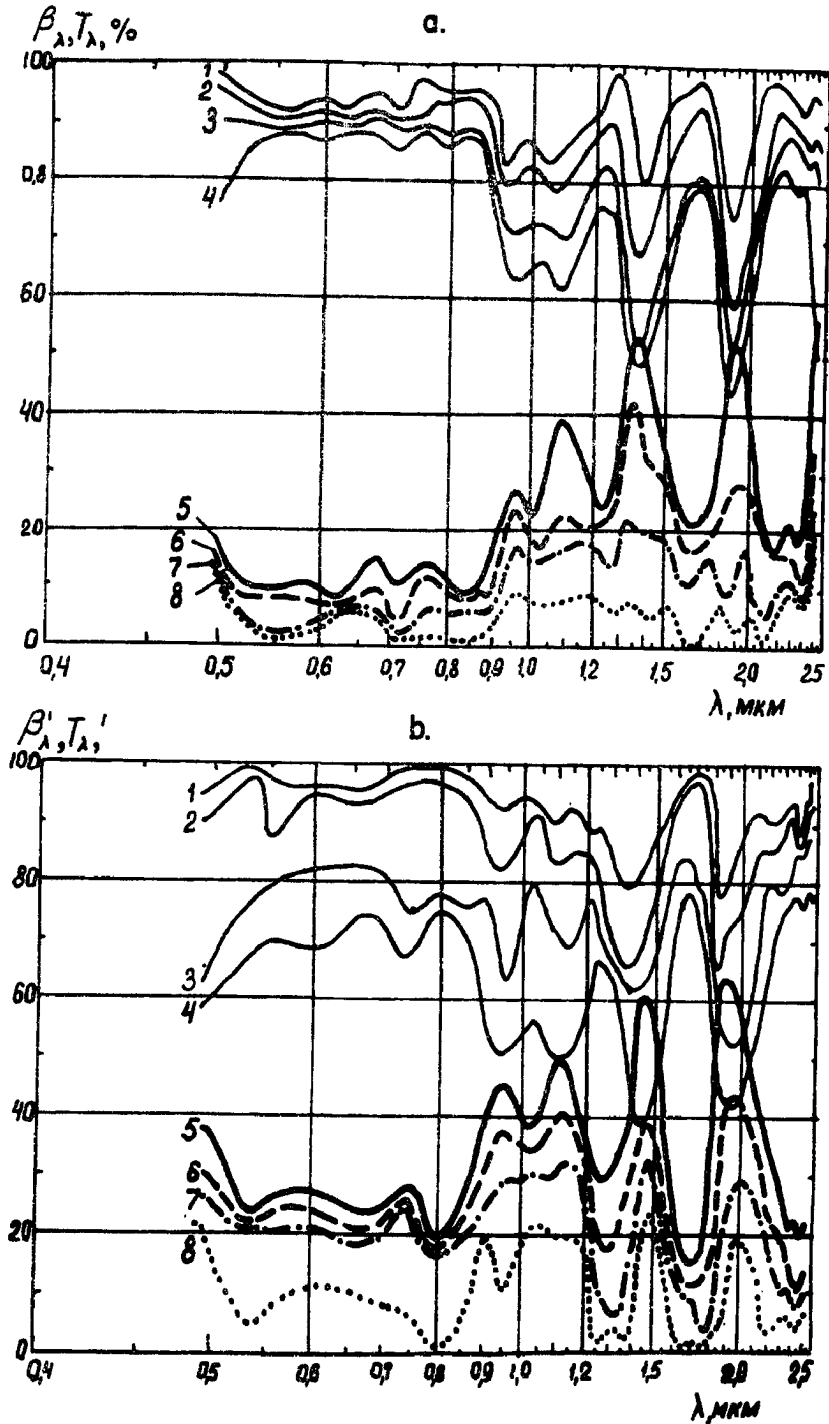


Fig. 29

Spectral transmission coefficients T_λ and relative radiative heat flux divergences β'_λ as inferred from the measurements made on 31 August, 1974, at 1251 with $h_\theta = 79^\circ$ (a) and at 1500 with $h_\theta = 63^\circ$ (b) by the SPI-74 spectrometer.

$$(a) \quad 1 - T_\lambda \left| \begin{array}{l} 6.1 \\ 4.5 \end{array} \right., \quad 2 - T_\lambda \left| \begin{array}{l} 6.1 \\ 3.05 \end{array} \right., \quad 3 - T_\lambda \left| \begin{array}{l} 6.1 \\ 1.5 \end{array} \right., \quad 4 - T_\lambda \left| \begin{array}{l} 6.1 \\ 0.45 \end{array} \right.;$$

$$(b) \quad 5 - \beta'_\lambda \left| \begin{array}{l} 6.1 \\ 0.5 \end{array} \right., \quad 6 - \beta'_\lambda \left| \begin{array}{l} 4.55 \\ 0.45 \end{array} \right., \quad 7 - \beta'_\lambda \left| \begin{array}{l} 3.05 \\ 0.45 \end{array} \right., \quad 8 - \beta'_\lambda \left| \begin{array}{l} 1.6 \\ 0.45 \end{array} \right.;$$

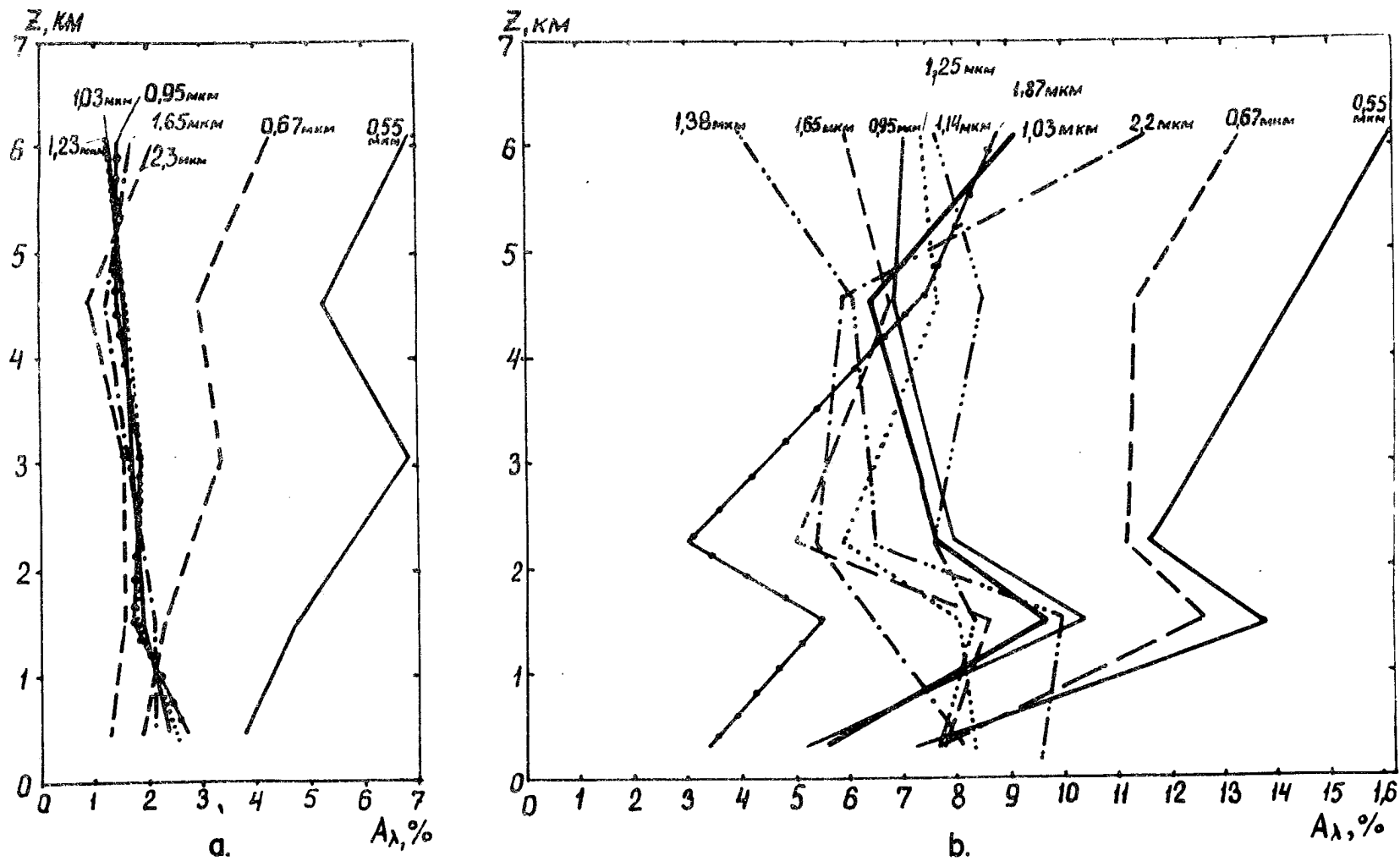


Fig. 30 Vertical profiles of the spectral albedo as inferred from measurements made on 31 August, 1974 (a) and 22 September, 1974 (b).

the temperature and humidity vertical distribution. It should be mentioned that on 22 September, the high values of relative fluxes equal to 35-20% were obtained in the visible 0.5-0.8 μm spectrum region, the heating of the sounded atmospheric layer by visible radiation taking place practically only in the lower 2 km layer. On this day, the absorption values were 30-34%, in the regions corresponding to the atmospheric windows.

For the 4 September and 31 August measurements, the relative radiative flux divergences in the water vapor bands 1.13, 1.38 and 1.87 μm were calculated for the whole sounded atmospheric layer according to the data collected by the SPI-74. The relative radiative energy divergences for the same spectral bands and the same atmospheric layers due to H_2O and CO_2 were calculated by means of techniques described in [24]. For the calculations the water vapor concentration profiles obtained simultaneously from aboard the same aircraft were used; the standard humidity distribution was used for the levels above the flight ceiling.

The difference between experimental (total) and calculated (molecular) values of flux divergences corresponds to the radiative divergence due to the aerosol. The calculated values are presented in Table 6.

It follows from Table 6 that the aerosol absorption is most conservative in the 1.65-2.10 μm band. The spectral curve of aerosol absorption in the IR is characterized by significant instability. Thus, the assumption made in Section 6.1.3 about aerosol absorption decreasing proportionally to λ^{-1} is very approximate.

The extremely high values of radiative heat flux divergences reaching 80% over the entire spectral region of 0.5-2.5 μm , were obtained

Table 6. Total, molecular and aerosol relative influxes of radiative energy.

Date of Sounding	Spectral Interval μm	Relative Influxes of Radiative Energy, %		
		Total	Molecular	Aerosol
4 September 1974 the first sounding	1.05 - 1.25	29	16	13
	1.25 - 1.65	42	17	25
	1.65 - 2.10	46	38	8
31 August 1974 the first sounding	1.05 - 1.25	32	19	13
	1.25 - 1.65	36	26	10
	1.65 - 2.10	30	20	10
31 August 1974 the second sounding	1.05 - 1.25	42	20	22
	1.25 - 1.65	38	25	13
	1.65 - 2.10	30	20	10

on 10 August. It is quite possible that these values are overestimated because the measurements have been taken during aircraft descent glissade. In this case, attention should be paid to the lack of absorption dependence on wavelength in the air mass heavily polluted by dust particles. In the vertical distribution of radiative heat flux divergences, a maximum of absorption was registered in the 2.4-3 km. Nearly half of the radiative heating falls on this layer. The maxima of albedo values reaching 24, 20, 16 and 12% at the wavelengths of 0.5, 0.6, 1.2 and 2.2 μm , respectively, were registered at the altitude of 2.4 km. Above this level, the albedo value decreased; at 6.1 km the albedo values were 18, 8, 3 and 5% for the above-mentioned wavelengths.

The 10 August SPI-74 data can be compared to those of the scientific-research ship "Musson" located about 2000 km from Dakar - the point of the IL-18 aircraft sounding. The dust flow reached the ship operating area on 11 August. "Musson" fixed the decrease of meteorological visibility down to 6-8 km along with the sharp increase of the concentration of particles greater than 0.65 μm in diameter, reaching 30 cm^{-1} in the near-water layer, as well as the decrease of the atmospheric transparency down to 59% by the pyranometer's readings.

Figure 31 gives the curves of the A_λ and β'_λ spectral curves, by the SPI-74 and K-2 spectrometer data obtained on 12 July. The 9-10 point stratocumulus clouds were located at the altitudes of 800-900 to 1400-1500 m; and the dust layer stretched from 2250 to 4500 m. The relative values of radiative heat flux divergences in clouds do not differ from those at the same levels in the atmosphere containing "dry" aerosol (see Fig. 28). However, a strong absorption is observed both in the visible and IR in the upper dust cloud layer. The albedo at all

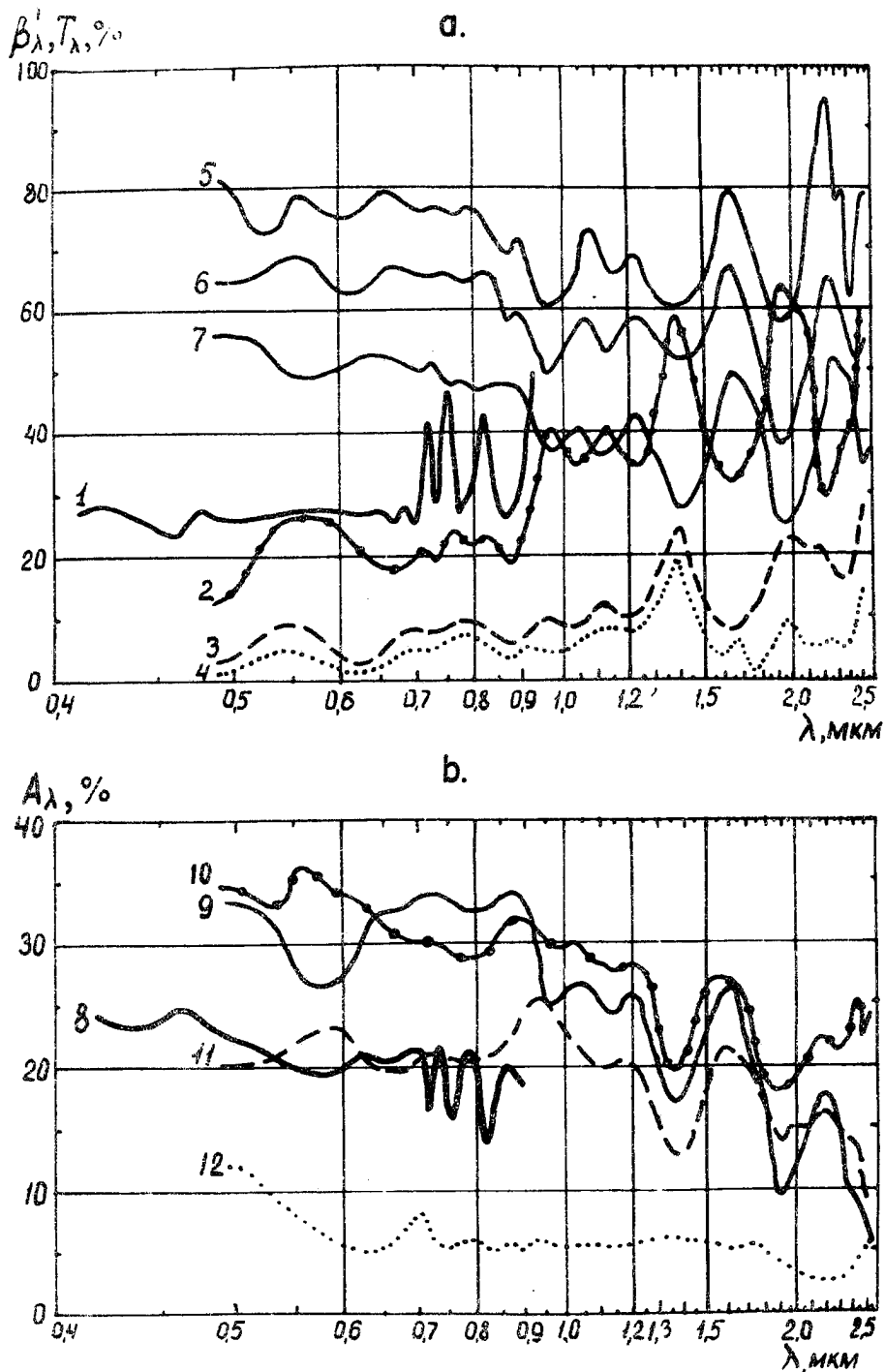


Fig. 31 Spectral relative radiative heat flux divergences β_λ' , transmission coefficients T_λ (a) and albedo A_λ (b) as inferred from the measurements made on 12 July, 1974 at 1330 with $h_\theta = 81^\circ$ by the SPI-74 (2-7, 9-12) and K-2 (1,8) spectrometers.

$$(a) \quad \begin{array}{l} 1,2 - \beta_\lambda' \left| \begin{array}{l} 6.3 \\ 0.3 \end{array} \right., \quad 3 - \beta_\lambda' \left| \begin{array}{l} 3.5 \\ 0.5 \end{array} \right., \quad 4 - \beta_\lambda' \left| \begin{array}{l} 1.5 \\ 0.3 \end{array} \right., \quad 5 - T_\lambda \left| \begin{array}{l} 6.3 \\ 3.05 \end{array} \right., \\ 6 - T_\lambda \left| \begin{array}{l} 6.3 \\ 1.5 \end{array} \right., \quad 7 - T_\lambda \left| \begin{array}{l} 6.3 \\ 0.3 \end{array} \right. \end{array}$$

$$(b) \quad 8,9 - A_\lambda (6.3), \quad 10 - A_\lambda (3.05), \quad 11 - A_\lambda (1.5) \quad 12 - A_\lambda (0.3)$$

wavelengths increases with height up to the 3 km level. Above this level, the albedo remains practically constant in the visible region and in the IR atmospheric transparency windows, while it decreases with height around the absorption bands' centers. The values of the radiative heat flux divergences and albedo of the whole atmospheric layer from 0.3 to 6.3 km turned out to be different according to the K-2 and SPI-74 data. At the altitude of 6.1 km the albedo of the ocean-atmosphere system is higher by 13-14% in the overlapping spectral region of 0.5-0.9 μm from the SPI-74 data as compared to the K-2 data. The radiative heat flux divergences are, on the contrary, higher by approximately 8-10% from the K-2 data. This difference can be caused by errors in calculating the downwelling and upwelling scattered radiation fluxes, according to the measurements of brightness at only two azimuth angles under conditions of spatially inhomogeneous clouds and aerosol atmosphere.

The measurements of the ocean-atmosphere system spectral brightness angular distribution indicate the dependence of the intensity of the sunlight patch observed at the mirror reflection angles, on the degree of atmospheric transparency. Under heavy atmospheric turbidities the reflection anizotropy decreases. These data agree well with the indicator measurements. This dependence can be used in the interpretaion of satellite images for evaluating the extent of atmospheric trubidity over sea.

Summing up the preliminary results of SPI-74 data processing, attention should be paid to the fact that under conditions of the tropical atmosphere over sea, significant absorption is observed in the intervals corresponding to the IR transparency windows, while at moderate latitudes there is no absorption in the clean air at these wavelengths [23, 35].

The revealed effects of decreasing of the ocean-atmosphere system reflectivity in the afternoon with a simultaneous increase of the atmosphere absorbing properties, can be apparently explained by the processes of coagulation and moistening (or drying) of particles under the influence of radiative heating and cooling in convective movements. However, it is necessary also to thoroughly evaluate the role of advection in variability of the atmosphere radiative characteristics. On the one hand, the dust can play the role of condensation nuclei; but on the other hand, a strong heating of the atmosphere at the expense of the dust prevents the formation of clouds.

We highly recommend that, in the future, the study of the balance between the aerosol and molecular components of the radiative heat flux divergence is continued, and also an attempt be made to evaluate the atmospheric aerosol spectral indices of absorption and scattering.

7. ANGULAR AND SPECTRAL CHARACTERISTICS OF SHORTWAVE RADIATION REFLECTANCE.

Under the GATE Radiation Subprogram, the direct measurements of the "water surface-atmospheric layer" spectral albedo as well as the reflected shortwave radiation angular distribution (the reflectance function) in separate spectral bands were performed on board the IL-18M aircraft. The results of measuring spectral albedo according to data obtained on 13 August and 22 September, 1974, under cloudless conditions are presented in this paper together with coefficients of reflectance anisotropy calculated through the angular characteristics of the reflected radiation.

7.1 Spectral Albedo.

The direct spectral albedo measurements in 10 spectral bands of 0.5-1.65 μm region were performed with the help of a spectral albedometer [25] installed in the aircraft's left wing-tip.

In Fig. 32, the spectral albedo vertical profiles for two days characterized by the presence of SAL (22 September) and its absence (13 August) are given. On 22 September the sounding was carried out from 1251 to 1423 GMT, on 13 August from 1300 to 1439 GMT. The aerosol layer upper boundary on 22 September was at 4300 m, the lower boundary reached the water surface; on 13 August the haze could be spotted at 5000 meters. In Fig. 32, the sun elevations, h_{\odot} , for the sounding horizontal runs are given. However, the dependence of A_{λ} on h_{\odot} can be ignored during the albedo profile analysis because the measurements showed that the sun elevation variations that took place during the sounding, influence the spectral albedo profiles far less than the wavelength and aerosol content.

The characteristic feature of the spectral albedo profiles for 22 September (Fig. 32a) is their sharp increase (approximately by the

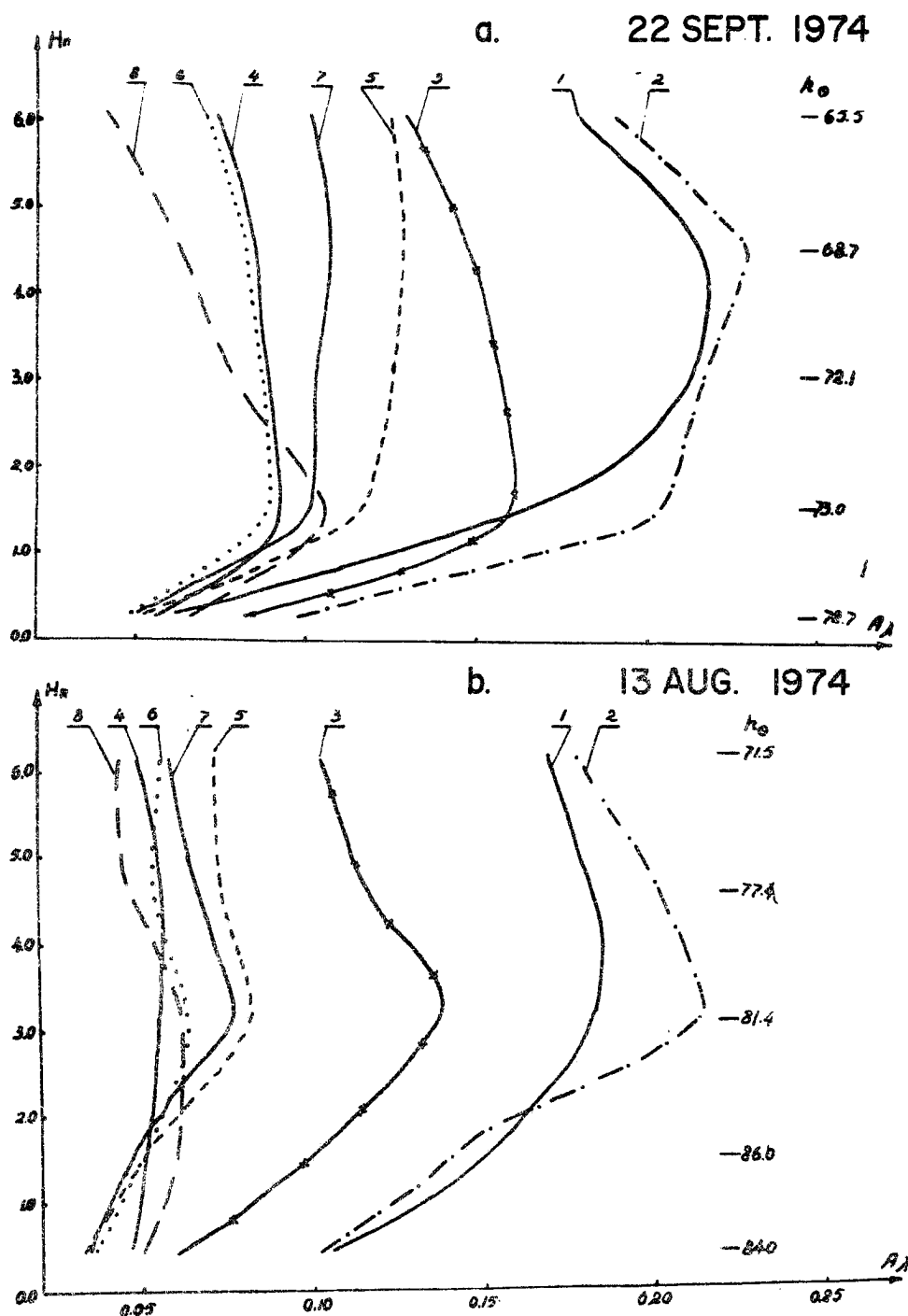


Fig. 32 The spectral albedo vertical profiles measured by the albedometer:

a - 22 September, 1974

b - 13 August, 1974

1 - 0.509 μm ;

2 - 0.553 μm ;

3 - 0.701 μm ;

4 - 0.96 μm ;

5 - 0.99 μm ;

6 - 1.13 μm ;

7 - 1.24 μm ;

8 - 1.38 μm .

factor of 2) in all the spectral bands in the lower atmospheric layer (300-1500 m). In the shortwave bands (0.509 and 0.553 μm) the albedo increased up to the SAL upper boundary, then decreased. In the longwave bands (0.99 and 1.24 μm) the albedo practically did not change at the altitudes of more than 1500 m and decreased in the water absorption bands (0.96, 1.13 and 1.38 μm).

The comparison of spectral albedo vertical profiles presented in Fig. 32 shows that the difference in the albedo values obtained on 13 August and 22 September is greater for the longwave bands than for the shortwave ones.

The spectral albedo vertical profiles of 13 August correlate with the vertical distribution of the total metal content in the aerosol samples (Table 4) - the maximum of total metal concentration is at 3000 m altitude and coincides with the albedo maximum. Thus, the albedo vertical profiles in the considered spectral intervals strongly depend on wavelength and atmospheric dust content.

7.2 Reflectance Functions.

Determination of the shortwave radiation spectral reflectance functions was provided for by the spectral indicatometer (scanning radiometer) [26] in 12 azimuths (over 30°) respective to the solar vertical plane [27] in 10 spectral bands of the 0.5-1.9 μm region (in the same bands as for albedo measurements except one).

The spectral indicatometer measured directly the relative (with respect to the nadir) spectral brightness at different angles, θ from nadir, and azimuth directions, γ , at the solar zenith angle i :

$$f_{\lambda,i}(\theta, \gamma) = \frac{B_{\lambda,i}(\theta, \gamma)}{B_{\lambda,i}(0, \gamma)} \quad (8)$$

Using the data on relative spectral brightness and spectral albedo, $A_\lambda(i)$ the coefficient of directed reflectance $R_\lambda(\theta, \gamma, i)$ or the brightness coefficient $\pi R(\theta, \gamma, i)$ [40] was calculated:

$$R_\lambda(\theta, \gamma, i) = \frac{A_\lambda(i)}{F_\lambda(i)} \cdot f_{\lambda, i}(\theta, \gamma) \quad (9)$$

where

$$F_\lambda(i) = \int_0^{2\pi} \int_0^{\pi/2} f_{\lambda, i}(\theta, \gamma) \cdot \sin \theta \cdot \cos \theta \, d\gamma \, d\theta \quad (10)$$

In order to obtain a more detailed characteristic of the reflected radiation field for the "ocean-atmospheric layer" system, the relative anisotropy coefficient K_A and the reflectance asymmetry coefficient in the solar vertical Γ were calculated by the reflectance functions.

The anisotropy coefficient characterizes the reflectance deviation from the isotropic one and is calculated by the formula:

$$K_A = \frac{F_\lambda(i)}{\pi} \quad (11)$$

The reflectance asymmetry coefficient in the solar vertical is determined from the expression:

$$\Gamma = \frac{\int_0^{\pi/2} f_{\lambda, i}(\theta, 180^\circ) \cdot \sin \theta \, d\theta}{\int_0^{\pi/2} f_{\lambda, i}(\theta, 0^\circ) \sin \theta \, d\theta} \quad (12)$$

where $f_{\lambda, i}(\theta, 180^\circ)$, $f_{\lambda, i}(\theta, 0^\circ)$ are the relative brightness functions in solar vertical and antivertical, respectively.

In Fig. 33, the reflectance functions in the solar vertical for the 0.99 μm wavelength according to data obtained on 13 August and 22 September at different altitudes are presented.

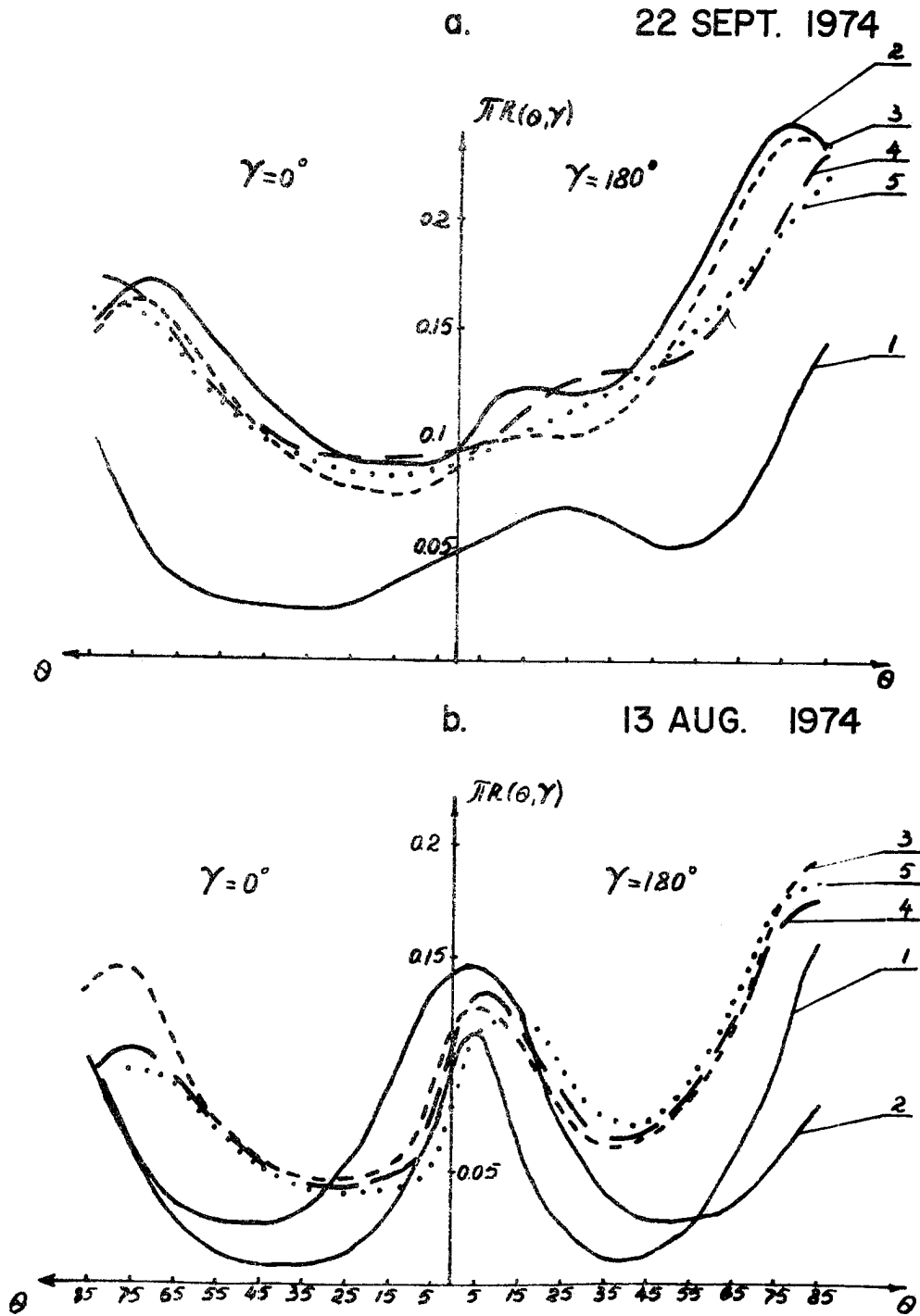


Fig. 33 The angular dependence of brightness coefficient with the sun vertical for $\lambda = 0.99 \mu\text{m}$ and different flight altitudes:

a - 22 September, 1974

b - 13 August, 1974

$\gamma = 180^\circ$ - vertical

$\gamma = 0^\circ$ - antivertical

1 - $H = 400 \text{ m}$,

2 - $H = 1500 \text{ m}$,

3 - $H = 3050 \text{ m}$,

4 - $H = 4550 \text{ m}$,

5 - $H = 6100 \text{ m}$.

The angular dependence of the reflectance coefficient in other azimuth directions and for different wavelengths are not given here, but it should be noted that the reflectance functions hardly depend on measurement of the azimuth at high sun elevations that were observed during the experiment.

From comparing the curves given in Fig. 33, one can see that in the presence of SAL (22 September) the shape of reflectance functions differs greatly from those obtained in a relatively "clean" atmosphere (13 August). The sun path standing out clearly on 13 August at the angles close to nadir at all the flight altitudes (Fig. 33b) is greatly weakened at low altitudes and completely vanishes at 6100 meters on 22 September (Fig. 33a). Insignificant changes of reflectance functions with height begin from 1500 m on 22 September and on 13 August from 3000 meters. On 13 August, the reflectance function at the height of 1500 m is symmetrical with respect to the nadir (Fig. 33b). At other altitudes on 13 August and at all the altitudes on 22 September, the reflectance functions are asymmetrical (the reflectance is stronger at the mirror angles) (Fig. 33).

The reflectance function asymmetry at other wavelengths can be traced through the vertical profiles of the Γ parameter, presented in Fig. 34 for 13 August and 22 September.

The minimum values of asymmetry on 13 August are observed at the altitude of 2000-3000 m at other altitudes this parameter monotonously increases. At the same time, it should be noted that the minimum values of parameter Γ for all the wavelengths correspond to the maximum values of spectral albedo (Fig. 32b) and total concentration of metal aerosols (Table 4).

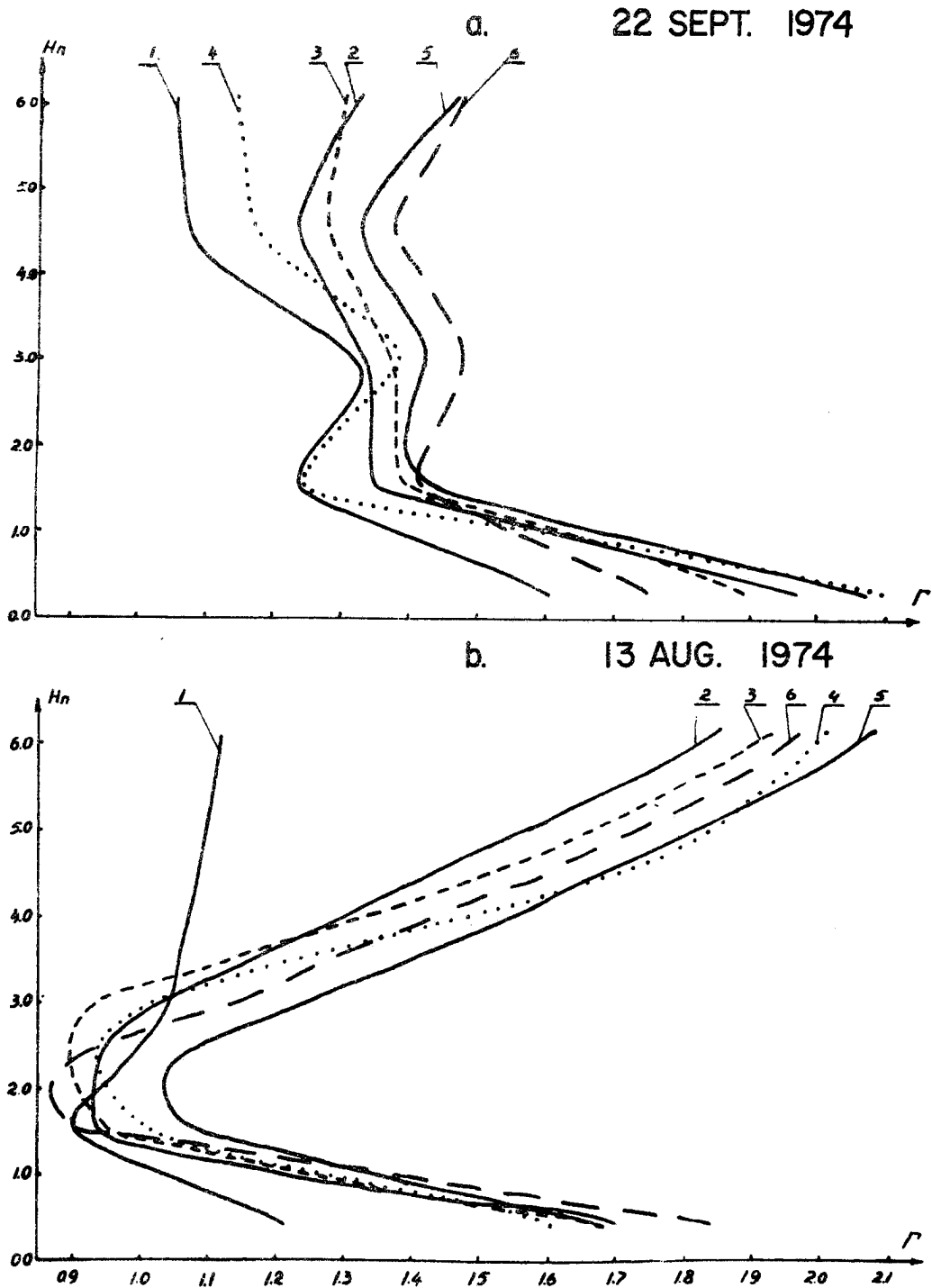


Fig. 34 Vertical profiles of the reflection asymmetry coefficient with the sun vertical for different days and wavelengths:

a - 22 September, 1974,

b - 13 August, 1974

1 - 0.509 μm ; 2 - 0.96 μm ; 3 - 0.99 μm ; 4 - 1.13 μm ;

5 - 1.24 μm ; 6 - 1.38 μm .

As long as the sun elevation changed insignificantly during the sounding, the variation of the reflectance function asymmetry with altitude and wavelength is explained, for 13 August, by the atmosphere's optical properties change with height (see Fig. 34b, curve 1 - shortwave spectral band, curves 2, 3, 4, 5, 6 - longwave region).

Vertical profiles of the reflectance asymmetry coefficient in the solar vertical for 22 September when the SAL was present, differ from parameter Γ profiles for 13 August (Fig. 34). Up to 1500 m the sharp decrease of parameter Γ is observed with a comparatively small variability at higher altitudes. Presumably this is connected with the fact that the SAL lower boundary was located near the water surface and strong variations of atmosphere optical properties were observed in the near-the-water layer. This is confirmed by the trend of the spectral albedo vertical profiles (Fig. 32) and the relative anisotropy coefficient, K_A , presented in Fig. 35.

For 22 September (as well as for other days with the SAL present) the sharp increase of anisotropy coefficient in the 300-1500 m layer and its relatively weak variability higher than 1500 m (Fig. 35a) is characteristic. Let us point out that in a relatively "clean" atmosphere on 13 August the monotonous (close to linear) variation of K_A with height was observed (Fig. 35b).

Intercomparison of the vertical profiles of the parameters, K_A and Γ for different wavelengths on 22 September shows their insignificant dependence on wavelength which corroborates the relatively neutral optical properties of Saharan dust in the investigated spectral intervals. The 0.99 μm wavelength is an exception where a certain increase in the anisotropy coefficient is observed which probably is caused by the SAL anomalous properties in this spectral region.

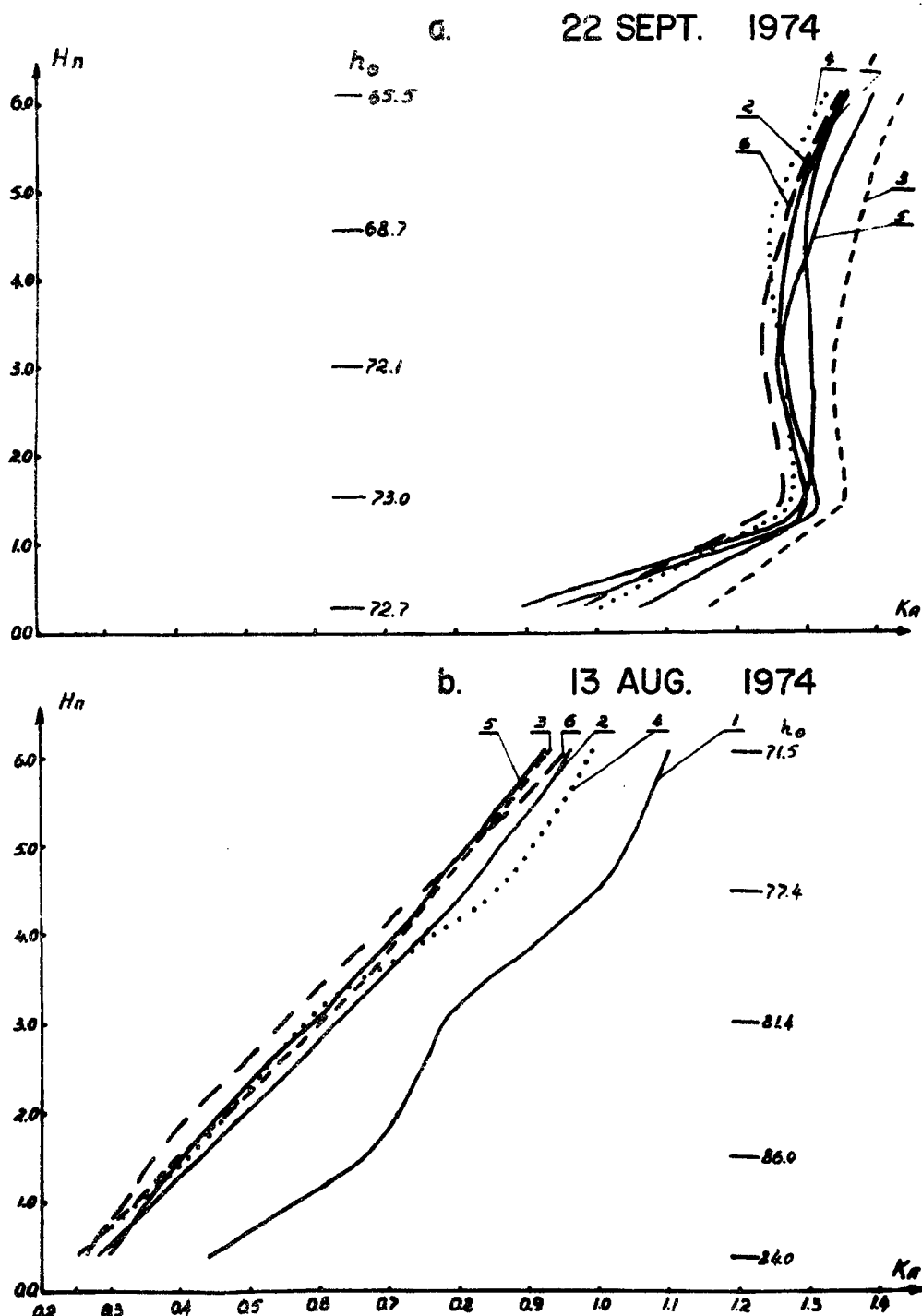


Fig. 35 Vertical profiles of the reflection anisotropy coefficient for different days and wavelengths:

a - 22 September, 1974

b - 13 August, 1974

1 - 0.509 μm ; 2 - 0.96 μm ; 3 - 0.99 μm ; 4 - 1.13 μm ;

5 - 1.24 μm ; 6 - 1.38 μm .

The carrying on of further analysis of the GATE experimental data on the angular reflectance characteristics and spectral albedo of the "ocean-atmosphere" system, with the incorporation of data on aerosol distribution and scattering functions, will produce more detailed information on radiative and optical characteristics of the dusty atmosphere.

8. CONCLUSION

The processing and analysis of the GATE data has only recently begun [38], therefore, it is natural that at this first stage of analysis it is possible to consider only a few aspects of the numerous GATE objectives.

The preliminary studies reported in this document clearly show that the atmospheric aerosol present in the equatorial Atlantic region does have a significant effect upon the distribution of radiative heating and cooling. Since the radiative component is one of the important atmospheric energy sources in the tropics, one must also consider the importance of the aerosol to the dynamics of the tropics. Therefore, the aerosol problem is important not only to the Radiation Subprogram but to the GATE Central Program as well.

It is beyond doubt that the study of SAL and its effect on the general circulation of the tropical atmosphere are also of primary importance from the point of view of planning and implementing the Global Atmospheric Research Programme (GARP).

The revelation of the role of atmospheric aerosol as a climate forming factor should become an important item of this program. This calls for elaboration of the Global Atmospheric Aerosol Radiation Experiment (GAAREX) program as an item of the program of GARP First Global Experiment, which will make it possible to considerably advance the solution of the "aerosol and climate" problem.

REFERENCES

1. Kondratyev K. Ya. "The GARP Atlantic Tropical Experiment and radiative factors of weather and climate". VNIIGMI MID, Obninsk, 1974, 85 pp.
2. Grigoryev A.A., Lipatov V.B. "The dust storms as inferred from the data of space observations". L.,Gidrometeoizdat, 1974, 31 pp.
3. Kondratyev K.Ya., Grigoryev A.A., Pokrovsky A.G., Pokrovsky O.M., Smokty O.I., Timofeev Yu.M. "Remote sensing of the minor gaseous and aerosol constituents of the atmosphere from space". - LGU, 1974, 106 pp.
4. Barteneva O.D., Veseļova L.K., Nikitinskaya N.N. "On the optical properties of the atmospheric aerosol in the tropical zone of the Atlantic". - Proceedings of the Interdiscipline geophysical expedition within the programme of the National Atlantic Tropical Experiment, L., Gidrometeoizdat, 1974, p. 482-495.
5. Kats A.L., Belenky V.S. "On a powerful dust outbreak from the African continent." - L.,Gidrometeoizdat, 1971, p. 154-159.
6. Petrov M.P. "Deserts of the globe". - Nauka, L., 1973, 435 pp.
7. Kapo-Rey R. "The French Sahara". Geographiya, L.,1958, 495 pp.
8. Fett V. "Atmospheric dust". - M.,Inostrannaya literatura,1961.
9. Abramov R.V. "Dust in the atmosphere over the Atlantic. Sedimentation conditions in the Atlantic". - Okeanologicheskiye issledovaniya, 1971, No. 21, p. 7-30.
10. Laktionov L.G.,Gudimenko A.V., Kopchenov V.M., Semko N.N., "Some characteristics of aerosol in the tropical zone of the Atlantic". - Proceedings of the Interdiscipline Expedition TROPEX-72, Gidrometeoizdat, 1974, p. 526-539.
11. Barteneva O.D. "On the light scattering indicatrices in the near-water atmospheric layer".-Proceedings of the Interdiscipline Expedition TROPEX-72", L., Gidrometeoizdat, 1974, p.474-481.

12. Burmistrova V.D., "Variability of the atmospheric transparency for the solar radiation under the atmospheric circulation conditions". - Proceedings of the Interdiscipline Expedition TROPEX -72, L., Gidrometeoizdat, 1974, p. 461-466.
13. Laktionov A.G., Bogomolov Yu.P. "The surface aerosol size distribution". - Izvestiya AN SSSR, Phisika atmosfery i okeana. 1971, v.7, No. 3.
14. Kastrov V.G. "Measurement of the solar radiation absorption in the free atmosphere up to 3-5 km". -Trudy TsAO, 1952, issue 8.
15. Snopkov V.G. On the total water content in the atmosphere in the tropical zone of the Atlantic as inferred from the data of the aerological sounding made on board the scientific research ship "Akademik Kurchatov". - Proceedings of the Interdiscipline Expedition TROPEX-72, L., Gidrometeoizdat, 1974, p. 194-196.
16. Kondratyev K. Ya., Nikolsky G.A., Esipova E.N., "Balloon measurements of radiation fluxes in the free atmosphere". - Izvestiya AN SSSR, Phisika atmosfery i okeana, 1966, V.2. No.4.
17. Barteneva, O.D. "Light-scattering indicatrix in the surface atmospheric layer".-Izvestiya AN SSSR, Ser. Geophysika, 1960, No. 12, p. 1853-1865.
18. Sivkov S.I. "Calculation techniques for the solar radiation characteristics". - 1., Gidrometeoizdat, 1968.
19. Vasilyev, O.B., Voitov V.P., Grischechkin V.S., Michailov V.V. "The techniques for the accomplishment of the Complex Radiation Experiment". - Collection of papers" Sbornik phisiki atmosfery", Izd.LGU, 1971, issue 9, p. 23-28.
20. Grischechkin V.S. "Spectral upwelling and downwelling radiation fluxes in the atmosphere". -Trudy GGO, 1973, issue 322, p. 3-11.
21. Kondratyev K.Ya., Vasilyev O.B., Grischechkin V.S., Ivlev L.S., Popov L.V., Prokofyev M.A., Tchapursky L.I. "Spectral radiative heat flux divergences in the troposphere over the 0.4-2.4 m range". -Trudy GGO, 1973, issue 322. p. 12-35.
22. Binenko V.I., Vasilyev O.B., Grischechkin V.S., Kondratyev, K.Ya. Tchapursky L.I., Tchernenko A.P. "Measurements of spectral characteristics of reflection, transmission and absorption of cloudiness in the wavelength region of 0.35-2.5 m".-Trudy GGO, 1973, issue 317, p. 3-7.

23. Kondratyev K. Ya., Ivanov V.A., Zhvalev V.F., Prokofyev M.A., Ter-Markaryants N.E., Tchapursky L.I. "The combined subsatellite experiment". -Trudy GGO, 1973, issue 317, p. 105-114.
24. Golubitsky B.M., Moskalenko N.I. "The spectral transmissivity functions in the H₂O vapour and CO₂ bands" . - Izvestiya AN SSSR, FAO, 4, 3, 1968, p. 346-360.
25. Korzov, V.I., Krasilschikov L.B. "Aircraft instrumentation for reflectivity measurements. II. Spectral albedometer". -Trudy GGO, 1973, issue 295, p. 200-204.
26. Korzov V.I., Krasilschikov, L.B. "Aircraft instrumentation for reflectivity measurements. I. Spectral indicatometer". - Trudy GGO, 1972, issue 275, p. 219-225.
27. Korzov V.I., Krasilschikov L.B. "The spectral reflectivity measurements from aircraft". - Trudy GGO, 1972, issue 275, p. 195-198.

BIBLIOGRAPHIC DATA SHEET	1. Report No. CSU-ATSP-247	2.	3. Recipient's Accession No.
4. Title and Subtitle Aerosol in the GATE Area and Its Radiative Properties		5. Report Date June 1976	6.
7. Author(s) K. Ya. Kondratyev, et al.	8. Performing Organization Rept. No. CSU-ATSP 247 Transactions MGO 381		10. Project/Task/Work Unit No.
9. Performing Organization Name and Address Department of Atmospheric Science, Colorado State University Fort Collins, Colorado 80523 U.S.A. Main Geophysical Observatory, Dept. of Radiation Studies, 7, Karbysheva St., 194018 Leningrad, U.S.S.R.		11. Contract/Grant No. NOAA-C4-6-158-44036	
12. Sponsoring Organization Name and Address NOAA, 6010 Executive Blvd., Rockville, Maryland 20852, U.S.A. Department of Radiation Studies, Main Geophysical Observatory, 7, Karbysheva St., 194018 Leningrad, U.S.S.R. Department of Atmospheric Physics, Leningrad State Univ., USSR		13. Type of Report & Period Covered	14.
15. Supplementary Notes This is the first joint publication by scientists at CSU and MGO in a series devoted to the analysis of GATE Radiation Subprogram results.			
16. Abstracts This report summarizes preliminary results of a research program conducted by Main Geophysical Observatory scientists during the GATE (GARP Atlantic Tropical Experiment). The origin and characteristic features of the dust layer are discussed. Inferences of microphysical and optical characteristics of the dust aerosol made from ship data are presented. Chemical analyses of aerosols showed a rather high content of metals. The iron concentration nearly always exceeded $10^{-5} \text{ kg m}^{-3}$ for aircraft aerosol observations. Extensive data are presented giving spectral and total shortwave radiative flux divergence values for cloudfree, dust and stratoform cloud cases. These data are interpreted in the context of the meteorological conditions and the optical parameters of the aerosol or cloud layer.			
17. Key Words and Document Analysis. 17a. Descriptors Saharan Aerosol Layer Radiative Characteristics GATE Atmospheric Radiation 17b. Identifiers/Open-Ended Terms 17c. COSATI Field/Group			
18. Availability Statement		19. Security Class (This Report) UNCLASSIFIED	21. No. of Pages 109
		20. Security Class (This Page)	22. Price